Quality analysis comparison of 3D products from satellites and aerial images : MICMAC Application in Hilly Zones(Liège)

Auteur : Dukuzemariya, Tharcille
Promoteur(s) : Cornet, Yves
Faculté : Faculté des Sciences
Diplôme : Master en sciences géographiques, orientation géomatique et géométrologie, à finalité spécialisée
Année académique : 2016-2017
URI/URL : http://hdl.handle.net/2268.2/3124

University of Liège

Faculty of Sciences

Geographical Sciences

DSM creation and image orthorectification from satellite and aerial very high resolution products: MICMAC application in hilly and urban area of Liège, Belgium.

Submitted by: Tharcille DUKUZEMARIYA

In partial fulfillment of requirements for the degree of**:**

Master in Geography:

Geomatics and Surveying

Academic year:

2016-2017

Supervised by: **Mr. Yves CORNET**

Jury members: **Mr. Pierre HALLOT**

Mr. Matthias VANMAERCKE

University of Liège

Faculty of Sciences

Geographical Sciences

DSM creation and image orthorectification from satellite and aerial very high resolution products: MICMAC application in hilly and urban area of Liège, Belgium.

Submitted by: Tharcille DUKUZEMARIYA

In partial fulfillment of requirements for the degree of**:**

Master in Geography:

Geomatics and Surveying

Academic year:

2016-2017

Supervised by: **Mr. Yves CORNET**

Jury members: **Mr. Pierre HALLOT**

Mr. Matthias VANMAERCKE

Table of Content

List of Tables

List of figures

List of Abbreviations

(I)FOV: (Instantaneous)Field Of View

(N)IR : (Near)Infra-Red

Apero : Aérotriangulation Photogrammétrique Expérimentale Relativement Opérationnelle

B/H: Base to Height Ratio

CCD: Charge-Coupled Device

CPs: Check Points

DEM: digital elevation model

DORIS: Doppler Orbitography and Radio positioning Integrated on Satellite

DSM : Digital Surface Model

ELISE : Elements of an Image Software Environment

ENSG : Ecole National des Sciences Géographiques

GCPs: Ground Control Points

GNSS: Global Naviation Satellite System

GPS: Global positioning System

GSD: Ground Sampling Distance

IMU: Inertial Measurement Unit

JARS: Japan Remote Sensing Study Group

MICMAC : Multi-Images Correspondances par Méthodes Automatiques de Corrélation

MSS: Multispectral Scanner System

NGA: National Geospatial Intelligence Agency

NW : North-West

PICC : Projet Informatique de Cartographie Continue

PSF: Point Spread Function

RPC: Rational Polynomial Coefficient

SfM: Structure from Motion

SIFT: Scale Invariant Feature Transform

SW: South-West

Acknowledgment

I would express my gratitude to almighty God for his protection and caring during my stay in Belgium.

I am grateful to Yves Cornet, my supervisor, for guidance, support and fruitful advices to this research. Also thank you for organizing my internships at ENSG so that I acquire skills I needed in “Multi-Images Correspondances par Méthodes Automatiques de Corrélation” (MICMAC) software.

Sincere thanks to Marc Pierrot-Deseilligny and his assistant Ewelina Rupnik for not only supporting me technically but also to sacrifice their enormous duties to ensure that I got enough knowledge about MICMAC.

Many thanks to Christophe Schenk from the Walloon region administration and to Carl Deroanne from AERODATA for providing aerial imagery and useful information.

I express my thanks to Réné Warnant, professor at University of Liège who rent me GNSS receiver for GCPs field survey.

Gratitude to Marc Binard for technical support in informatics and logistical help.

Thanks to Florent Poux and to Romain Neuville for their encouragements and helpful comments. I also thank all staff members in the Geomatics Units for their direct and indirect support.

I am indebted to my family for their encouragements and prayers during my studies. This work is dedicated to you.

Classmates and friends, thanks for strong collaboration and friendship that made me feeling at home and stable during my studies.

Without you all, this research should not have been fruitful and successful as it is.

CHAPTER I. : GENERAL INTRODUCTION

Photogrammetry and remote sensing being introduced in 19th century made a recent significant development in mapping through both satellites and aerial sensors which produce earth surface's space based images.

Nowadays, many platforms are equipped with high spatial resolution sensors. This resolution, often expressed in meters varies from one sensor to another and define the ability of the sensor to identify the smallest detail on the image. Most optical high satellite sensors utilise pushbroom technique which replaces the scanning motion by a series of sensors on a line, so the resolution and field of view (FOV) are given by the choice of optics and number of elementary sensors (30,000 for Pleiades). The image is thus constructed line by line while taking into accounts the movement of the satellite (Nicolas, 2012). Optical satellite sensors having capacity to vary ground sampling distance(GSD), they provide short revisit time.

From 1990s, digital cameras are on market. Since then, they made a rapid success in photogrammetry. However, the analogue cameras remain the basic data in photogrammetry and some digital camera's manufacturers kept their conventional central perspective for image acquisition so that the existing software can still be used while other cameras are designed to use pushbroom technology. Digital sensors are more preferable than analog sensors due to their superior radiometric quality and better geometric quality in addition to more varied recording and multi-spectral recording capabilities.

Three dimensional models of the terrain or surface are generated from object restitution and recognition from multiple stereoviews of flying area. They constitute a crucial basic topographic data for major engineering projects, geological or landscapes studies, natural hazard monitoring and precise surveying. Their geometric qualities like precision, accuracy and fineness of high spatial frequency structures, depend on image acquisition techniques, auxiliary data quality, flight planning parameters, FOV of the sensor, used photogrammetric processing algorithms, aerotriangulation configuration and on relief of study area (Billen and Cornélis, 2000). Furthermore, the influence of sensor on accuracy of created digital surface model (DSM) depends on base to height(B/H) ratio and consequently on the incidence angles of stereo images (Poli and Caravaggi , 2013).

Aerial images are the mostly used in large scale mapping mainly due to their high spatial resolution. However, the current availability of very high satellites sensors able to acquire

images at some decimeter level of resolution with large spatial coverage stimulate our curiosity to know which specific quality of 3D models can be obtained from both aerial and satellites data. Thus, the main purpose of this research is to analyze the geometric quality of DSMs products from high spatial resolution satellites stereo- photogrammetry to those from aerial stereo-photogrammetry. In addition to that guidelines for carrying the same study in mountainous countries like Rwanda were mentioned.

This report is subdivided into seven chapters; first chapter describes the general introduction together with research objectives, chapter two deals with states of the art, third chapter explains hypothesis and characteristics of the area of study, fourth chapter cites methodology and qualification of used datasets, fifth chapter details and discusses the obtained results, validation of hypothesis and how this study can be undertaken in Rwanda, lastly chapter seven concludes the research and proposes future improvements.

CHAPTER II. : STATE OF ART

This chapter describes the states of the arts together with relevant literature review about research topics. It deals with fundamentals of photogrammetry, photo interpretation of satellite and aerial imagery and their respective computer based processing for the reconstruction of topography.

Therefore, after a brief historical description of aerial and satellite photogrammetry, we firstly describe some relevant characteristics and geometric models of photography and digital image acquisition. After this description, we then set up some algorithms implemented in photogrammetric software as well as in MICMAC opensource which is used in this study.

II.1. Brief historical development in photogrammetry

According to Linder (2009) photogrammetry is known to have three main development phases distinguished by techniques of the equipment used and workflow. The first phase was a*nalog photogrammetry* in which the reconstruction of orientation of photos and measurements, were performed using optico-mechanical instruments. Aerial analog photos taken by metric camera were exploited since the development of the first cameras consisting in a number of circular arranged lenses able to widen up the camera's field of view and the technical possibility to perform aerial surveys from aircrafts at the beginning of 20th century. *Analytical photogrammetry* is the second phase where, this reconstruction was done algorithmically using computers. Required equipment became then smaller, cheaper and more easily handled. However, analog photos taken by metric cameras on films were still used and it necessitated high precision mechanical and optical eyepiece equipment called "analytical plotter" that were continuously improved since early 20th century. The third phase is *digital photogrammetry* in which digital (or numeric) images are directly processed using computers with a cheap and fast digital workflow.

The transition from analytical to digital photogrammetry was the fundamental photogrammetric development thanks to softcopy-based systems. Digital aerial sensors were the first to be used before the introduction of satellite sensors for military purposes. But according to Luhmann (2004), efficient digital cameras were on the market since 1990s.

In digital photogrammetry, digital images constitute the basic inputs. They can be images taken in digital format by digital aerial camera or onboard satellite sensors or scanned negative (analog) photos.

The main distinction from analog and digital sensors is that the latter uses Charge-Coupled Device (CCD) instead of films for photograph acquisition. As stated by Kiema and Awange (2013) the CCD converts photons that reach the sensor surface into electrons which after being accumulated in capacitors and converted are stored into digital form.

Regarding satellite history in Earth observation and photogrammetry, the US CORONA missions were the first satellite systems to be launched in space in 1960 for military intelligence tasks (Baumann, 2009). Some CORONA missions using forward and backward analog cameras (KH4A) allowed the acquisition of stereo-pairs of photos. The commercial market of space borne sensors of medium up to (very-)high spatial resolution started with the launch of Landsat-1 satellites in 1972 and followed by SPOT-1 in 1986 and IKONOS in 1999 (Toth and Józ´ków, 2015). Since then, the advancement of space technology has led to the affordable space products of nowadays.

However, the traditional satellite systems like Landsat and SPOT 1 to 4 were not correctly designed for photogrammetric purposes because stereo pairs were acquired with large delay (at least one day) from different orbits producing some difficulties to detect homologous points in an automatic way of both images. On the contrary, more recent satellite systems like Ikonos, Quickbird, SPOT5 (HRS instrument) and Pleiades were specifically designed for photogrammetric applications (bi- and tri-stereoscopy): satellite-sensor agility to perform nearly instantaneous stereo pair acquisition, sensor calibration, platform-sensor position and attitude control.

From the time when commercial satellites images' resolution improved, the difference between airborne and satellite images has decreased and the use of the latter made a clear progress (Toth and Józ´ków, 2015).

II.2. Image characteristics

To better understand space images, the four basic types of resolution must be distinguished: spatial, radiometric, spectral, and temporal resolutions.

S*patial resolution* usually expresses in pixels per meter, settles on the smallest detail that can be seen on the image. As stated by Kiema and Awange (2013) spatial resolution depends on sensor altitude, detector size (or points sampling frequency along the scan line for scanning sensors like Landsat MSS, TM, ETM+ and OLI), focal length and system configuration. Therefore, the finer the spatial resolution, the smaller the detected details are and obviously, the more expensive the imagery is. For passive sensor, spatial resolution depends basically on Instantaneous Field of View (IFOV). It is the solid angle in which the sensor integrates the electromagnetic signals coming from the area around each sampled point and it determines the area of earth's surface observed at a particular time from a given altitude (Poli, 2005). This area depends also on the Point Spread Function (PSF).

The IFOV and the PSF determines the Ground Sampling Distance (GSD) between two neighbouring points allowing a continuous (spatial autocorrelation of the recorded signal) measurement surface reflectance. Poli (2005) suggests a classification of spatial resolutions of satellite imagery such as very high (GSD < 1 m), high (GSD between 1 m and 5 m), moderate (GSD between 5 m and 20 m), low (GSD between 20 m and 50 m) and very low (GSD larger than 50 m).

Radiometric resolution describes the actual information content in the image and the sensor's ability to distinguish the smallest energetic variations in reflected, emitted or backscattered electromagnetic signal (Canada Centre for remote sensing, n.d). This characteristic is fundamental during the homologous point detection with matching algorithms. It is usually expressed as an integer number of bit-depth used to quantize pixel values at which images are recorded; for example, 0 to 255 for 8 bits.

Spectral resolution defines the size and number of spectral bands that the sensor is able to record within a specific wavelength range to describe the spectral signature (reflectance variation in function of the wavelength) of the observed surfaces. The finer the spectral resolution, the narrower the wavelength range for a particular channel or band (Kiema and Awange, 2013). The higher the number of bands, the more comprehensive the spectral signature curve is. Spectral resolution varies from panchromatic to multispectral or even hyperspectral sensors. Panchromatic sensors record grey level images mixing the electromagnetic signal in the whole visible and near infra-red spectral range while multispectral and hyperspectral sensors record images by decomposing the signal to very large number of spectral bands (3 visible bands, 2 near infrared bands, 1 Short Wave Infra-Red bands and 1

double-gain thermic IR band for the multispectral TM sensor onboard Landsat for example). The widest spectral range in which panchromatic sensors operate, allows finest spatial resolution compared to multispectral ones. To produce very high resolution multispectral products, image fusion methods combining panchromatic and multispectral acquisitions (Pan-sharpening) are thus used.

Temporal resolution expressed in hours or days, refers to the period by which the same area is sensed by a sensor onboard of unique satellite (the case of satellite constellations like Cosmos-Skimmed with imaging radar onboard is somehow different). It is also named the revisit time. Such characteristic doesn't exist for aerial survey. The temporal resolution of a sensor depends on a variety of factors, including the satellite/sensor capabilities (agility in attitude variation), the field of view and the swath overlap in function of the latitude for round-trip orbiting satellites (retrograde, polar and sun-synchronous orbit) (Canada Centre for remote sensing, n.d).

II.3. Aerial photography and imagery

II.3.1. Film and digital aerial cameras

Over more than a hundred years ago, photographs have been taken by film based or analog cameras. Traditionally, analog aerial cameras use large film format; normally 23 cm by 23 cm, for acquiring large field of view which reduces the number of flight lines to be flown (Leberl and Gruber, 2003). Numeric images acquisition from airborne sensors made a transition from film based analog cameras to digital cameras. According to Leberl and Gruber (2003), this advancement made flight mission cost saving from all expenses on film and scanning process.

Field of view of digital camera is defined as the number of pixels across the swath (rows of an image) (Leberl and Gruber, 2003). This number ensures that field of view of digital image is as large as that of standard analog image of 23 cm.

While for analog cameras, mission parameters were determined by the required scale of photographs, in digital cameras Ground Sampling Distance (GSD) related to focal, flight height and sensor type, resolution and size has to be specified first as it impacts the cost of flight and data processing in the way that the higher GSD, the more flight lines and data to be acquired on a specific area (Neumann, 2009). So, GSD is chosen in the interval of minimum and maximum based on scanning resolution and the reference scale of the product to be created (orthoimage, maps, 3D objects database …):

$$GSD = \frac{1}{Imaging\ scale * scanning\ resolution}\ n \qquad (1)$$

Imaging scale equals the ratio between focal length and height of flight above the mean ground elevation:

$$Imaging\ scale\ at\ A = \frac{f}{HA} \qquad (2)$$

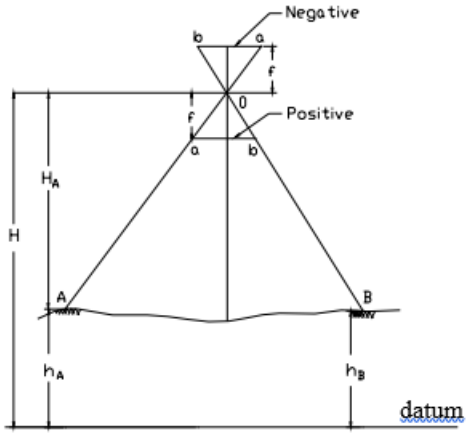

Figure 1: Flight height (HA), mean ground elevation (hA) and flight altitude (H)

For digital cameras, the equation (1) is adapted using pixel size of the CCD:

$$GSD = Imaging\ scale * pixel\ size \qquad (3)$$

Generally, CCD pixel size ranges from 6 microns up to 12 microns (Neumann, 2009).

Digital aerial cameras can be classified as large, medium and small format systems. Large format digital cameras systems efficiently collect and process wide swaths of (very-)high spatial resolution imagery by direct digital capture and acquire images in visible and near infrared channels (Coulter and Stow, 2008). Currently, there are three commonly known manufacturers of large format cameras which are Leica Geosystems ADS40, Vexcel UltraCam and Intergraph Z/I Imaging® DMC. From acquisition point of view, digital aerial cameras are either linear array CCDs or frame (or area) array CCDs. Both, UltraCam and DMC are frame (or area) array CCDs while ADS40 is a linear array CCDs sensor system.

Even though digital aerial cameras are more frequently used in photogrammetry, analog photographs are still used for mapping. As analog cameras photographs are central perspective projection, in frame array sensors, the central perspective geometry is kept so that as a benefit, existing software can still be used in processing. On the other side, linear array CCDs is

oriented across flight direction and collects data continuously, similarly to pushbroom acquisition by satellite sensors (Linder, 2009). With linear array, there are specific effects due to platform motion and attitude variation on the acquisition geometry.

II.3.2. Acquisition techniques by digital aerial cameras

Linear CCDs sensors use a triplet technique in focal plane with a single sensor head and provide forward, nadir and backward viewing (figure 2). In addition, each image line is acquired over a unique time and associated with a unique camera position and orientation. On the other hand, frame (area) CCDs sensors operate in the same way as film cameras with unique camera station per frame. They utilize multiple CCD arrays to generate individual large format image frames and (very-)high spatial multispectral images are obtained through image fusion or pan-sharpening (Coulter and Stow, 2008).

Due to central perspective geometry, interior geometry, calibration and stereo-model formation, a block of overlapping frame imaging products remains similar to that from traditional approaches of scanned films. They allow high geometric accuracy because interior orientation parameters and central perspective are controlled during calibration. Global Positioning System (GPS) / Inertial Measurement Unit (IMU) are optionally used to approximate the accuracy of aerial triangulation and reduce the number of required control points for block adjustment (Gruber and Leberl, 2007). Moreover, from sensor position and attitude angles, iterative adjustment methods can be initiated to solve nonlinear equations (with unknowns like sine and cosine angles). The approximation from the first iteration provides linearized equations since unknowns tend towards small angular corrections.

In linear imaging, image strip is a collection of 6 to 7 files each one of 4 colour channels in addition to 2 or 3 panchromatic strips for stereo works. Due to the fact that image strips are raw images lacking internal photogrammetric accuracy, geometric accuracy is obtained by direct geo-referencing of images thanks to the embedded GPS/ IMU data (Gruber and Leberl, 2007) and / or indirect georeferencing through GCPs. Obviously, the accuracy of image geometry depends on that of GPS/IMU measurements and of GCPs. In linear array, each element or detector take a line in either panchromatic or spectral bands. For example, Leica ADS40 acquires panchromatic and multispectral lines of 12 000 elements.

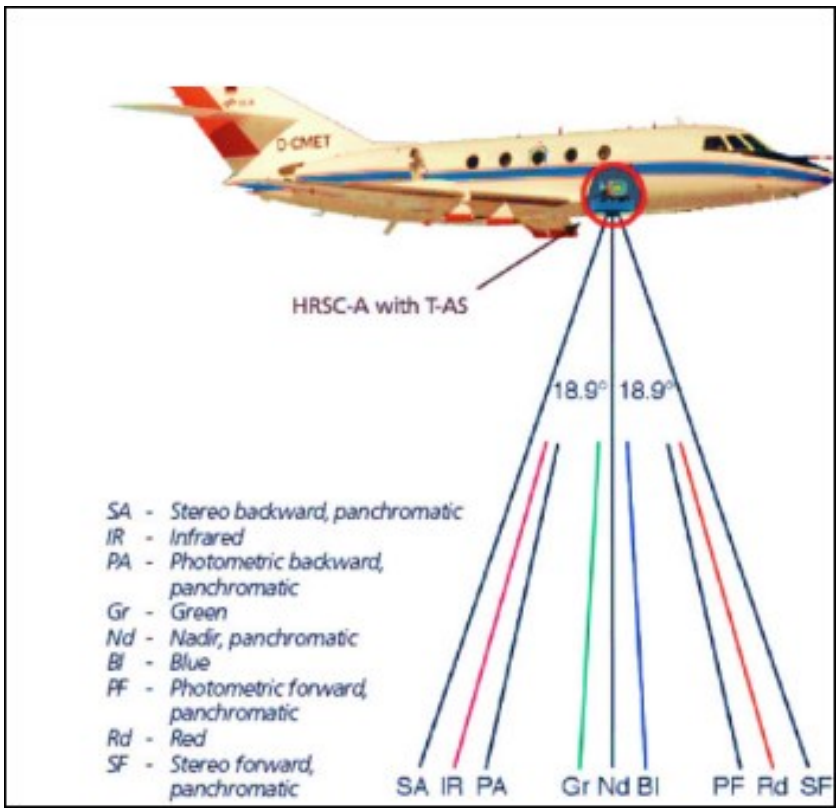

Figure 2: Imaging with ADS40 Camera, linear array of CCDs technology (Kheiri, 2006)

Figure 3: Raw image from ADS40 Camera (left), same rectified image (right) (Tempelmann et al., 2000)

As visible on figure 3, raw images are subjected to errors due to variations in sensor attitudes which results in some imperfections like for instance transformation of linear into curved features here illustrated.

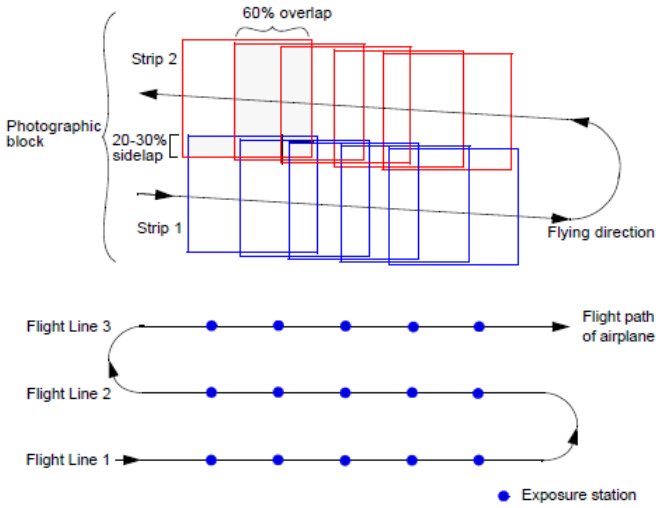

Figure 4: Block of aerial photographs and exposure stations of frame cameras (Hexagon geospatial, 2017)

Table 1: Linear and frame sensor parameters (Kheiri, 2006)

	Digital cameras technology		
Parameters	*Frame or area array of CCD*		*linear array of CCD*
Camera type	*DMC*	*UltraCam-D*	*ADS40*
Panchromatic focal length (mm)	*120*	*100*	*62.5*
Multispectral focal length (mm)	*25*	*28*	*62.5*
Pixel size (µm)	*12*	*9*	*6.5*
Number of pixels (panchromatic)	*13 500 x 8 000*	*11 500 x 7 500*	*2 x 12 000*
Number of pixels (Multispectral)	*3 000 x 2 000*	*4 000 x 2 700*	*12 000*
Field of view (°)	*77(cross track) x 44(along track)*	*55(cross track) x 35 (along track)*	*64°*
Radiometric resolution or dynamic range (bits)	*12*	*12*	*14*
Imaging rate	*2 frame/second*	*1 frame/second*	*830 lines/second*
Compatible GSP/IMU	*POS/AV 510*	*Aerocontrol AC by IGI Applanix POS AV*	*Applanix POS AV*
Forward stereo angles	-	-	*28°*
Backward stereo angles	-	-	*14°*

II.4. Satellite imagery

There exist various systems for remote sensing data collection. They can be grouped into the following ones (Ramapriyan, 2001):

Table 2: Categories of remote sensing data collection

Type of instrument	*Imagers, sounder, altimeter, radiometer, spectrometer*
Measured wavelength	*visible, near infrared, thermal infra-red, microwaves*
Geometric Mechanism of Platform the instrument	*Scanning, frame, push broom, whiskbroom imagers*
Platform	*Aircraft, spacecraft*
Sensing mechanism	*Passive, active*
Viewing characteristics	*Nadir, off-nadir, mono, stereo (bi- and tri-)*
Measured spectral characteristics	*panchromatic, multispectral, hyperspectral*
Spatial resolution	*(Very-)high, moderate, low*
Altitude and orbits	*Sun-synchronous, geosynchronous, geostationary,*

Regarding imaging types and their geometric models of acquisition, satellites sensors are specific and various. Pushbroom (examples: MERIS on board Envisat, QuickBird, IKONOS, HRS on board SPOT5/, Pleiades) and Whiskbroom sensors (examples: Landsat Thematic Mapper, AVHRR, SeaWiFS) have been developed. Compared to Whiskbroom, Pushbroom sensors are the most used for satellite photogrammetric purpose (Gupta and Hartley, 1997). Both are classified as linear CCD or line based scanner types, and they are able to produce imagery in different spectral channels. Not only they are installed on board satellite but they can also be designed as airborne systems (example: the pushbroom technology of Leica ADS-40).

A pushbroom sensor (or along track scanner) is a digital collector with a linear collection array made up of a line of elements (also called detectors), corresponding to the pixels of the acquired image. It is placed in the focal plane of the optical system and produces a two-dimensional (raster) scene (NGA, 2009) as the sensor moves. Thanks to multiple linear array of detectors (examples: 3 000 detectors for SPOT1-3 HRV instrument, 12 000 detectors for SPOT5 HRS and 30 000 detectors for Pleiades), pushbroom captures all pixels of the entire line across track at once.

Whiskbroom sensor (or across track scanner) scans each pixel of one or several lines (examples: 6 for Landsat/MSS and 16 for Landsat/TM) oriented across track at a time

(Aggarwal, n.d). Whiskbroom uses a rotating mirror to sweep out a scan line from one side of the sensor to the other perpendicular to the motion of platform of the sensor (Fowler, 2014).

Whiskbroom makes longer acquisition time range between stereopairs (at least 1 day), this increases the risks of land cover differences (due to human actions and humidity variation for example) and uneven cloud distribution on imagepairs (Poli, 2005). On contrary, acquisition time interval for pushbroom stereoviews varies from few minutes to seconds (Poli and Caravaggi, 2013). Obviously, time delay produces signature variation which can be harmful to automatic matching.

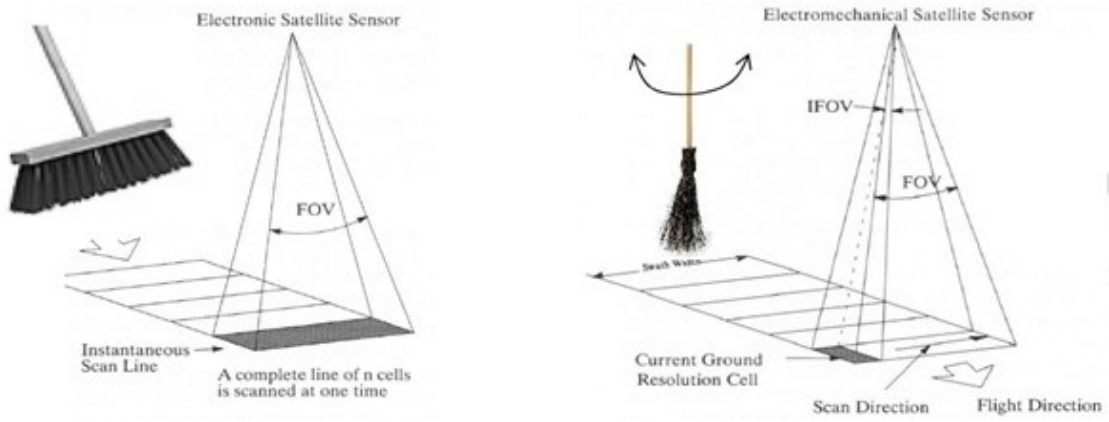

Figure 5: Left: Pushbroom scanning; Right: whiskbroom scanning concept

(http://www.florianhillen.de/studium/projekt/index.php?id=grundlagen&uid=sensoren)

II.4.1. Existing very high spatial resolution satellite sensors

Nowadays, most of commercially available high spatial resolution optical sensors are pushbroom sensors. Their altitude is usually between 300 to 850 km along near polar and retrograde orbits.Many of them are sun-synchronous orbits for the reason to cover the area at almost the same solar daytime (Poli, 2005) inducing constant illumination conditions except the seasonal varition for high lattitude. But this effect is easily normalized.

Table 3 summarizes important characteristics of (very-)high spatial resolution satellite sensors for photogrammetric mapping. Along-track and across-track mean respectively, quasi-simultaneous acquisition and acquisition from different orbits with time delay.

Table 3: Characteristics of some high spatial resolution sensors (Poli, 2005; Jacobsen *et al.*, 2008)

sensor characteristic		*Ikonos-2*[1]	*Quickbird-2*	*Geoeye-1*	*WorldView-1*	*Pleiades*	*SPOT5 HRS*[2]
Resolution resolution(GSD)		*0.82m Pan,3.28 m MS*	*0.6m Pan*[3]*, 2.4 m MS*[4]	*0.41m Pan, 1.65m MS*	*0.5m(nadir)-0.55 m (20° off-nadir) Pan*	*0.50 m Pan, 2m MS*	*2.5m &5m(nadir) Pan,10m MS,20m(nadir) SWIR*
spectral bands (μm)	*Pan*	*0.45-0.9*	*0.45-0.9*	*0.45-0.9*	*0.4-0.9*	*0.47-0.83*	*0.48-0.71*
	Blue	*0.445-0.516*	*0.45-0.52*	*0.45-0.51*	*none*	*0.42-0.55*	*none*
	Green	*0.506-0.595*	*0.52-0.6*	*0.52-0.58*	*none*	*0.50-0.62*	*0.50-0.59*
	Red	*0.632-0.698*	*0.63-0.69*	*0.655-0.690*	*none*	*0.59-0.71*	*0.61-0.68*
	NIR	*0.757-0.853*	*0.76-0.9*	*0.78-0.92*	*none*	*0.74-0.94*	*0.78-0.89*
	SWIR	*None*	*none*	*none*	*none*	*none*	*1.58-1.75*
Bit depth		*11 bits per pixel*	*11 bits per pixel*	*11 bits per pixel*	*11 bits per pixel*	*12 bits*	*8 bits*
image swath at nadir		*11km*	*16.5km*	*15.2km*	*17.7km*	*20 km*	*60 km to 80 km*
Revisit		*3 days*	*1-3.5days*		*1.7-5.4 days*	*Daily*	*1-3 days*
Altitude		*681km*	*450 km*	*681km*	*496km*	*694km*	*822km*
B/H		*Variable*	*Variable*	*Variable*	*Variable*	*0.25-0.4*	*0.84*
Stereo		*along track*	*along track*	*along track*	*along track*	*along track stereo and tristereo*	*across and along track*
Types of array sensor		*Pushbroom*	*Pushbroom*	*Pushbroom*	*Pushbroom*	*Pushbroom*	*Pushbroom*

[1] IKONOS-2 was decommissioned on 31st March 2015 (http://eoedu.belspo.be/en/satellites/ikonos.htm)

[2] SPOT5 has been decommissioned on 31st March 2015. HRS (High Resolution Stereoscopic) (http://www.satimagingcorp.com/satellite-sensors/other-satellite-sensors/spot-5/)

[3] Pan means panchromatic

[4] MS means multispectral

II.4.2. Processing levels

Satellite images recorded by (very-)high spatial resolution sensors are provided to users at different processing levels. In general, the latter are classified into following three categories:

a) *Raw products* are those close to original images acquired by the sensor (e.g.: level 1A of SPOT5/HRS). Their radiometry is normalized and calibrated without any geometric correction (Poli and Caravaggi, 2013). According to Spot image (2010) these images are radiometrically corrected by normalizing CCD values in order to compensate effects of detector sensitivity variation producing vertical stripping in the case of SPOT pushbroom instrumentation and horizontal stripping in the case of Landsat/MSS and TM technology. Raw images are provided together with their sensor and satellite metadata (internal calibration, attitude and ephemeris) either in form of rigorous sensor model or in their approximation form of RPC models to guarantee simplicity and full autonomy in photogrammetric image processing tasks (Spot image, 2010; Poli and Caravaggi, 2013).

b) *Geo-referenced products* (e.g.: SPOT5/HRG 1B level) are compensated for any systematic distortions produced by the sensor, the platform, the Earth curvature and rotation (Poli and Caravaggi, 2013) and variations in orbital attitude of satellites (Spot image, 2010). Being generated from raw images, they inherited their radiometric corrections plus supplementary adjustments.

c) *Map orientated products* (e.g.: SPOT 2A level) are georeferenced images which were orthorectified with respect to the accurate DEM (Digital Elevation Model) and GCPs provided by the producer (as default) or by the user (Poli and Caravaggi, 2013). This geometric processing eliminates the parallax deformation due to elevation variation when look direction is not vertical. It is very significant on high and very-high resolution images. Their metadata contains mostly their processing and the datum/map projection characteristics (Poli and Caravaggi, 2013). Higher product levels (level 3) exist. They are generally the result of spatio-temporal aggregation of several images during some specific time periods (e.g.: weekly or monthly product of Sea Surface Temperature from NOAA/AVHRR instrument). But they are not useful in our application.

Sometimes, depending on satellite images providers, the general processing levels and their specific corrections are not totally similar to the ones described above. This is the case for Pleiades 1A /1B images where only two types of products are distributed to the users under

names of *Primary* and *Ortho products* (Standard: georeferenced product free from terrain and off nadir effects, Tailored: products with more specialized corrections than standard). Both are corrected radiometrically and geometrically. The details on corrections of p*rimary products* are in chapter four. *Ortho products* have additional radiometric and geometric corrections than *Primary products* such as planimetric and altimetric reset using specific datum and map projections if GCPs and DEM are available, otherwise Shuttle Radar Topography Mission (SRTM) DSM is used (Astrium, 2012). In addition to that mosaicking of contiguous pass together with colour balancing, and pan-sharpening are carried out.

DEM and DSM are both digital models which differ from the fact that DEM deals with elevations above sea level while DSM often produced automatically from photogrammetric stereo images represents top faces of all terrain objects (manmade or vegetations) and terrain itself (Jedlička, 2009).

II.5. 3D restitution in digital photogrammetry

In digital photogrammetry, 3D objects extraction is possible from multiple images taken from different points of view in order for the images to contain a common zone called overlap.

In general, 3D restitution in digital photogrammetry requires three basic processing phases: interior or inner orientation, relative orientation and absolute orientation. The last two phases are often called external orientation. Specific input parameters during the restitution process are required for digital and analog aerial images and also for satellite images. In the following sections, restitution is described for analog and digital aerial images from frame cameras and for satellite images from (very-) high pushbroom resolution sensors.

II.5.1. Photogrammetric restitution from frame aerial images

Camera parameters which define the position of centre of perspective with respect to the image reference plane are essential for the interior orientation. They establish the relationship between image (pixel) coordinates and camera or sensor system so that internal camera geometry can be determined by reconstructing bundle of rays identical to those existed during image shooting. Inner orientation ensures collinearity between image point, perspective centre and object point and it is performed on images individually. This relationship is similar for analog and digital frame cameras (Karabork *et al.*, 2012).

Those parameters are provided by camera manufacturer in a calibration certificate and include *the principal distance* (focal length "f" or constant of the metric camera) and the position (ξ_o, η_o) of the principal point (Kraus and Waldhäusl, 1998). For better image geometry, radial and tangential distortions due to sensor's optical system imperfections are also modelled and corrected. For analog images, image coordinates also called pixel coordinates (in pixel units) are transformed into camera coordinates (in mm units) by a 2D affine transformation using fiducial marks whose camera coordinates are given in calibration certificate. For images acquired by frame digital sensors, the calibrated size of the CCDs array given in pixels and millimetres is used as coordinate system, in addition to the provided principal point coordinates.

Relative orientation consists of orienting cameras with respect to themselves in a stereo-model reference system so that conjugate rays intersect (Schenk, 2005). This is done by eliminating transversal parallax. This operation consists in resolving an equation with 5 independent unknowns so, calibrated coordinates of at least 5 homologous points have to be known.

On one hand, using dependent relative orientation (*orientation par enchaînement* in French) explained in Schenk (2005), it is possible to determine from these unknowns three rotation angles $d\omega$, $d\varphi$, $d\kappa$ and two translations terms which describe the orientation and the position of one bundle with respect to the others at the moment of acquisition. The two translation components are transverse translation (along y-axis) and vertical translation (along z-axis) measured relatively to the third translation component (along x-axis) which is generally fixed to 1.

On the other hand, independent orientation process (*méthode indépendante* in French) determines five rotation angles $d\varphi 1$, $d\kappa 1$, $d\varphi 2$, $d\kappa 2$ and $d\omega$ (Schenk, 2005). In order to form stereo-model, parallaxes are eliminated or at least reduced to very small and negligible values by selecting six standard points in overlap zone (figure 6) so that conjugate rays intersect or nearly intersect at a unique point. This process ensures coplanarity or quasi-coplanarity of both rays and base-line joining both centres of perspective. No external inputs are needed, only images coordinates of those six points and the outputs from inner orientation are sufficient for a perfect relative orientation.

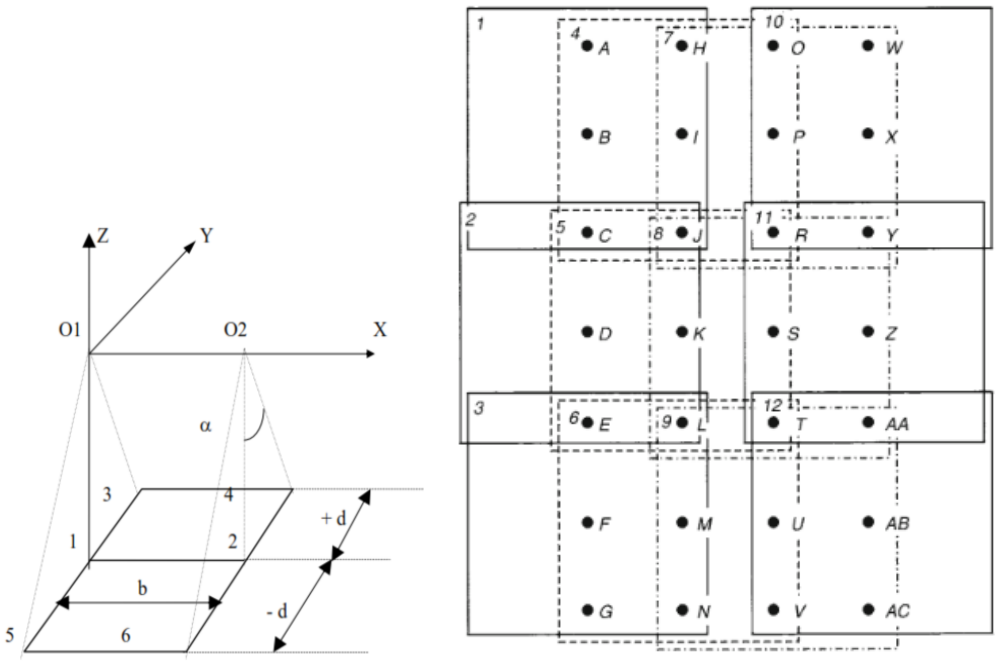

Figure 6:(left) Position of six standard points with O1 and O2, perspective centres of projection for stereo-photogrammetric acquisitions (Collignon, 2008-2009). (right) A block of 12 aerial images with different standard points (Kiema and Awange, 2013)

Created model being similar to the object model, it has an arbitrary scale, position and orientation, so, it has to be georeferenced to fit object's ground coordinate system. This constitutes the absolute orientation. It is performed using homologous points known in image-coordinates (and thus in stereo-model coordinates) and adjusting an Helmert transformation with 7 or 9 parameters; 1 or 3 scale factors, three rotation angles and three translation terms. So, at least 3 nonlinear points must be planimetrically and altimetrically known. During this orientation, direct geo-referenciation can also be performed by using coordinates of the perspective centres expressed in object's reference system and rotation angles derived from GPS/IMU measurement during image acquisition (Gomarasca, 2009).

Classically, the workflow of digital photogrammetry for stereo-restitution is summarized in the following (figure 7):

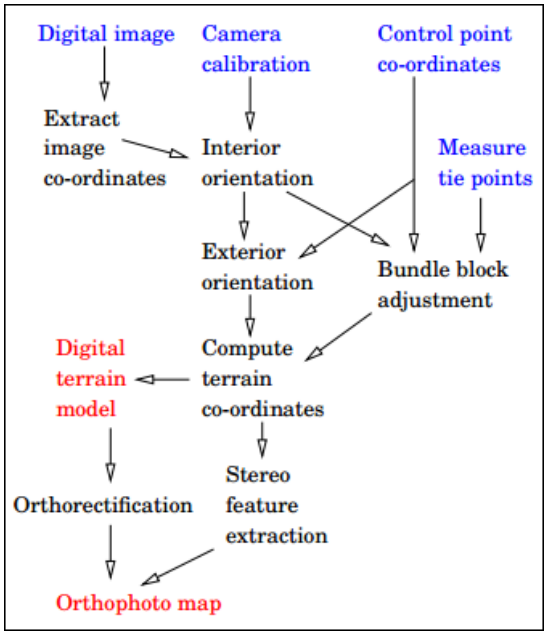

Figure 7: Photogrammetric workflow: inputs, processes, output (Vermeer and Ayehu, 2014)

II.5.2. Photogrammetric restitution from satellite imagery

In pushbroom design, four different coordinate systems relate image coordinates (column or sample and row or line positions) to object (ground or terrain) coordinates: the image coordinates system, the sensor coordinates system, the orbital coordinates system and the ground coordinates system (figure 8).

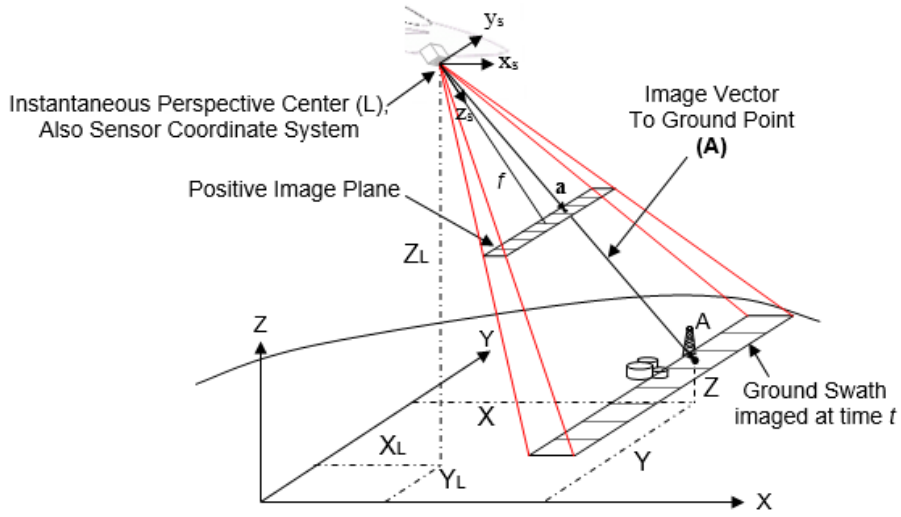

Figure 8: Acquisition geometry of pushbroom where (xs, ys, zs) are sensor coordinate system (NGA, 2009).

Acquisition by pushbroom sensors is time dependent, so, its geometric model is represented in the across track direction by planar central perspective and in the along track direction by

orthogonal perspective, thus, ray intersection of sparse resection techniques, provide inaccurate information for along-track locations (Gupta and Hartley, 1995; Gupta and Hartley, n.d). In fact, at a certain time, energy values measured by the detector array are recorded instantaneously. So, all pixels of a line are acquired at the same time, from the same position and with the same attitude. As each line is imaged independently (means at different time), it has its unique exterior orientation parameters ($x_{s(t)}$, $y_{s(t)}$, $z_{s(t)}$, $\Omega_{s(t)}$, $\Phi_{s(t)}$, $K_{s(t)}$) (NGA, 2009).

From the equation of collinearity expressed in Earth-fixed (or ground) coordinates system using the relationship between the four coordinate systems mentioned above, each pixel in the image has its corresponding object point. This means that for each line, those six exterior parameters have to be solved. Then, for all image lines, parameters and number of equations required become huge. Thus, a rigorous method rather than a simple bundle adjustment has to be used (Gupta and Hartley, 1995) in combination with sufficient heavy hardware resources during processing of pushbroom images.

As stated by NGA, (2009) in order to improve resolution of the unknowns, it is necessary to take into consideration that because of linear sensor geometry, generally, pitch(φ) angle is highly corrected with position along flight direction and roll angle (ω) with cross-strip linear displacement. Hence, auxiliary information is necessary such as sensor position, velocity and acceleration from GPS antenna or Doppler Orbitography and Radio positioning Integrated on Satellite (DORIS) system, values of angular orientation (pitch, roll, yaw) from onboard Inertial Navigation System (INS) or star tracker system and accurate distributed ground control points.

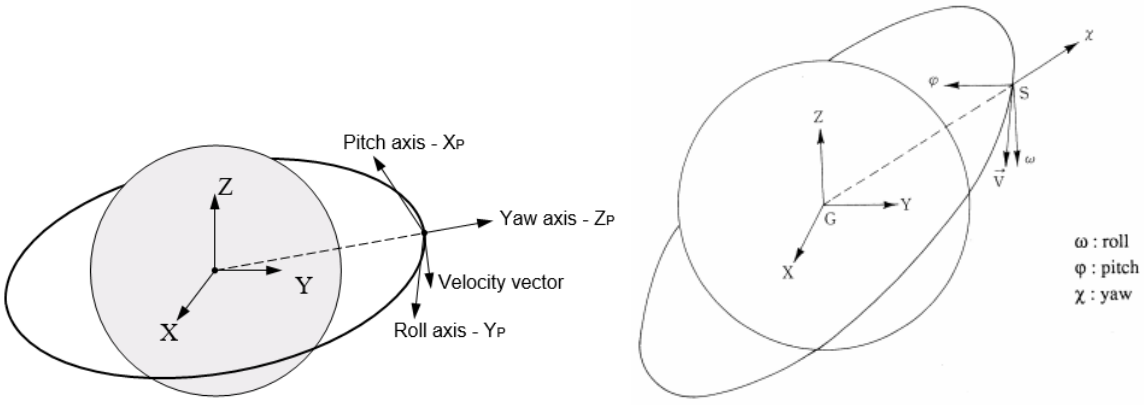

Figure 9: Position and attitude parameters for satellite platforms (NGA, 2009; JARS" platforms")

Nowadays, Earth observing satellites are equipped with so named direct sensor orientation which is a combination of a positioning system such as GPS or DORIS, together with attitude

control system such as gyros and star sensors (Jacobsen, 2007). Those instruments track satellite motion and orientation and provide continuously satellite position and attitudes angles data. This information together with internal calibration of sensor/platform system formulate collinearity equations, which relate each image point in image coordinates (column, row) to its corresponding object location in ground coordinate (X, Y, Z) (Zhou *et al*., 2015). This forms rigorous physical sensor model which is useful in satellite image processing.

However due to the fact that each scanned line has to be treated individually using its particular attitude parameters and that sensor model vary from sensor to sensor, the use of rigorous sensor model is obsolete. That's why empirical functions such as polynomial equations are preferred to approximate the sensor variation over time during the image acquisition (Shaker *et al*., 2010). The other advantage of empirical functions is that their structures are easily maintained because changes in sensor geometry or configuration do not require re-implementation of processing software (Rupnik *et al.,* 2016). The Rational Polynomial Coefficient (RPC) model is the mostly used polynomial approximation of sensor physical model for optical (very-)high spatial resolution satellite-sensors like Pleiades IKONOS, QuickBird, WorldView, GeoEye, Pleiades, SPOT 6/7 NAOMI, , , , etc. It is given by image provider in the metadata files.

RPC model is the ratio of two cubic functions of latitude, longitude, and height that provides conjugate image coordinates. RPC models have capacity to accomplish rigorous sensor model tasks in mapping; like direct georeferencing and image rectification, feature extraction and block adjustment.

Sensor modelling involves both interior orientation that contains optics and alignment construction and exterior orientation that includes ephemeris and attitude data. The RPC model incorporates interior and exterior orientations into equations in order to get 3D coordinates of objects from 2D image coordinates and inversely (Dial and Grodecki, 2005) as illustrated on (figure 10):

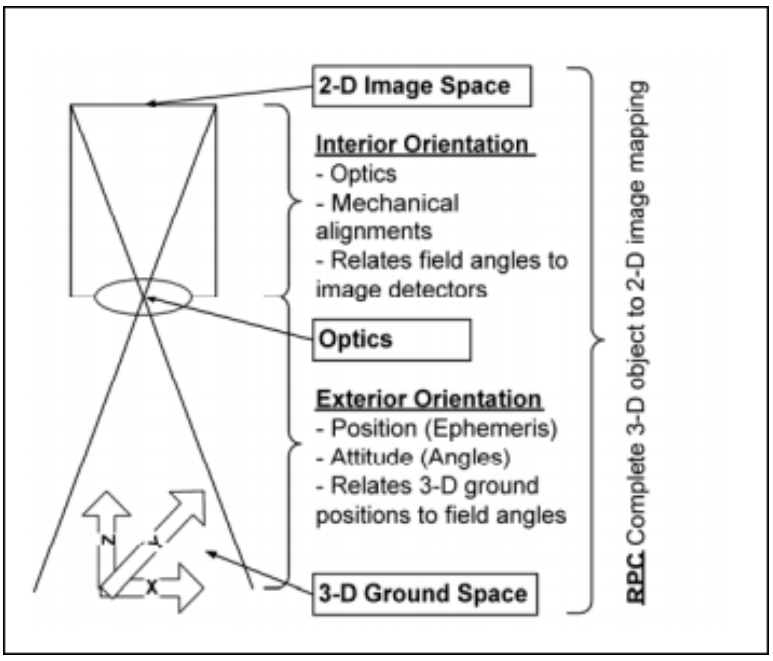

Figure 10: Complete RPC model (Dial and Grodecki, 2005)

RPC metadata files contain both direct analytic model (Image toward Ground) and inverse analytic model (Ground towards Image), each expressed in terms of coefficients: 20 numerator coefficients and 20 denominator coefficients for line and sample coordinates for Pleiades. Those coefficients are used in RPC equations to compute image coordinates as sample or column and line or row positions from object coordinates (φ, λ, h) and vice versa (Dial and Grodecki, 2005). Generally, φ, λ are coordinates in WGS84 datum while h is the orthometric height.

The following equations express the inverse analytical model. $\mathrm{RPC}_{\mathrm{row}}$ and $\mathrm{RPC}_{\mathrm{col}}$ functions are adjusted using the measured ephemeris, attitude and physical sensor model (d'Angelo and Reinartz, 2012):

$$r = RPC_{row}(\varphi, \lambda, h) \quad (4)$$

$$c = RPC_{col}(\varphi, \lambda, h) \quad (5)$$

Even if some software integrates well sensor data to produce accurate exterior orientation which is able to generate accurate products (like 4m IKONOS without GCPs as an example) suitable for mapping at 1:10 000 scales without requiring ground control (Dial and Grodecki, 2005), RPC model is not sufficiently accurate to generate reliable surface models (d'Angelo and Reinartz, 2012). Therefore, the positioning biases are corrected through RPC refinement. This refinement as stated by Rupnik, *et al.* (2016) and Hu *et al.* (n.d) can be done either directly by modifying original RPC with the aid of GCPs or indirectly by correcting errors using

polynomial functions that model differences between true terrain coordinates and coordinates computed using direct analytical RPC model.

II.6. 3D products from (very-)high spatial resolution satellite and aerial images

Stereo-pairs of (very-)high resolution satellite images are suitable to produce DSMs (d'Angelo and Reinartz, 2012) thanks to direct orientation parameters contained in RPC as explained in previous sections.

Satellites images have been evaluated and confirmed to fit the requirements of mapping at certain scales; Hu *et al*. (2016) based on the accuracy evaluation of DEM generated from stereo-pairs of Worldview-3 agreed on its use in mapping application at 1:5000 scale or smaller. After radiometric and geometric analysis of Pleiades 1B images, Agrafiotis and Geogopoulos (2015) found that they can replace aerial images in large scale orthoimage production when evenly distributed control points are used for orientation model refinement. By evaluating 3D geometrical restitution accuracy of Worldview2 images and aerial images from UltraCamX cameras, both dataset was validated in topographic mapping of 1:5000 scale (Yilmaz *et al*., 2016).

II.7. MICMAC in 3D production

The automation of 3D object reconstruction from photographs has been greatly improved since early 1990[ies] thanks to computer vision (according to Förstner and Wrobel (2016) computer vision is a science and technology of obtaining information about the physical environment from images) methods with the aid of analytical and numeric photogrammetry. The so-called Structure from Motion (SfM) expanded its domain of application, it consists firstly of feature detection and matching which produce homologous (or tie) points and secondly of using those automatically detected tie points as input of bundles adjustment and dense 3D models' computation (Galland *et al*., 2016). As respectively described by Lowe (1999, 2004), Bay *et al*. (2006), Morel and Yu (2009), feature detection and matching may be performed by algorithms like Scale Invariant Feature Transform (SIFT), Speeded Up Robust Features (SURF) or Affine SIFT (ASIFT).

Commercial (like Agisoft Photoscan Pro, Pix4Dmapper Pro) as well as open source software (such as OpenMVG, VisualSFM, OpenSFM, Python Photogrammetry toolbox) implement SfM concept. Open source software is preferable than commercial software based on the fact

that the latter is less controlled by users which is scientifically a disadvantage and expensive. SfM based on open source software like VisualSFM and Python Photogrammetry toolbox have the capacity of integrating other software to get a complete tool necessary for 3D object reconstruction but they lack georeferencing tools (Moutinho, 2015).

Since 2005, an open source photogrammetric software MICMAC that implements SfM algorithm, precisely SIFT has been developed at French Geographical Institute (*Institut National de l'Information Géographique et Forestière*).

SIFT has been proved to be the best performance regarding geometrical change among other local invariant feature descriptors on greyscale images (Mikolajczyk and Schmid, 2005) and limited on colour images (Abdel-Hakim and Farag, 2006). However, Govender (2009) shown that SIFT performs better than SURF and Harris corner detectors on daytime outdoor images taken with changes in illumination and vehicle speed. Some algorithms have been proposed to improve matching by including colour information of MSS images for instance in (Farag and Abdel-Hakim, 2004) and the inclusion of colour invariance in CSIFT described by (Abdel-Hakim and Farag, 2006).

Being known for its capacity in tie points computation, bundle adjustment for relative and absolute orientation and in-depth maps creation, this software is designed into two main libraries: ***APERO*** (*Aérotriangulation Photogrammétrique Expérimentale Relativement Opérationnelle*) for image orientation computation and ***MICMAC*** for depth maps and 3D cloud points generation from orientated images (Georgantas *et al*., 2012).

MICMAC is powerful for 3D models' production from stereo or tri-stereo satellites images and multiple aerial images. In processing, it uses several tools all accessible using one command ***mm3d***. However, it is not simple for unexperimented and new users as it lacks graphical interfaces, runs well on Linux machine rather than on windows and even if its technico-scientifical documentation is continuously improving, it is not very explicit and complete.

Whether satellites or aerial images are to be processed, the general workflow for 3D models' generation is summarized into four complex tools (Pierrot-Deseilligny, 2017):

a) ***PASTIS*** (*Programme Autopano Sift pour les Tie points dans les ImageS*) tool, an interface to SIFT for tie points computation.

b) ***APERO*** tool, for internal, relative and absolute orientations from tie points and GCPs and/or GPS/IMU data.

c) ***MICMAC*** tool, for dense image matching process according to the results from ***APERO***.

d) For orthophoto extraction, ***PORTO*** tool is used.

MICMAC provides the possibility to use simplified tools instead of the above complex tools in carrying out photogrammetric workflow of images. Simplified tools are designed as interfaces of their respective complex tools and are often used as they don't require advanced computer skills.

MICMAC offers to users, the possibility to specify some parameters for computation effectiveness. As an example, the user may select among a set of images, optimal images from which the initial orientation should be calculated. The user can also assign the confidence to the observations that will be transmitted to ***APERO*** during bundle adjustment as weighting functions (Pierrot-Deseilligny, 2017).

CHAPTER III. : RESEARCH HYPOTHESIS

In this chapter, research hypothesis was highlighted and the study area was described together with the reason of its choice.

III.1. Hypothesis

Since the beginning of photogrammetry, aerial imagery was mostly used in precise topographic mapping applications mainly due to its (very-)high ground resolution. With the affordable (very-)high resolution satellite imagery that provides larger spatial coverage compared to aerial imagery, very large-scale 3D data can also be collected from satellite products. But the question that arise is; which is the specific quality of 3D models produced by both aerial and satellites data. Thus, we aim to demonstrate that the geometric quality of 3D models from existing (very-)high spatial resolution satellite imagery is as accurate as the ones produced from aerial digital imagery with similar resolution when using currently available open source software.

In this regard, the hypothesis of the study was that, by using MICMAC software, the geometric accuracy of DSM and orthoimage products generated from a stereo-pair of Pleiades images is equivalent to those products generated from UltraCam Falcon aerial camera and that their structural richness specially to describe the 3D geometry of build-up area is similar.

III.2. Study area description

For practical reasons in addition to the only available Pleiades archive stereo-pair on Walloon region, this hypothesis was demonstrated in the area of Liège in Belgium. But also, the availability of reference datasets of the Walloon geoportal and the closeness of the study area to the University for field surveys (GNSS) effectiveness justified practically this choice.

As explained by Tihon *et al.*, (2005), due to the presence of Meuse, Ourthe and Vesdre valleys that cut three geomorphologic domains; the Hesbaye plateau, the Plateau de Herve and the Condroz, this area is characterized by a hilly landscape with quite important altitude variations (60 to more than 300 m elevation) and steep slopes. Furthermore, landcover is also diversified with dense urban to low density peri-urban area, farmlands, pastures and forests. This means that the quality of the photogrammetric products generated from aerial and satellite imagery was compared in different morphological and landcover contexts. Precisely, the study area is located on the western side of Liège city. It includes large parts of districts such as Liège, Saint Nicolas, Grâce-Hologne, Seraing, Flémale and small parts of Chaudfontaine, Esneux, Neupré,

Ans, Awans, Fexhe-le-Haut-Clocher and Engis. In this zone, the altitude ranges from 60 m in the valley to 280 m in the Condroz and Condroz ardennais plateau southward (figure 11).

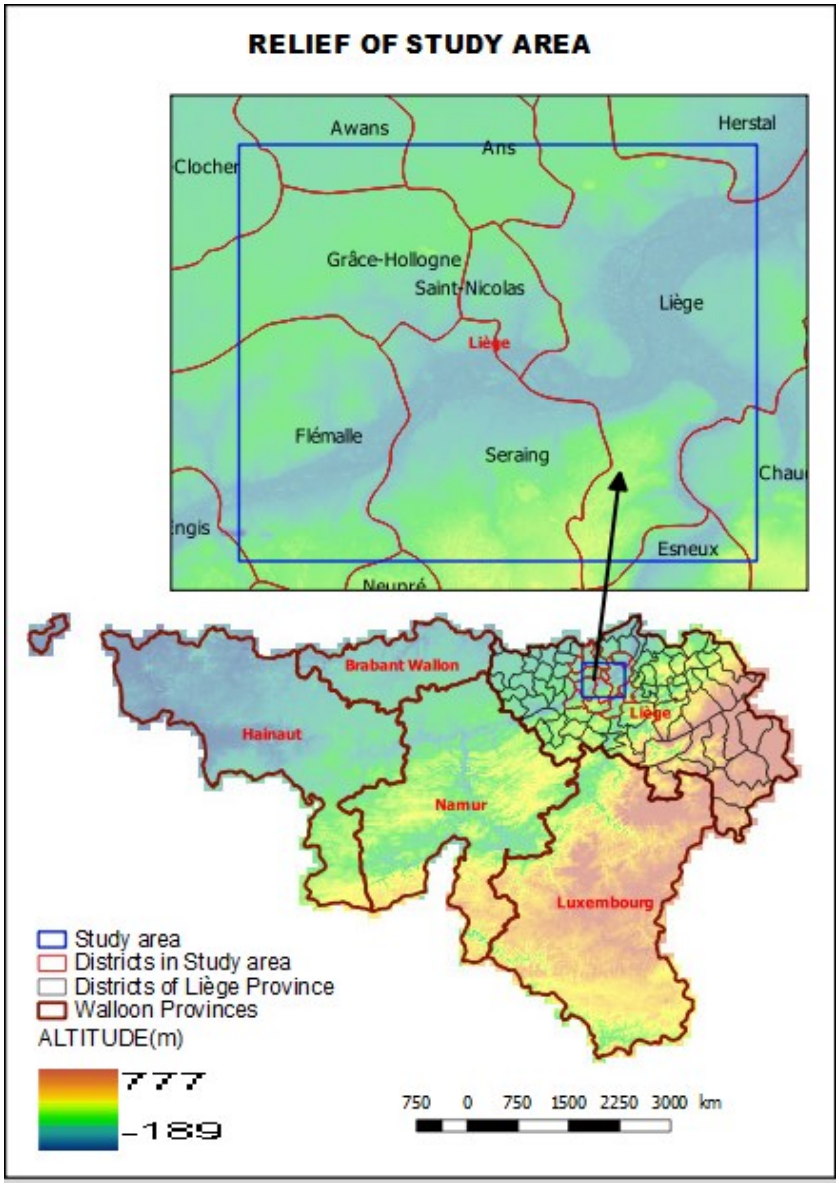

Figure 11[5]: Relief map of Liège area

[5] The background image is the Walloon DSM found from WalOnMap geoportal. The access agreement doesn't allow any modification to users that is the reason why the map doesn't satisfy standard symbology.

CHAPTER IV. : DATA DESCRIPTION AND PHOTOGRAMMETRIC PROCESSING

As shown on figure 12, our research has been performed in several phases; The first phase involves data collection. Firstly, it consisted of image selection and ordering from existing archive datasets and secondly, of field work. In first section, this phase is detailed and quality of collected data is described. After preparing relevant inputs in compatible file formats, photogrammetric processing using MICMAC was applied. All steps used to produce photogrammetric products were explained in second section of this chapter.

Lastly, the analysis of the obtained photogrammetric products made the final phase. This analysis was depicted in chapter five as the assessment of geometric, radiometric and structural quality of output products from which hypothesis was validated and discussed.

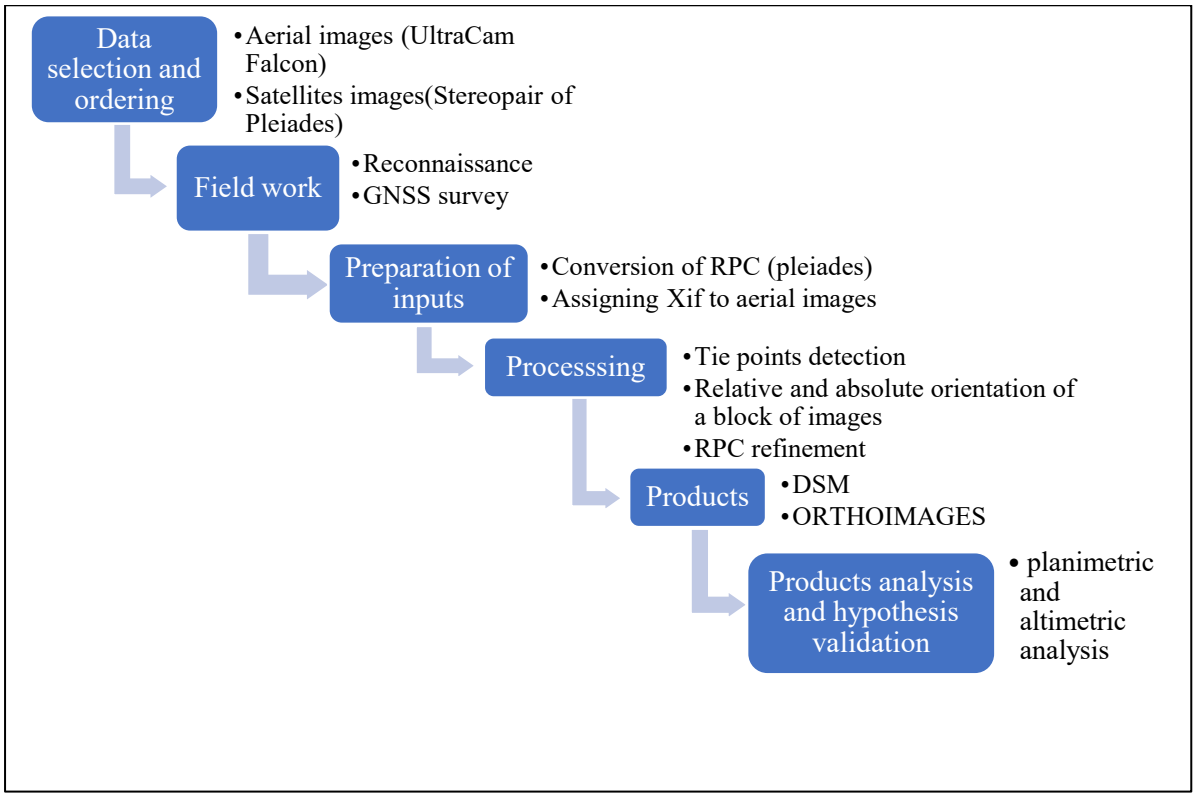

Figure 12: Workflow chart.

IV.1. Qualification of used data

In this research both secondary and primary data were used for gathering the objectives and enabling hypothesis validation. For the aim to geometrically and structurally assess and compare the quality of 3D products, two secondary datasets were used: aerial images and

Pleiades satellite. Primary data consisted of GCPs necessary for absolute orientation during photogrammetric processing of those images.

IV.1.1. Secondary data

Aerial image dataset

UltraCam digital aerial cameras of Vexcel Imaging are well known for their geometric capability and operability that provide full exposure control (aperture, shutter speed) across terrain and increase stability and accuracy within each frame better than 2 microns. Furthermore, the presence of integrated GPS/IMU provides ancillary data for each exposure (Microsoft UltraCam Team, 2012). Since 2003, with the introduction of UltraCam D, the company produced many more cameras in order to meet customers' requirements in practical works (figure 13).

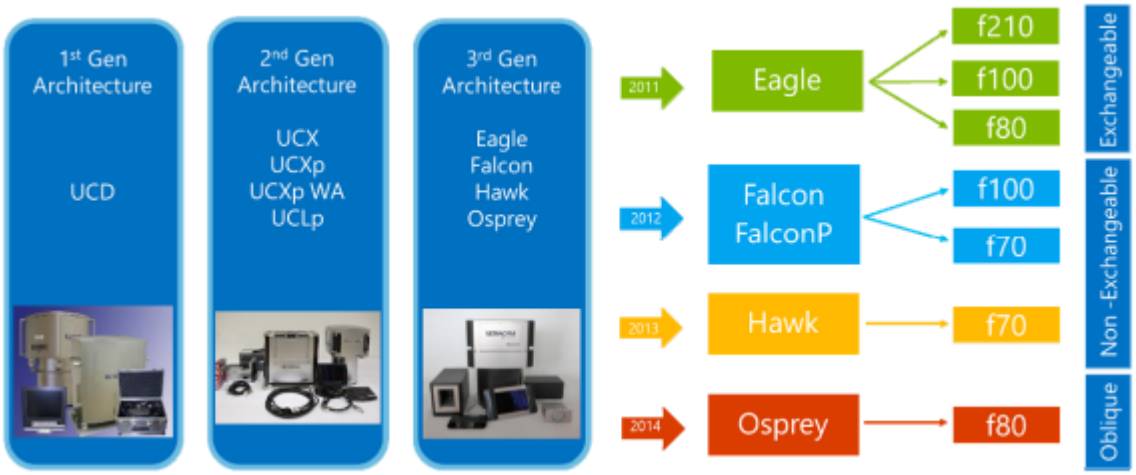

Figure 13: Evolution of UltraCam cameras (Wiechert and Gruber, 2015).

The third generation consisted of nadir cameras such as UltraCam Eagle, Falcon Prime, Falcon and Hawk and oblique cameras like UltraCam Osprey. All cameras are supported by UltraMap software for processing procedures such as aerial triangulation, dense matching and orthoimage production.

UltraCam Falcon also named UltraCam Prime was firstly introduced in 2012. This camera provides possibility to buyers to choose focal length (wide range of 70mm or standard of 100 mm), image size (14 430 height * 9 420 width pixels or 17 310 height * 11 310 width pixels for panchromatic image) and housing configuration (choice of a fully integrated system or separate sensor head and external computer/storage unit). The sensor carries 8 lenses which enable to capture stereo images. For operational simplicity, Falcon is manufactured as an

integrated unit enclosing all sensor head components for instance a solid-state image storage system of about 7500 images for 14 430 pixels height and 5 200 mages with 17 310 pixels height (https://ultracam.wordpress.com/page/7/). Being designed with a unique sensor system and available at different prices Falcon allows budget restriction in various project requirements.

Typical flight height ranges from 1700 m to 10 000 m maximum. For large area projects, large focal length and wide image size are preferable for rapid data acquisition at high altitude. During data acquisition, panchromatic, visible and NIR data with respectively 6 µm and 18 µm of physical pixel size is captured in a single pass. The embedded GNSS/INS system is UltraNav (Applanix POSTrack OEM) and pan sharpen ratio is 1:3 to allow production of multispectral data at pixel size equivalent to that of panchromatic data (http://www.vexcel-imaging.com).

From surveying direction in geomatics department of Wallonia public service (*Service Public Wallon*), a set of 112 multispectral (MSS) images sensed into 6 strips at nadir by the UltraCam Falcon aerial digital camera with serial number S/N UC-Fp-1-40616106-f100 was given. Its focal length is 100.5 mm and the principal point (PP) is located at centre of the CCD array (see table 4). Radial distortion is very small (less than 2 microns). The flight mission has been performed in 2015 between 12th and 15th April as seen in annex I. Its aim was to produce a mosaic of orthoimages for agricultural parcel control. That's the reason of the early summer flight when parcels are not laboured and vegetation cover is present. NIR band was also sensed for this purpose.

Each image has 17 310 columns and 11 310 rows corresponding to the image format of 103.860 x 67.860 mm (figure 14). As the flight height above ground level was ~3 900 m, the GSD corresponding to the focal length and the array size was ~23 cm which is approximate to theoretical GSD of 25cm. The aerial scale was 1/39 861 and the distance between two cameras were ~ 1 047m with overlap of 60 % and base to height ratio (B/H) of ~0.27. This ratio is rather smaller to the optimal range of stereo aerial pairs of 0.5 to 1.0 and can probably affect the accuracy of automatic DEM generation as proved by Hasegawa *et al.* (2000) that for ratio lower than 0.5, height accuracy decreases as the ratio decreases.

In processing point of view, aerial images sensed by this UltraCam Falcon camera are the results of a pan sharpening. This is an image processing in which multispectral images are upscaled at high spatial resolution of their corresponding panchromatic images and both fused

to produce multispectral bands at spatial resolution of the panchromatic record. Images were level 3 (i.e. obtained after 270° rotation of images in clockwise direction). flight direction was Eastward with the following image coordinate system (figure 14):

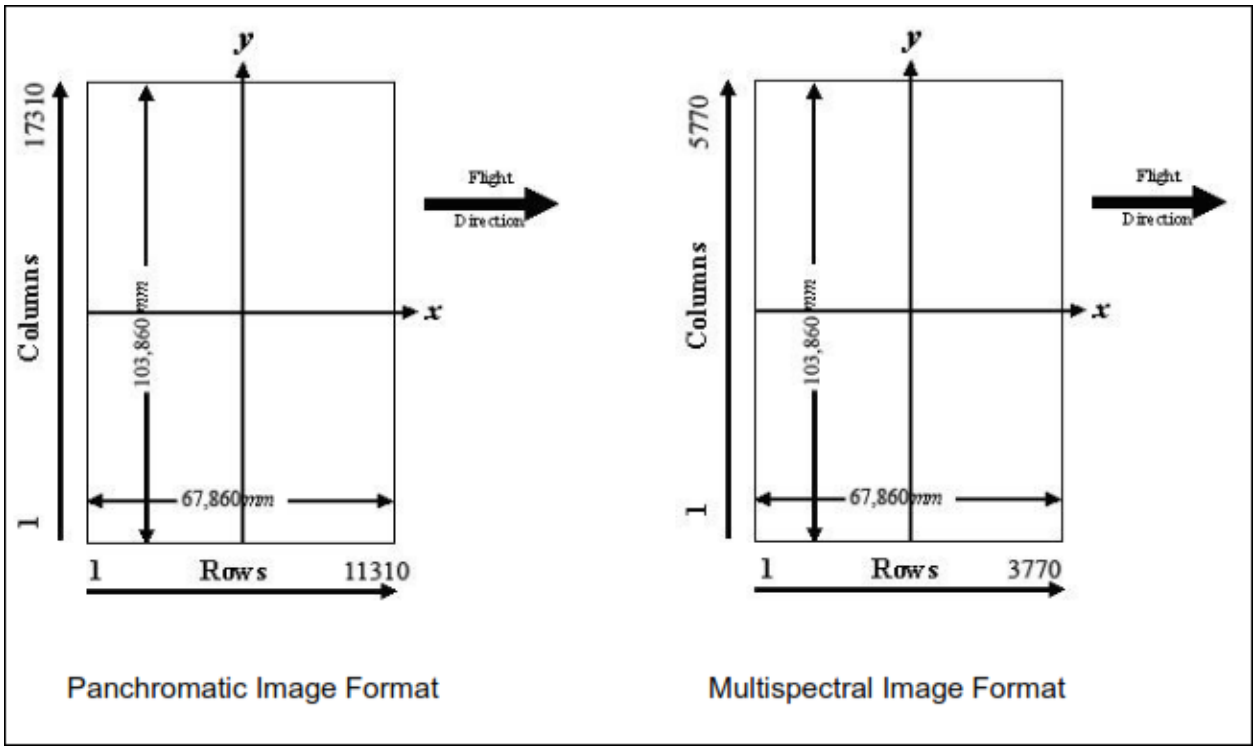

Figure 14: Image coordinates system of level 3 images

To remove camera imperfections due to lens systems, a number of calibration methods have been carried out such as: geometric calibration, radiometric calibration, verification of lens quality and sensor adjustment, calibration of defective pixel, shutter calibration, sensor and electronic calibration. The details about these calibrations are found in camera calibration report in annex A.

Table 4: Summary of characteristics of aerial images

Sun elevation (°)	*43*
Radiometric resolution (bits)	*32*
Mean flight height (m)	*3880 (~3900)*
Average B/H	*0.27*
Average Photo scale (m)	*39861*
GSD (m)	*~0.23**
Overlap	*60%**
Side-lap	*30%**
Pan sharpened	*Yes*
Planimetric precision (m)	*0.97*
Focal length(mm)	*100.5*
Position of PP (mm)	*X=Y=0.000***
Precision of PP (mm)	*± 0.002***
Distortion (mm)	*0.002***
MSS bands	*Red, Green, Bleu, NIR*

* This information is specific to the aerial image acquisition mission performed by AERODATA on demand of the geomatics department of Walloon public service to produce the mosaic of orthoimages of the country in 2015 (http://geoportail.wallonie.be/walonmap)

** This information is specific to the camera UltraCam Falcon with serial number S/N UC-Fp-1-40616106-f100 as read from calibration certificate (See annex A)

Satellite images dataset

Pleiades 1A satellite was launched in 16 December 2011 and its twin Pleiades 1B in 2012. Both operate as a constellation in the same orbit, phased 180° apart (Airbus Defense and Space, 2017). For civil users, Pleiades products exist with primary correction at 0.5 m of spatial resolution in panchromatic mode which is useful in photogrammetry and 2.8 m for multispectral mode (Astrium, 2012). The interests of Pleiades rely not only on its spatially accurate products but also to daily worldwide revisit suitable for daily change detection (Airbus Defense and Space, 2017). In addition, the ability to provide stereo and tristereo products (figure 15) from the same pass of the area improves mapping quality from 3D models for mountainous and high-rise building areas.

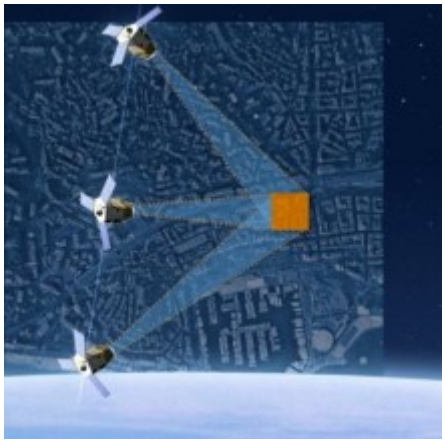

Figure 15: Stereo and tri-stereo Pleiades acquisition (Astrium, 2012)

With stereo images, it is likely to have occlusions on images of mountainous or high-rise building areas as illustrated on figure 20. Effect of sun elevation on stereo pairs or triplets is also pronounced as the smaller is sun elevation, the longer is the shadow in the sun's opposite direction. Depending on the latitude of the area, different daytime and season combinations produce ideal sun elevation (figure 16).

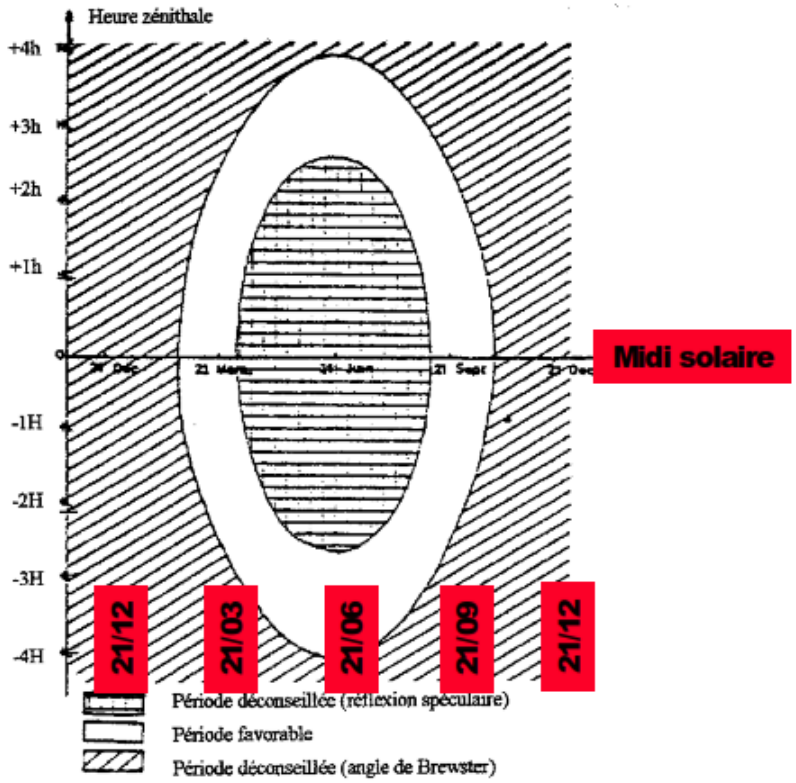

Figure 16: Ideal daytime and season combination for remote sensing imaging in mid-latitude countries (Lefèvre et al.,1984).

Both shadows and occlusions have a negative effect on the quality of matching. By adding nadir view as on figure 17, the quality of matching and accuracy of 3D models is improved. Furthermore, the season of acquisition depends on the application domain. The period between late autumn and early spring are propitious for photogrammetric application because of absence of vegetative activity if sun elevation is sufficiently high. For agriculture and forestry applications, this period is to be avoided.

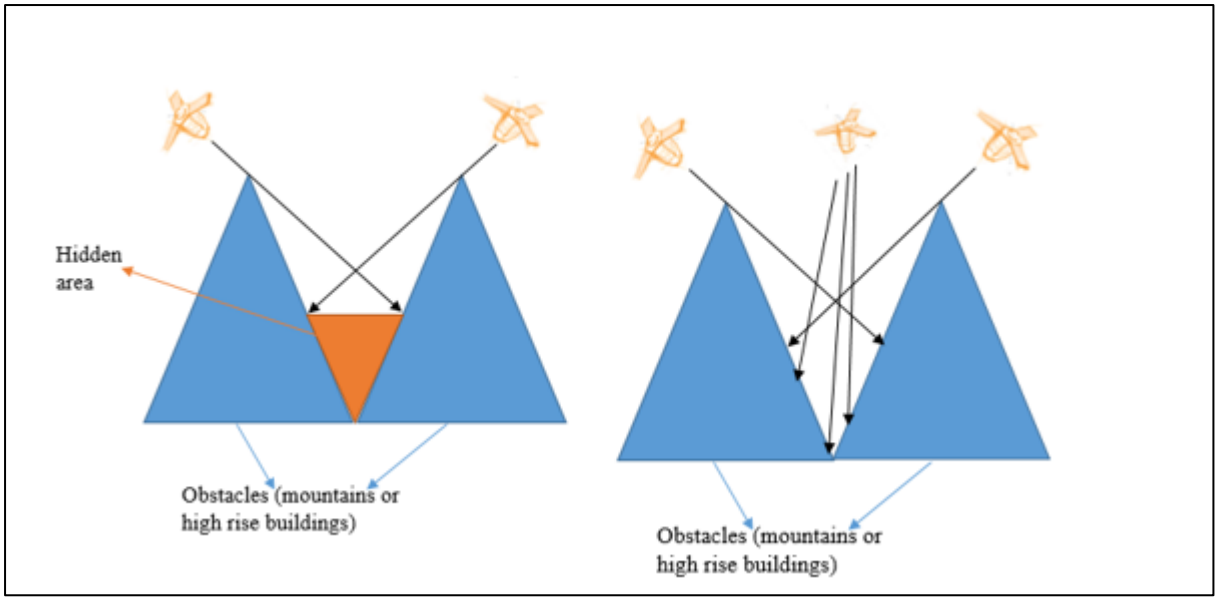

Figure 17: Advantages of tri-stereo-viewing in mountainous or high building areas (Astrium, 2012; modified).

As specified by Astrium (2012) primary products of Pleiades satellites undergo the following geometric processing:

- The combination of all sub-swaths across in the field of view (20 km nadir condition): synthesis in a virtual focal plane represented by a single linear array for all spectral bands;
- Correction of instrumental and optical distortions: viewing angles adjusted to the single linear array model;
- Co-registration of all spectral bands: multispectral and panchromatic;
- Attitudes and ephemeris data are refined at ground on the mean estimation:
    - Adjustment of the time stamp sampling (along scan line),

- Attitudes filtering during time of acquisition or *posteriori* extended over several orbits (Refined Attitude Data);

- Consistent alignment of the physical model ancillary data and RPC analytic model data.

According to Astrium (2012), the main radiometric corrections of Pleiades primary images are:

- Inter-detector equalization: on board correction of differences in sensitivity between the detectors;
- Aberrant detectors correction;
- Panchromatic band restored and denoised;
- Pixel sampling at Shannon optimizing image quality for downstream value-added processing: Spline kernel resampling into the Primary geometry in order to get spatial resolution of 0.5 m for panchromatic and of 2 m for multispectral images in nadir condition.

Pleiades products are produced at different angular products called ratio B/H. B/H influences the accuracy of the photogrammetric processing and the resulting DEM. The relationship between height accuracy δZ and planimetric accuracy δp is:

$\delta Z = (\frac{H}{B})\delta p$ (6) where higher accuracy means lower δZ.

δZ is inversely proportional to B/H in equation (6). So, the lower B/H ratio implies lower accuracy and vice versa.

According to Astrium (2012), the best range of B/H ratio for accurate automatic 3D products from stereo images of Pleiades is 0.25 to 0.40 given that possible values are between 0.15 and 0.6 for stereo and from 0.3 to 0.8 for tristereo. In flat area with small buildings, high B/H ratio is possible as there are no hidden parts due to buildings or mountains as illustrated (on figure 18).

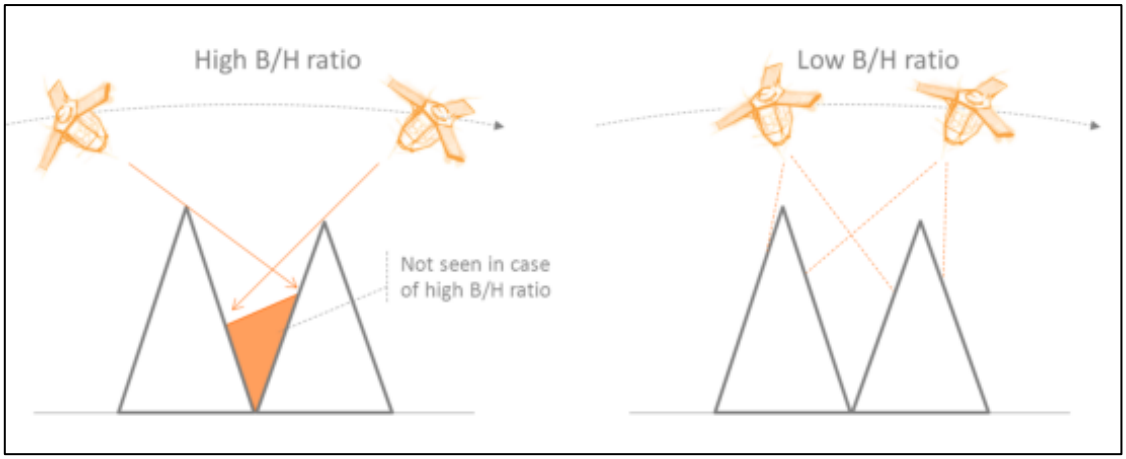

Figure 18 : Influence of high and low B/H ratio (Astrium, 2012).

For our experiment, to prevent excessive costs and image quality randomness due to the presence of clouds and unmanaged time delay in case of tasking plans, we searched for stereopairs or tri-stereo triplets available in the Pleiades archives accessible on the Airbus-Astrium Geostore portal (http://www.intelligence-airbusds.com/en/4871-browse-and-order). Only one stereopair of Pleiades 1A was available on the Western area of Liège. A subset of this pair covering 122 km² was clipped and bought from Airbus Defense and Space Geo SA (see annex B). Beyond primary corrections, stereopair was delivered with pixel's values in top of atmosphere normalized reflectance and systematic errors free.

The sensing date is 13th March 2015 and daytime are respectively 10:39:24 UTC and 10:39:53 along the same descending track (see annex B). So, the first image has been acquired looking in the south-west direction with incidence angle of ~20° (figure 19) while the second image has been acquired looking in the north-west direction with incidence angle of ~15°. This acquisition date corresponds to early spring without any green canopy in deciduous forest area and early phenological stage in agricultural and pasture zones. The geometric configuration of the pair produces a B/H ratio of the stereo data of 0.33(see annex B and table 6) which is sufficient to get accurate 3D models. However, occlusions on western side of steep hills and buildings are present (figure 20). Sun elevation angle is quite small (34.6°) and shadow length is thus large.

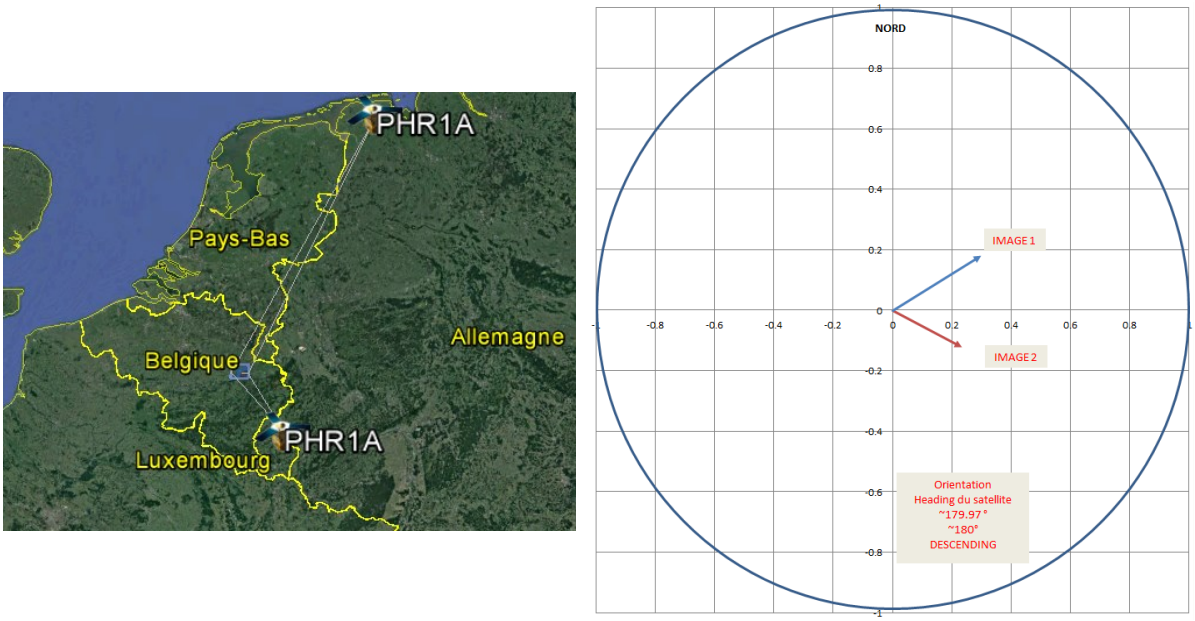

Figure 19: Position of the satellite on a sky-plot (orthogonal projection of the sensor position vector at the target point) for each acquisition of the stereo pair.

Table 5: Characteristics of satellite data used

Stereo pair	Acquisition date and daytime	Snow cover	Cloud cover	GSD	Pre-processing level	B/H	Observation incidence	Sun elevation	Detectors (panchro)
First image	March,2015 10:39:24 and 10:39:53	0%	0%	0.5 m	Primary + reflectance corrections	0.33	20.1°	34.6	30000
Second image			1%				15.0°		

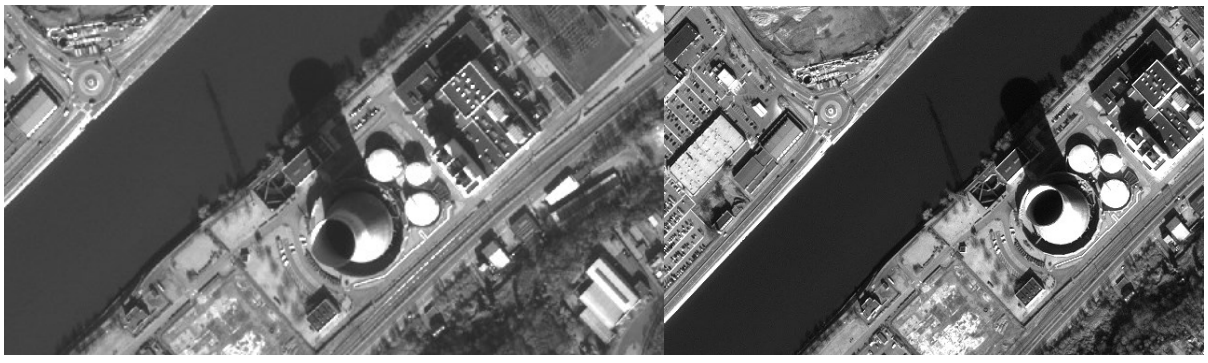

Figure 20: Occlusion and shadow on the first image acquired of Pleiades' stereo pair (left) and on the second image acquired (right).

Spatial comparison of Pleiades and Vexcel images

A difference of 25 cm in GSD between Pleiades and Vexcel images make an important difference in details that can be seen on both datasets. This affects also the nature of points that are to be chosen as GCPs. Very well and contrasted objects must be selected. This is generally negative for Pleiades images in positionning GCPs (figure 21). Furthermore a slant effect is clearly visible on Pleiades images due to viewing obliquity.

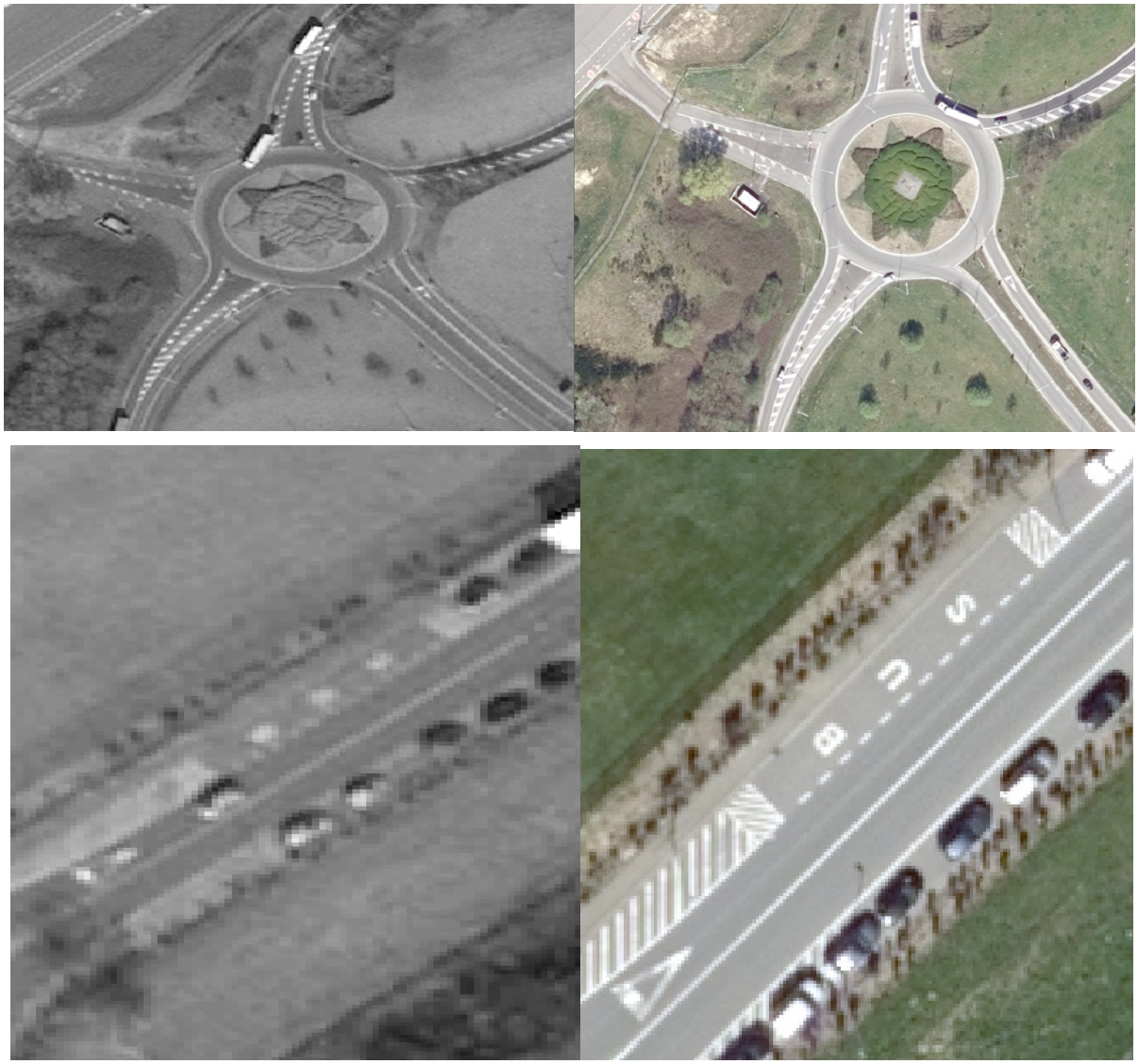

Figure 21: Difference in details visualisation between Pleiades (left) and Vexcel (right) images

Cost of aerial image acquisition mission and Pleiades images per square km is a useful information for operational purposes. The price of Pleiades' stereopair was 5.74 €/km² (2*2.87 €/km²) for optimal clients, and 8.12 €/km² (2*4.06 €/km²) in general. Unfortunately, we didn't get any information about 2015 aerial mission cost of used Vexcel images.

IV.1.2. Primary data

Photogrammetric processing requires a number of points whose coordinates are known in terrestrial coordinates system in order to perform the external bundle orientation or in refinement of RPC. Specifically, thanks to GCPs, orientated images can be orthorectified in object based coordinate system and 3D models can be produced.

In order to get accurate measurements, surveyed GCPs were chosen as ground points clearly identifiable and localisable without any ambiguity on the images. We also selected points evenly distributed and describing the topographical features of the zone. Real Time Kinematic (RTK) mode of GNSS positioning was used to measure precise terrestrial coordinates in carrier phase measurement by transmitting real time corrections from Wallonia Continuously Operating Reference Station (WALCORS base stations) to the Trimble R10 Rover Receiver that was used.

Reconnaissance

Like in large and short surveying tasks, a well-designed preliminary study of the area is necessary in order to understand possible troubles that would be met on the field and to get relevant information about the area so that the field survey should be effective and rapid. In this regard, an orthophoto with 25 cm GSD of Walloon region of 2015 was used to identify *a priori* positions of ground points to be surveyed as ideal points visible on both Vexcel and Pleiades images.

The processing of multiple strips of aerial images requires GCPs spatially distributed in a strong geometric configuration. According to Hexagon Geospatial (2017), GCPs should be measured at each first and last corner image in the strip and in a zone common to multiple images to ensure perfect configuration as illustrated on figure 22(left). While for accurate bundle adjustment in MICMAC, optimal configuration is to have GCPs in each corner and centre of the image block (figure 22(right)).

By following position guideline of figure 22, surveyed points were selected in an overlap zone of 3 successive images. For accuracy of point localization in the images, points were selected as corners of pedestrian marks across the road or on corners of parking marks or any other accessible of such marks highly identifiable and localisable on both aerial and Pleaides images. As, it was hard to find such stable points in farmlands and semi-natural areas, the Southern and North-Western parts of area of interest lack surveyed points as shown on figure 23. Due to high

difference in visible details between the two datasets, centre points of some roundabouts were added to ensure sufficient surveyed ground points able to be seen on both datasets.

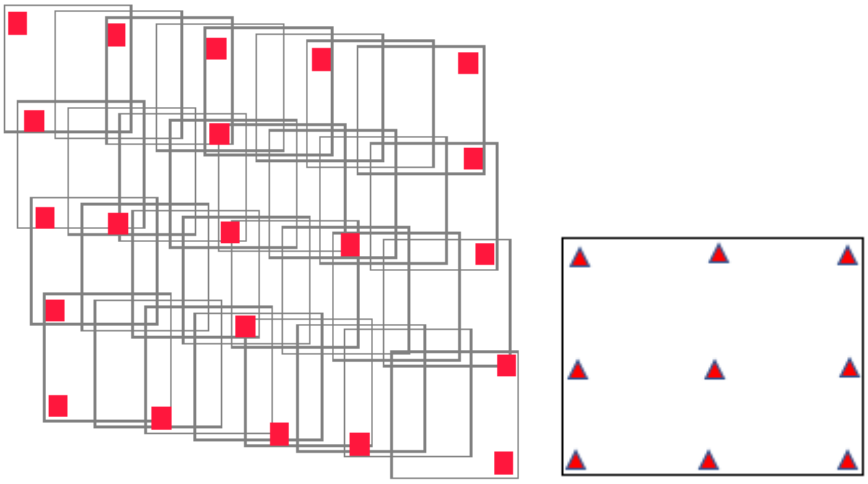

Figure 22: Recommended spatial distribution of GCPs (Hexagon Geospatial, 2017) (left). Optimal spatial distribution of GCPs in a block of images according to E. Rupnik (pers.comm.,2017) (right).

Field work

The GNSS field survey was performed on Saturday 29, Sunday 30 of April and Monday 1st of May 2017. During this survey, planimetric coordinates in Lambert 72 coordinate system of identified ground control points in reconnaissance study helped to track their correct positions. The zoomed view at each point location and its coordinates made field survey easier. Points that didn't found due to recent urban management or points that were near power lines or electric poles or not compatible with GNSS measurements (multipath features, signal hidden features…) were replaced after checking their visibility both on aerial and Pleiades images. As it was impossible to directly survey centre points of roundabouts due to statues monuments, 4 equally distant points were taken around and the corresponding centre point was post estimated using circle equation, see calculations in annex C. These chosen 4 distant points ideally formed a square and calculations were done with least square adjustment.

At the end of reconnaissance and GNSS field survey, terrestrial coordinates of 49 surveyed ground points were accurately surveyed (figure 23) in Belgium map coordinate system (Lambert 1972). This set of points was split into two categories; GCPs as points suitable to photogrammetric processing according to recommendations of figure 22 (right) and Check Points (CPs) as remained points and used to evaluate the accuracy of results (details on distribution of GCPs and CPs used for Vexcel and Pleiades is seen in figure 35 and figure 36).

However, due to the lack of surveyed ground points in North, South and corners of study area (as seen on figure 23 and figure 24), we were unable to establish strong GCPs configuration specified on figure 22 (right). A detailed description of these surveyed 49 points and additional computations are provided in annex C.

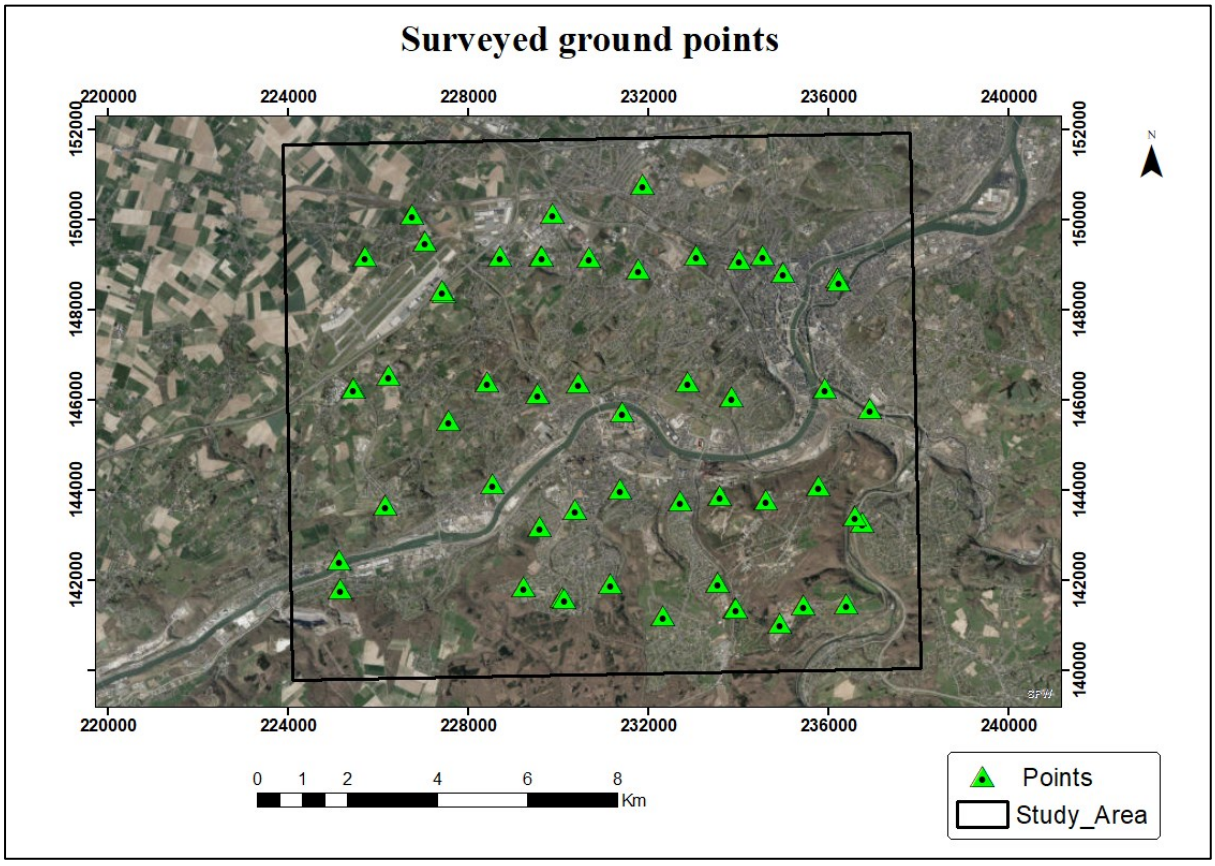

Figure 23: Spatial distribution of all surveyed points (GCPs and CPs). The background true colour composite is the orthoimage of Wallonia of 2015 accessible on the Walloon Geoportal (http://geoportail.wallonie.be/walonmap)

IV.2. MICMAC workflow

Below there are details on aerial and Pleiades images processing for DSM production. The details on used command lines for aerial and Pleiades photogrammetric processing are respectively in annexes D and E. At the end of each processing section, a chart flow summary of a set of used tools is given (figure 29 and figure 33). Processing was done on Ubuntu 16.04 LTS, RAM of 15.6GB, Processor of Intel Core i7-3930KCPU @ 3.20GHZ x 12, 64bits of operating system, 2.9TB of disk and Gallium0.4 on NVA8 graphic card.

IV.2.1. Aerial image processing

Inputs

112 aerial Vexcel images covered large extent compared to the zone of study, so, only 48 images whose cameras centres close to Pleiades boundary (figure 24) were processed to meet the aim of this research.

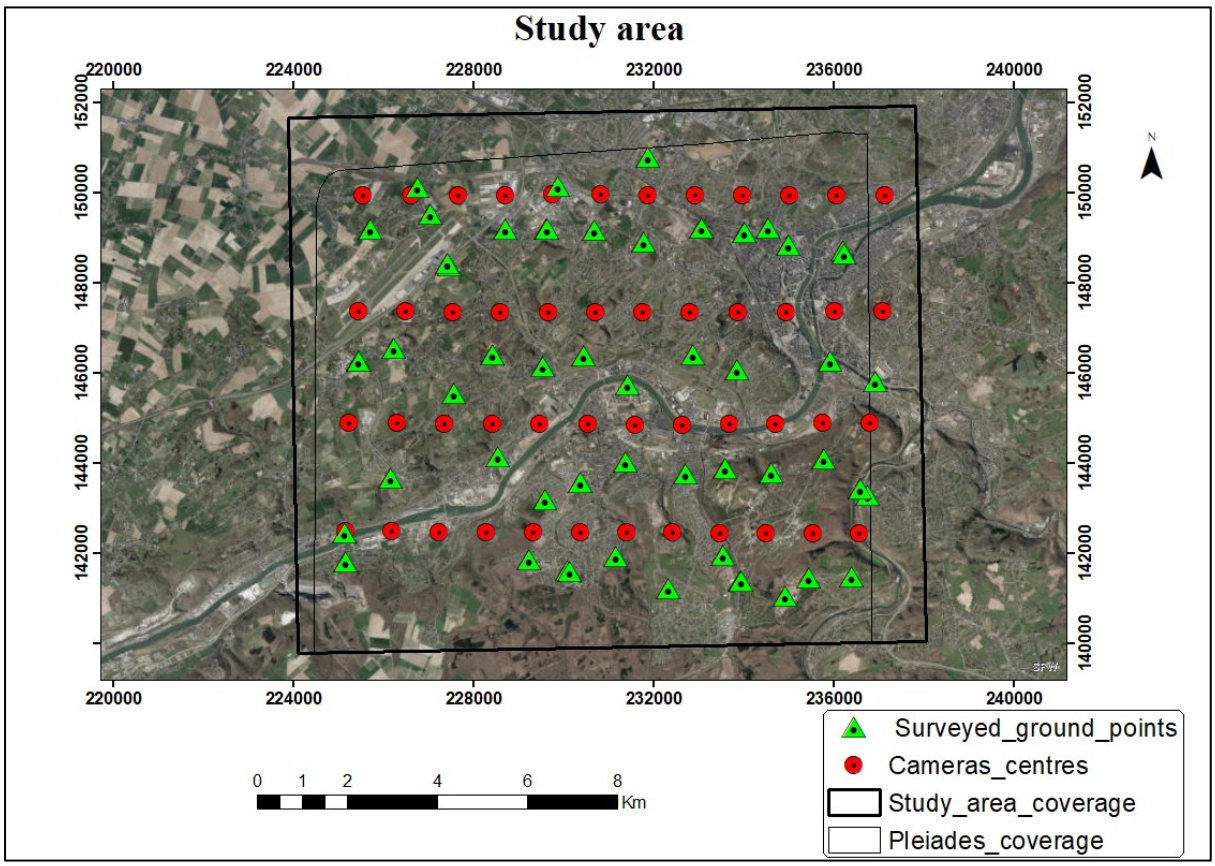

Figure 24: Study area, position of the aerial images and footprint of stereo pair of Pleiades image subsets ordered from Astrium (described in next section). The background true color composite is the orthoimage of the Walloon Region produced in 2015 (http://geoportail.wallonie.be/walonmap).

Being raw images, they missed metadata information (also called Xif) defining the internal parameters like focal length and sensor size. This information was obtained from calibration certificate and were associated to images through specific association keys in an xml file named MicMac-LocalChantierDescripteur.xml, containing specific characteristic of this project. An ASCII file containing 3D coordinates and precision of surveyed ground points (GCPs and CPs) was converted into software's compatible xml file format (named "gcp-S3D.xml" see annex D) by GCPConvert tool.

The uncertainty of GNSS measurements were taken into account during bundle adjustment by reducing their weights by a certain factor as it is explained in further sections.

Tie points generation

In MICMAC, image matching i.e. detection and correspondence of homologous points (tie points) is done prior to image orientation (inner or exterior). In other words, tie points define the quality of exterior image orientation and the latter determines DSM quality. According to Remondino *et al.* (in preparation, 2013), image matching is the establishment of correspondences between the extracted primitives from two or more images. Image matching can be established through area based approach or feature based approach. MICMAC uses feature based approach by SIFT algorithm precisely SIFT++ which is the C++ version of SIFT. SIFT generates Key points (also called feature points) on each image which become Tie points only when they are matched to homologous points on one or several other image(s). Further explanations on SIFT algorithm is found in Lowe (2004). The use of SIFT in MICMAC is detailed in Galland *et al*. (2016).

Due to the fact that the algorithm implemented in MICMAC is based on the original SIFT which was basically developed on greyscale images, the Key point detection process with multispectral images is done on the corresponding greyscale images. The conversion from multispectral to greyscale is performed as the mean value of the first three spectral bands (R, G, B) during tie point detection process. From the test we did, this generates less tie points than those found on the highest contrasted band (R band) which explains the fact that the implemented SIFT++ is not fully invariant in terms of contrast as stated by Pierrot-Deseilligny (2017). Despite that we chose to adopt the default conversion method of Micmac for tie points generation on multispectral images.

SIFT after storing in a database all possible detected feature points, it globally matches each feature point of each image to other images individually to the database by evaluating object, position, scale and orientation. Then, the obtained matched candidate points formed clusters, however only clusters that contain at least 3 candidate key points are kept. Due to ambiguous features or presence of clutter in image, this matching is not accurate thus, further evaluation is done by examining in key point database the nearest neighbour of each matching candidate in each cluster. The best match is found to be that of minimum euclidean distance for the invariant descriptor vector (Lowe, 2004; Aguilera *et al.*, 2012).

Tapioca, a simplest tool of *PASTIS* an interface to SIFT was used to extract tie points from images. The computational mode parameters of Tapioca (All, MulScale, Line, File, Graph, GeoRef) control how SIFT 's key points from image pairs have to be matched to become tie points and help to maximize the matching among pairs of descriptors identified (Pierrot-Deseilligny, 2017).

Therefore, to accelerate tie points detection process on pairs of aerial images, resampling was done with computation mode Multiple Scale Approach "MulScale", firstly, at finer resolution of 1000 from which only pairs with at least 2 matched points were secondly involved in computation of tie points at resolution of 5000 because with the used computer capacity it was impossible to run computation at whole resolution images due to their large volumes (48 images each of 820 GB).

By detecting tie points at final image resolution of 5000, the precision was deteriorated by more than 2 pixels as the size of each image was 17 310 columns and 11 310 rows, this has negatively affected the quality of resultant photogrammetric products as it has found in chapter five. Even if thousands of tie points were found on image pairs (figure 25), it was impossible to zoom in this ELISE (Elements of an Image Software Environment) window to evaluation the correctness of obtained tie points. As seen on figure 25, in homogenous areas (Meuse river) and in forests, few tie points were detected.

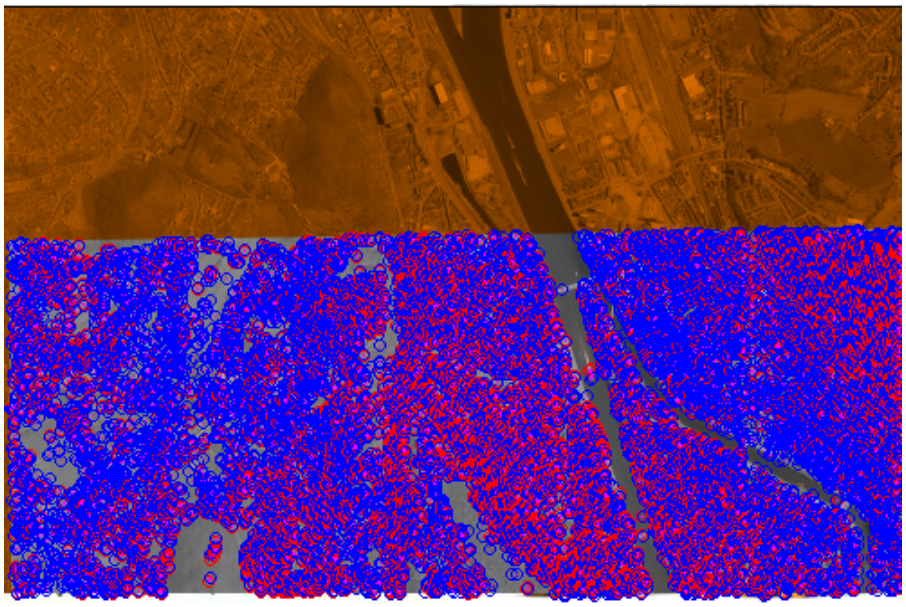

Figure 25: MICMAC snapshot of tie points on common zone of Vexcel stereo pair: on first image (1_10A_16278.tif) and on second image(1_10A_16279.tif)

Image relative orientation

APERO carries out image orientation and position together with distortion modelling from observations. The observations can be tie points, GCPs, rough position of projection centre and camera orientation from embedded GPS/IMU.

Having only tie points as observations from our aerial images, first orientation is required in order to fix an arbitrary coordinate system of the stereo-model. In that regard, the user chooses the starting image whose position has to be fixed otherwise *APERO* chooses that image as the one with highest amount of tie points from its optimal list of image pairs (M. Pierrot-Deseilligny, pers.comm., 2017). In our experiment, we used the second option. The second image for first orientation was then chosen automatically as the one having multiple tie points matching with the tie points of the first image.

After linearization of the equations, *APERO* performs least square adjustment and resolve the unknowns which are the parameters of the internal calibration, depending to the calibration model used, the camera orientations and positions. Then it uses a RanSaC (Random Sampling Consensus) algorithm and inertial matrix (computed using tie points), to orient in the arbitrary coordinate system all images of the block (Pierrot-Deseilligny and Clery, 2011). Due to the reason that MICMAC was designed for terrestrial and aerial photogrammetry, the base component along the x-axis (head of the aircraft) of the first image was not designed to be equal to one as it is for dependent relative orientation method but to stay random (M. Pierrot-Deseilligny, pers.comm., 2017).

From calibration certificate, an xml file of calibration of images were prepared by not taking into consideration the presence of distortions as they were less than 2 microns. Having digital images taken by digital cameras, internal parameters were already in pixel units so internal orientation was not done. From detected tie points and parameters of internal orientation, relative orientation of block of images was calculated by Tapas an interface to *APERO* with calibration model Figee. Sparse cloud points and cameras positions were then computed in arbitrary system by AperiCloud and visualized by CloudCompare as in figure 26:

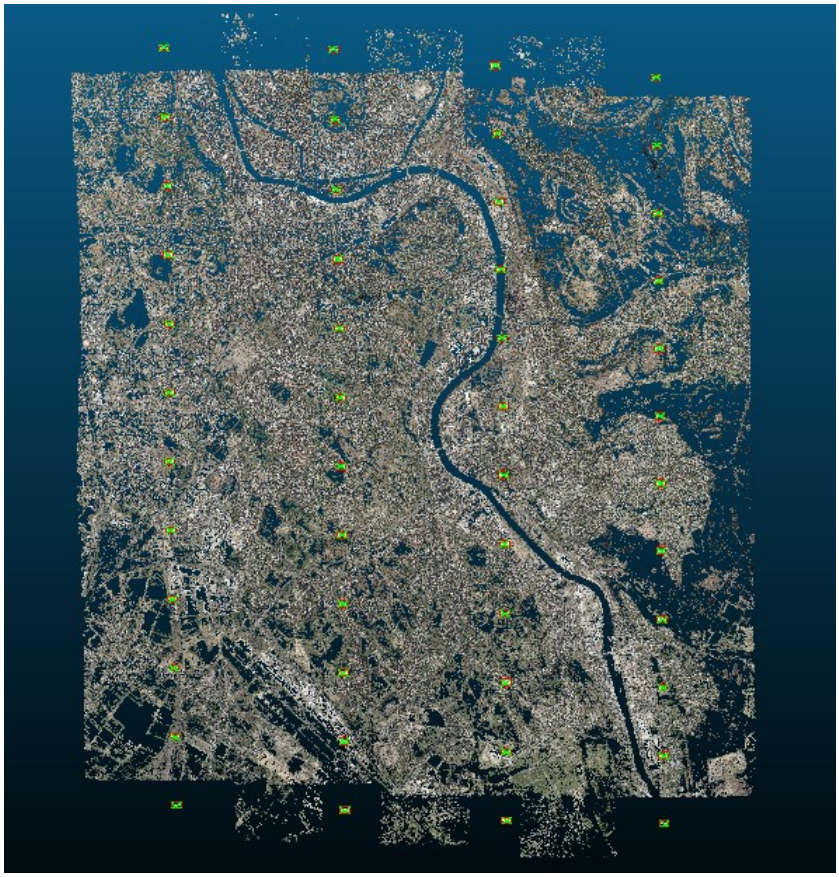

Figure 26: CloudCompare's screenshot of top view of relative orientation of all images (Camera positions are in green and red colours and on background, there are sparse cloud points)

Absolute orientation

External orientation is done thanks to known GCPs or position of projection centre from GPS/IMU or their combination. There are two types of equations for determining 3D intersections of homologous rays; either coplanarity equations or collinearity equations. MICMAC uses collinearity equations (M. Pierrot-Deseilligny, pers.comm., 2017). To estimate absolute orientation's parameters, MICMAC implements bundle intersection through spatial resection method explained in Kraus and Waldhäusl (1998) in order to estimate six parameters of exterior orientation from at least three non-collinear GCPs.

As external orientation requires to know 2D coordinates of GCPs in image space, MICMAC provides ELISE windows where GCPs are positioned on images manually either by SaisieAppuisInit or SaisieAppuisPredic tool while image measurements are being saved automatically in a specified new folder (called "gcp-2D-S2D.xml" in annex D) in working directory. During processing, MICMAC found 3D coordinates into gcp-S3D.xml file in which

points with positive incertitude are identified as GCPs and those with negative incertitude as CPs.

From image coordinates of 4 GCPs measured on 6 images with SasisieAppuisInit, the absolute orientation parameters corresponding to the relatively oriented images were estimated by GCPBascule tool. From this approximated ground model, the positions of remained GCPs and CPs were predicted and measured with SaisieAppuisPredic which facilitated the procedure. Ground model orientation of the whole block was then calculated using again GCPBascule to estimate seven parameters of the final absolute orientation. So, the obtained parameters were the following:

i) Scale: 398.48

ii)Three translations of the origin: Xo=230531.74 m, Yo=144867.50 m, Zo=4080.52 m

iii) Rotation matrix:

$$\begin{bmatrix} -0.0150138745842059666 & 0.999878473964179615 & 0.00419772236254948878 \\ -0.99988515483243734 & -0.0150050436004253336 & -0.00212739565245834844 \\ -0.00206415011142554831 & -0.00422918072593837444 & 0.999988926596042327 \end{bmatrix}$$

From the above matrix three angles can be retrieved using the below formula:

$$\begin{bmatrix} \cos(\Phi) * \cos(\mathrm{K}) & \cos(\Phi) * \sin(\mathrm{K}) & -\sin(\Phi) \\ \cos(\Omega) * \sin(\mathrm{K}) + \sin(\Omega) * \sin(\Phi) * \cos(\mathrm{K}) & -\cos(\Omega) * \cos(\mathrm{K}) + \sin(\Omega) * \sin(\Phi) * \sin(\mathrm{K}) & \sin(\Omega) * \cos(\Phi) \\ \sin(\Omega) * \sin(\mathrm{K}) - \cos(\Omega) * \sin(\Phi) * \cos(\mathrm{K}) & -\sin(\Omega) * \cos(\mathrm{K}) - \cos(\Omega) * \sin(\Phi) * \sin(\mathrm{K}) & -\cos(\Omega) * \cos(\Phi) \end{bmatrix}$$

Absolute orientation with GCPBascule being computed with the assumption that relative orientation is perfectly known, bias in exterior orientation are corrected using bundle adjustment in which GCPs and tie points are combined together with their weighting functions through Campari tool. As specified previously, tie points are not accurate due to restricted final resolution of images, so, their weight was reduced by multiplying their precision by 10 as the same as GCPs' weight so that precision of each GCPs should be reduced from millimetre up to centimetre level.

During this process, Campari filters tie points obtained from Tapioca by removing those which are not stable and bad matched. According to Triggs *et al.* (2010) this adjustment consists of refining visual reconstruction to get optimal 3D structures and estimates of viewing parameters such as camera centres, calibration and 3D coordinates of features. The block was georeferenced at the average residual of 0.66 pixels.

Quality evaluation of orientation

The orientation was verified through matching in perpendicular direction to epipolar curve by MMTestOrient tool in order to validate the internal accuracy. This was done on Campari's orientation results. The resulting parallaxes; Px1 the epipolar parallax which is the depth and Px2 the transverse parallax which is the displacement in the orthogonal direction to the epipolar (Pierrot-Deseilligny, 2017) were then generated. Px2 is supposed to be null for perfect orientation, however addition factors such as noisy or ambiguity in 2D matching can also be the source of having values different to zero, so spatial and quantitative analysis was done to understand the source of errors.

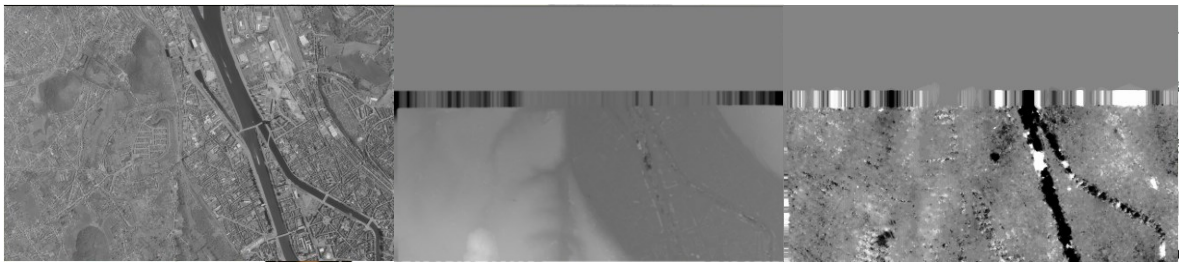

Figure 27:MICMAC's snapshots: (left) aerial image (1_10A_16278.tif), (middle) the epipolar parallax (Px1_Num16_DeZoom2_Geom-Im_8Bits.tif), (right) the transverse parallax (Px2_Num16 DeZoom2_Geom-Im.tif. (Dynamic of transverse parallax was set based on the average and standard deviation of pixel values).

Figure 27 (right) and (middle) show epipolar and transverse parallax of first stereopair of aerial images (1_10A_16278.tif and 1_10A_16279.tif) of the same strip that's why only common zone has information. Black patterns are mainly in Meuse river due to low correlation. In order to understand statistical significance of transverse parallax of figure 27 (right), StatIm tool was computed over the bounding box of 8650 and 5580 pixels. The obtained mean value was 0.001 pixels and standard deviation was 0.16 pixels. As mean value approach zero, there is no significant bias in orientation and also no significant systematic errors left for correction. The standard deviation being less than 1/5 pixel shows that the biases throughout the image are near the mean value. Thus, orientation results were relevant for DSM computation.

Orientation export

Campari generates an exterior orientation xml file for each image. This orientation was exported using OriExport tool in a standard form in which Omega (Ω), Phi (Φ), Kappa (K), the three angular measurements were in degrees and camera centres' position during exposure of each image were in Lambert 1972. See Annex F.

Dense matching and 3D products creation

There are two different geometry for dense matching, either image geometry or ground geometry. According to (E. Rupnik, pers.comm., 2017) in image geometry, a depth map per image pair is produced. It required to input an image master from which all 3D points are re-projected into secondary images. In ground geometry, a dense point cloud of the whole image block is generated. At each pixel of image block a height Z is calculated.

MICMAC has three tools for dense matching: Malt, C3CD and PIMs. According to (M. Pierrot-Deseilligny, pers.comm., 2017) Malt is fast and commonly used in aerial photogrammetry workflow where the ground altitude is concerned while PIMs is robust and used in terrestrial photogrammetry where depth is more important. C3CD is like a component of PIMs called PIMs2Ply which produces dense point cloud.

From adjustment results, a dense matching was calculated in order to produce the corresponding DSM in ground geometry. To do so, Malt tool was used with UrbanMNE mode. Computation was performed in window size of 3x3. As Malt by default computes a DSM for at least a tristereo images, we specified the option NbVI=2 to indicate that we are dealing with stereo pairs. To be able to get absolute height values, the option EZA=1 was used. In Micmac, terrain resolution of input images is kept on the resultant 3D products. To be time saving, the option DoOrtho=1 was added to command line of Malt so that after DSM computation, orthoimages of each and every pair of images should be calculated.

To facilitate comparison analysis between Pleiades and Vexcel photogrammetry products, two DSMs and two orthomosaïc were produced from a block of Vexcel aerial images; firstly, DSM and individual orthophotos were produced at 25 cm of resolution. Secondly, DSM and orthophotos were produced at spatial resolution of 50 cm whose coverage was defined and calculated based on metadata of Pleiades' DSM as a bounding box of [224123, 139218.5, 236716, 151264] respectively as minimum X, Y and maximum X, Y. The 25 cm and 50 cm individual orthophotos were then separately ortho-mosaicked by Tawny tool. Tawny merge individual orthoimages and carry out radiometric equalization (Pierrot-Deseilligny, 2017). In using Tawny tool, no addition parameter was indicated; we kept default options where radiometric equalizer is done by first degree polynomial function. The resultant orthomosaïc was a colour image of 3 visible bands. For data volume handling, Micmac generated 25 cm Vexcel orthomosaïc and DSM in 8 tile image files and 50 cm orthomosaïc and DSM in 4 tile

files so that they can be visualized and analyzed in Geographic Information System (GIS) software.

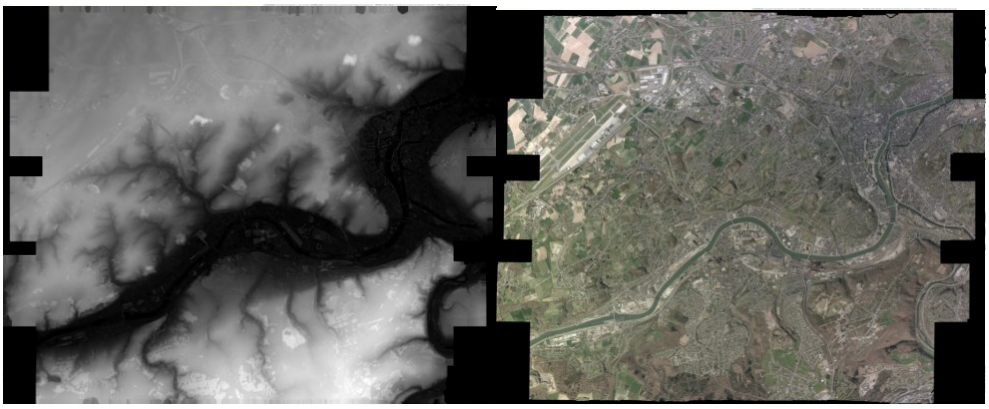

Figure 28: DSM and orthoimage from Vexcel images (snapshot of MICAMC)

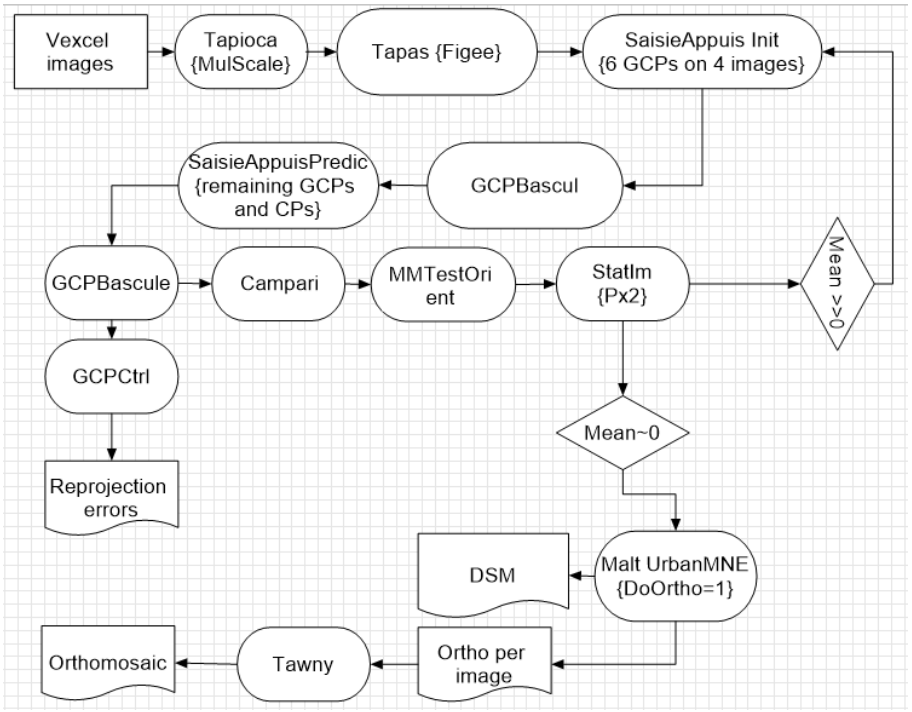

Figure 29: Summary of all used tools

IV.2.2. Satellite image processing

Inputs

The main inputs given by image provider were a panchromatic stereo pair of 16 bits and their corresponding RPCs (each per image) coded in DIMAP version 2.15. The same gcp-S3D.xml file used in Vexcel aerial processing containing 3D measurements of GCPs and CPs was again used for RPC refinement purpose, but signs of incertitude were changed to ensure the use of correct GCPs and CPs for Pleiades processing (figure 36 shows the used GCPs and CPs) as those points were not totally the same for Vexcel and Pleiades processing.

Tie point computation

In addition to GCPs, tie points are necessary as well. According to Stumpf (2013), tie points correct relative bias while GCPs scale and correct absolute biases. Tie points were calculated from stereo pair by MulScale at first low resolution of 1000 and finally at whole image resolution without shrinkage (resolution of -1).

RPC processing and refinement

RPCs contained coefficients of third order rational polynomial functions that express the collinearity and perform the conversion of geodetic coordinate expressed in WGS84 datum into sample and line image coordinates and inversely through the following mathematical expressions:

$$sample(\phi, \lambda, h) = \frac{P1(\phi,\lambda,h)}{P2(\phi,\lambda,h)} \quad (7)$$

$$line(\phi, \lambda, h) = \frac{P3(\phi,\lambda,h)}{P4(\phi,\lambda,h)} \quad (8)$$

$$P_i(\phi, \lambda, h) = \sum_{i=0}^{m} \sum_{j=0}^{n} \sum_{k=0}^{o} C_{ijk}\, \phi^i \lambda^j h^k \quad (9)$$

$$\lambda(sample, line, h) = \frac{P\prime1(sample,line,h)}{P\prime2(sample,line,h)} \quad (10)$$

$$\phi = (sample, line, h) = \frac{P\prime3(sample,line,h)}{P\prime4(sample,line,h)} \quad (11)$$

$$P'_i(sample, line, h) = \sum_{i=0}^{m} \sum_{j=0}^{n} \sum_{k=0}^{o} C'_{ijk}\, sample^i line^j h^k \quad (12)$$

Where k is the image and (ϕ, λ, h) the object's WGS84 geodetic coordinates expressed in degree and meter. P_i and P'_i (i = 1 to 4) are nominator and denominator of the third order

rational polynomial functions. C_{ijk} and C'_{ijk} are the 80 provided RPC. The values of m and n comprises into [0-3] because of the third order of the functions.

MICMAC doesn't understand geocentric coordinate system but euclidian coordinate system. Therefore, RPCs were converted and projected in appropriate Belgium coordinate system Lambert 1972 by the tool Convert2GenBundle.

RPCs' error

To understand how inaccurate RPC was and to demonstrate the importance of their refinement by the introduction of GCPs, Campari was done by only tie points as observations where all GCPs were turned into CPs (by adding negative sign to their precisions). Campari's results showed ground distance error of the range of 58 up to 67 m between predicted position and real positions of CPs. This orientation error was in the same direction on both stereopair independently to CPs' location. This is illustrated on figure 30 where roundabouts centre points (0 and 130 000) were projected off their correct positions.

Figure 30: Imperfections of RPC (point 0 on left and 130 000 on right). (Micmac's snapshots)

RPCs' refinement

Very high-resolution satellite images processing with MICMAC assumes as hypothesis that there is no error in sensor trajectory but that there is inaccurate calibration and attitude of sensor. Thus, 2D polynomial functions of image space in x and y are used to model the refinement of RPC by combining tie points measurements with GCPs in bundle adjustment (Campari tool) to ensure perfect relative orientation and intersection of homologous rays at a single 3D point. Furthermore, as stated in Rupnik *et al.* (2016), to resolve sensor orientation's imperfections of RPC data, a polynomial compensation of line (or row) and sample (or column) coordinates is used based on constraints and conditions. Regarding conditions (observations),

a deforming polynomial function is used so that for every homologous point, its image coordinates are corrected and adjusted as follow:

$$sample'(\phi, \lambda, h) + D_{sample}(x, y) \qquad (13)$$

$$line(\phi, \lambda, h) + D_{line}(x, y) \qquad (14)$$

$$D_{sample}(x, y) = \sum_{i=0}^{m} \sum_{j=0}^{n} a_{ij} * x^i y^j \qquad (15)$$

$$D_{line}(x, y) = \sum_{i=0}^{m} \sum_{j=0}^{n} b_{ij} * x^i y^j \qquad (16)$$

Where $D_{sample}(x, y)$ and $D_{line}(x, y)$ are adjustable functions added to the rational function in order to compensate the discrepancies between measured image coordinates and nominal line and sample coordinates of GCPs and /or tie points for an image. a_{ij} and b_{ij} are polynomial coefficients that should be estimated for each image, they include coefficients like $\mathbf{a_0}, \mathbf{a_S}, \mathbf{a_L}, \ldots$ and $\mathbf{b_0}, \mathbf{b_S}, \mathbf{b_L}, \ldots$ as detailed in (Grodecki and Dial, 2003).

$\boldsymbol{a_0}$ is a parameter that absorbs in-track errors which induce offsets in line direction such as in track ephemeris, satellite pitch altitude errors, line component of principal point and detection position errors while $\boldsymbol{b_0}$ absorbs across-track errors causing offsets in sample direction like cross track ephemeris errors, satellite roll attitude error, sample component of principal point and detector position errors. Parameters in line direction ($\mathbf{a_L}, \mathbf{b_L}$) absorb gyro drift effects and those in sample direction ($\mathbf{a_S}, \mathbf{b_S}$) absorb radial ephemeris error and interior orientation errors like errors in focal length and in radial distortion (Grodecki and Dial, 2003). In 0-degree polynomial, only two parameters, $\boldsymbol{a_0}$ and $\boldsymbol{b_0}$, are estimated while in first order polynomial additional parameters are estimated.

According to Rupnik *et al.* (2016) 0-degree polynomial is sufficient to adjust image bundles taken from the same orbit while first-degree polynomial is for images acquired from different orbits as those images require high positioning accuracy therefore, necessitate additional parameters in bundle adjustment. In this study, stereo pair was acquired from the same orbit so, during RPC conversion parameter Degree=0 was specified in command line of Convert2GenBundle tool.

To model image deformation due to changes (first constraint) in sensor attitude $\delta\alpha_i$ which induce image pixels' displacement R_i, this formula is used (Rupnik *et al.,* 2016):

$$\sum_{x=0}^{m}\sum_{y=0}^{n}(\sum_{k}^{\{x,y\}} D_k(x,y) - \sum_{l=0}^{2}\delta\alpha_l R_{x,y,l})^2 * pds_{rot} * pds_{NB} = 0 \qquad (17)$$

Second constraint located in the following formula ensures that displacement remain nearly zero:

$$\sum_{x=0}^{m}\sum_{y=0}^{n}\sum_{k}^{\{x,y\}} D_k(x,y)^2 * pds_{nul} * pds_{NB} = 0 \qquad (18)$$

k is the image, l is the line. pds_{rot} (the weight parameter of rotation constrains), pds_{nul} (parameter which forces that deformation field is small) are non-parameterized weight functions and pds_{NB} the weight function of each observation (Rupnik *et al.,*2016).

Before applying the corrections in equation (15), (16), (17) and (18), 2D image measurements of GCPs were obtained using SaisieAppuisPredic tool in ELISE window. These measurements were done on 8bits images converted from the original 16 bits pair because the latter had contrast problems. The conversion was done by To8Bits tool with contrast enhancement parameter Dyn=0.1. Except this procedure, the whole processing was done on 16 bits original images so that matching accuracy should not be altered.

Only 12 GCPs were used to compensate RPCs'errors. RPCs' refinement was practically performed by Campari tool in which weighting functions were involved on GCPs measurements such like; precision of 3D measurements of each GCPs was multiplied by 10 so that their weight would be reduced during refinement. On the other side, weight of their 2D measurements was not altered by setting their multiplication factor at 1. Campari involves tie points to ensure corrections in image orientation (precisely in relative orientation) if any. Parameters of equations (17) and (18) were involved in Campari tool, however, we chose to keep their default values ($pds_{rot} = 0.002$ and $pds_{nul} = 0.0$).

This refinement was done at an average residual of 0.294 pixels and was qualitatively and quantitatively verified using MMTestOrient and StatIm tools. For MMTestOrient tool, mandatory parameters for pushbroom sensors were set as ZMoy=200 as mean altitude of the study area and Zinc=400 as incertitude on Z. The optional argument GB=1 was used to specify that it was a generic bundle mode.

Figure 31 (right) shows that transverse parallax is almost null. Its quantitative value was assessed by StatIm tool over the bounding box of 11500 and 11500 pixels. The obtained mean value was 0.14 pixels and standard deviation was 0.12 pixels. The bias is homogeneous as

standard deviation is small. With such small bias, we assumed that no systematic errors remained in the refined RPC and that computation of 3D model can be done.

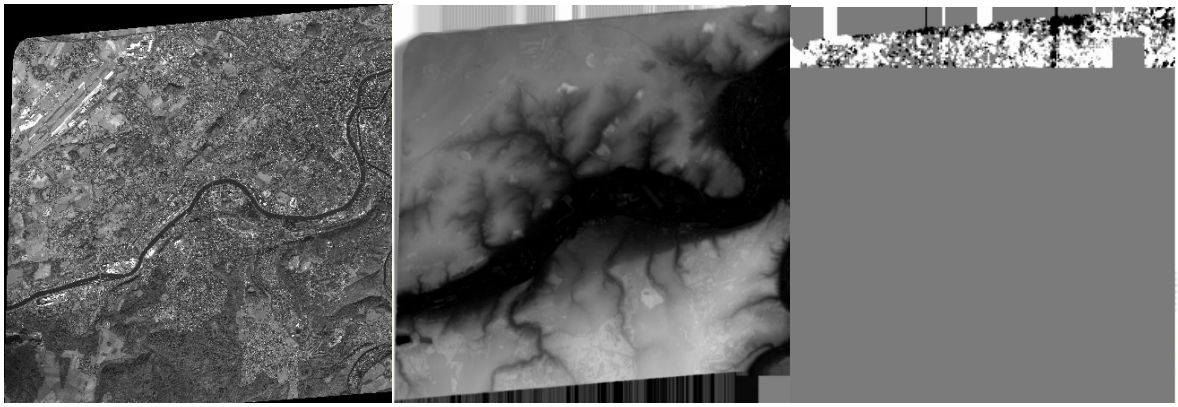

Figure 31:MICMAC's snapshots: (left) satellite image in 8bit, (middle) the epipolar parallax (Px1_Num16_DeZoom2_Geom-Im_8Bits.tif), (right) the transverse parallax (Px2 Num16 DeZoom2 Geom-Im.tif). (Dynamic of transverse parallax was set based on the average and standard deviation of pixel values)

Dense matching and 3D products creations

In order to generate a DSM and orthoimages, Malt tool was used. The absolute Z values were calculated by setting EZA=1 and DoOrtho = 1 to compute orthoimages of each image. DSM and individual orthoimages were produced at 50 cm of spatial resolution. The orthomosaïc was carried out by Tawny tool which performed also radiometric equalization. The orthomosaïc and DSM were each generated into 4 tile files in greyscale colour as processed images were panchromatic.

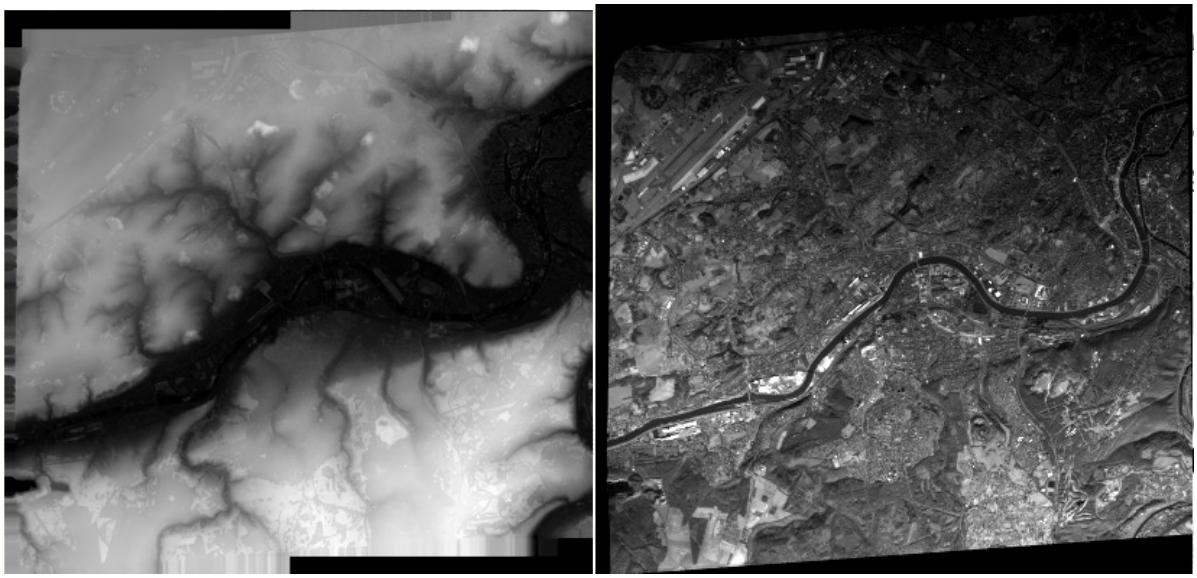

Figure 32: DSM and orthoimage from Pleiades (MICMAC's snapshots)

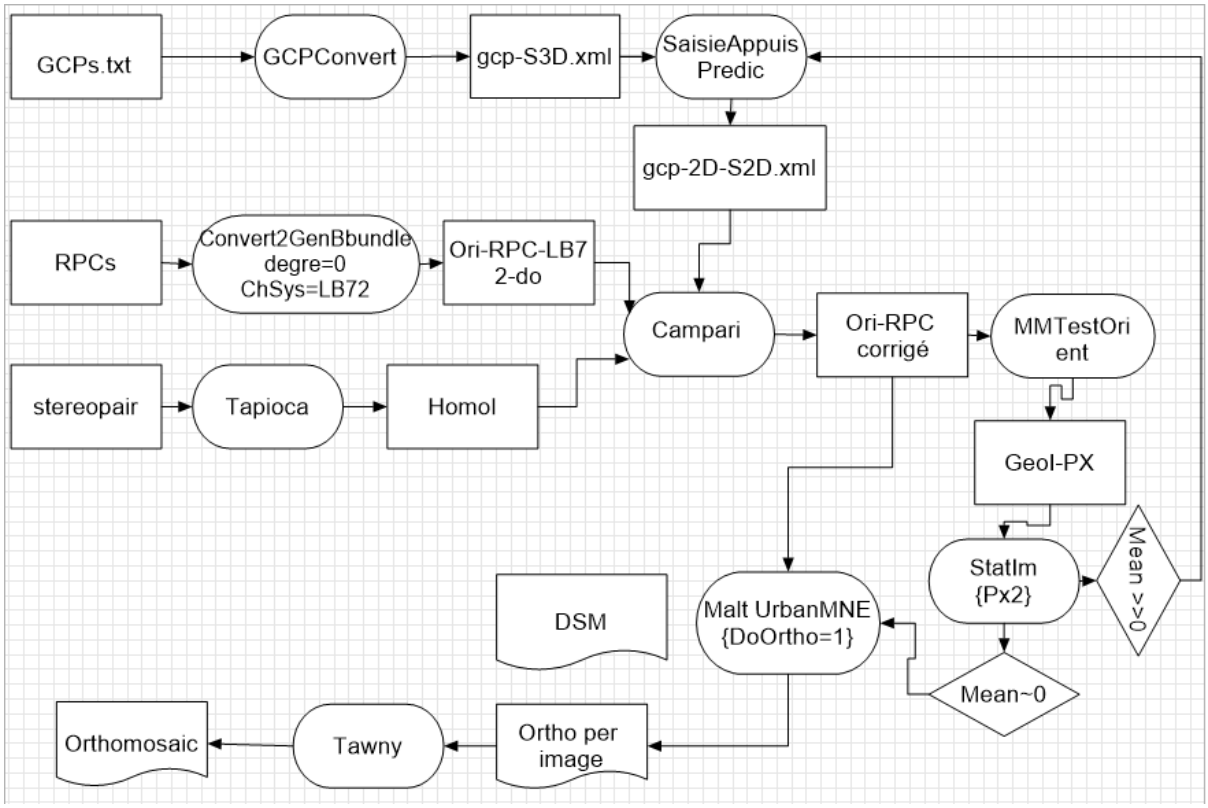

Figure 33: Summary of tools used in Pleiades processing

CHAPTER V. VALIDATION AND DISCUSSION

This chapter describes results of photogrammetric processes and their geometric and radiometric analysis. After evaluating software's 3D reconstruction uncertainty based on results from Pleaides and Vexcel aerial images, their qualitative and quantitative comparison were undertaken. Radiometric analysis was done on Vexcel orthomosaïc product by visual analysis. Altimetric validation of photogrammetric DSMs was done through their comparison with reference data such as data of *Projet Informatique de Cartographie Continue* (*PICC*) and Lidar measurements based on descriptive statistics, hillshadings and topographic profiles. From these analyses, discussions were made, research's hypothesis was verified and transposition of this research in Rwanda was also considered.

V.1. Uncertainty of MICMAC bundles adjustment

V.1.1. Uncertainty of Vexcel bundles adjustment

Georeferencing accuracy of MICMAC is estimated through CPs. The used 13 GCPs and 24 CPs are distributed as in figure 35. The estimated average of reprojection error of all CPs in all stereo images is 0.346 pixels. This error (figure 34), expressed in pixels, allows to evaluate the quality of 3D bundle reconstruction models, it is the error deduced from cost-functions of bundle adjustment expressed as the sum of distance squares between observed imaged points and projected primitives (Bartoli, 2003).

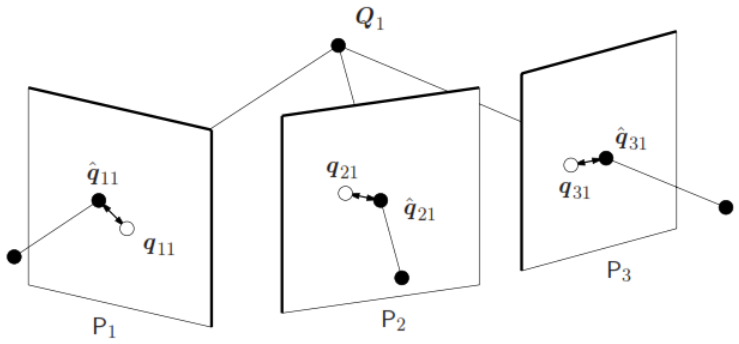

Figure 34 : Reprojection error of point Q1 in P_i (i=1 to 3) cameras (Bartoli, 2003). Where q_{ij} are measured image points and $\hat{q}_{ij}$ are estimated points.

In real world reference frame, bundle reconstruction uncertainty is represented by a planimetric root mean square error in X and Y and mean Z error. Respectively these errors are 0.247 m, 0.287 m and 0.200 m. Those values are at the range of spatial resolution of processed images (See annex H for the details on each CPs). Positive inaccuracy of Z coordinate shows that in

Vexcel products height is generally exaggerated. This overestimation is also confirmed by table 6.

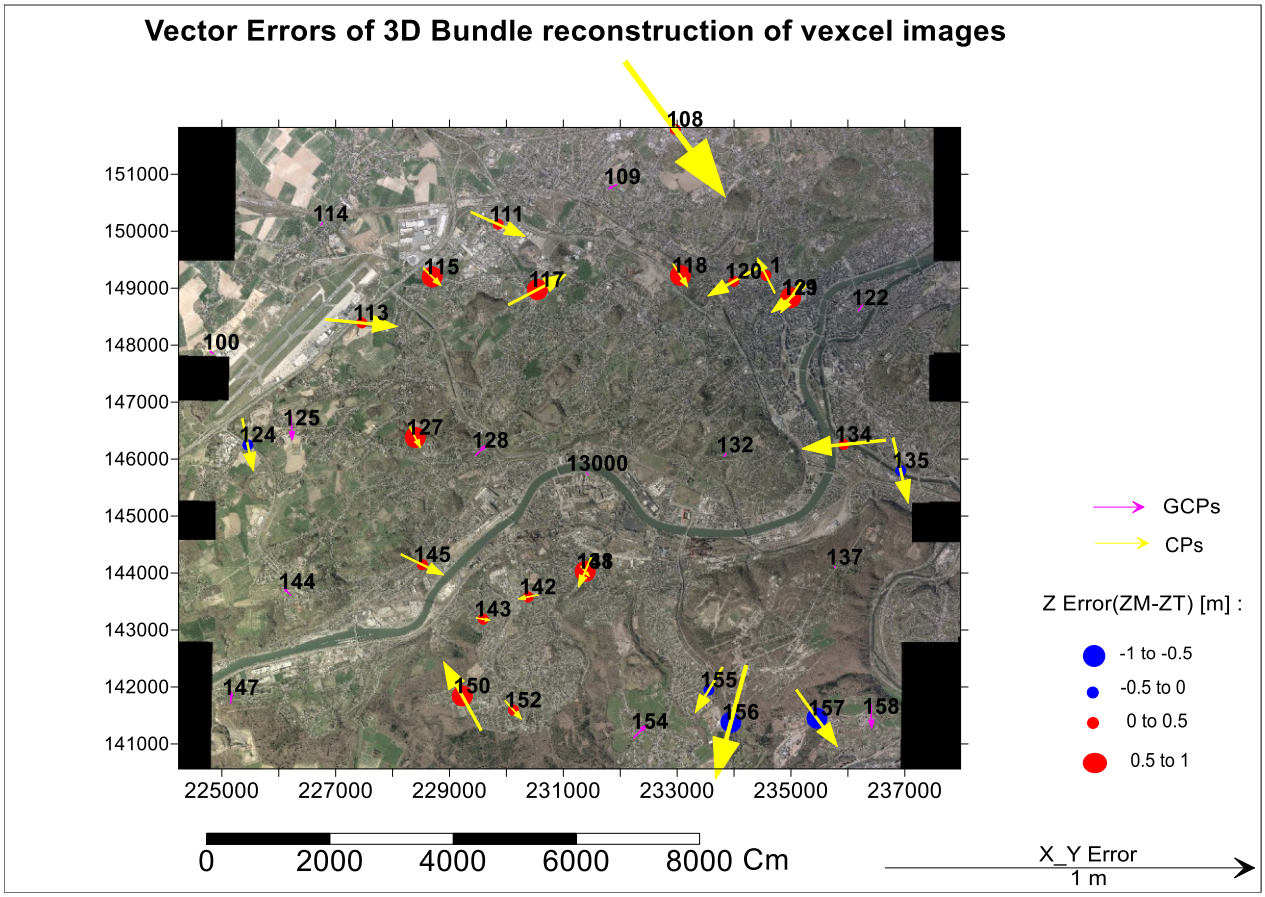

Figure 35: Planimetric and altimetric bundle errors of Vexcel aerial images. Z error is computed using the following subtraction: Z from photogrammetric measurement (ZM) minus Z from surveyed measurements (ZT)

As seen on figure 35, Z error is about ±1m. At South-East (3 points), East (1 point) and West (1 points), MICMAC's 3D photogrammetric model is underestimated. However, large parts are dominated by height overestimation which explains the positive Z inaccuracy of 3D bundle reconstruction of Vexcel images by MICMAC.

Planimetric error increased in Southern and Northern parts and CPs at borders of study area are the most erroneous mainly due to insufficient GCPs at those particular areas. In central part, this error is relatively small but it increases outwards. The orientation of this error is not systematic throughout the study area and also there is no correlation between planimetric and altimetric errors of bundle adjustment of Vexcel images.

Altimetric error of Vexcel is in the range of ±1m.

Table 6: elevation error of CPs of Vexcel; underestimation (in pink) and overestimation (in Blue).

Rank	ID	Z error (m)
1	157	-0.754
2	156	-0.593
3	124	-0.368
4	135	-0.367
5	155	-0.036
6	108	0.025
7	121	0.033
8	152	0.098
9	138	0.101
10	134	0.141
11	1	0.167
12	145	0.254
13	111	0.278
14	113	0.280
15	143	0.338
16	142	0.402
17	120	0.461
18	150	0.555
19	127	0.558
20	115	0.604
21	141	0.609
22	119	0.638
23	117	0.660
24	118	0.748

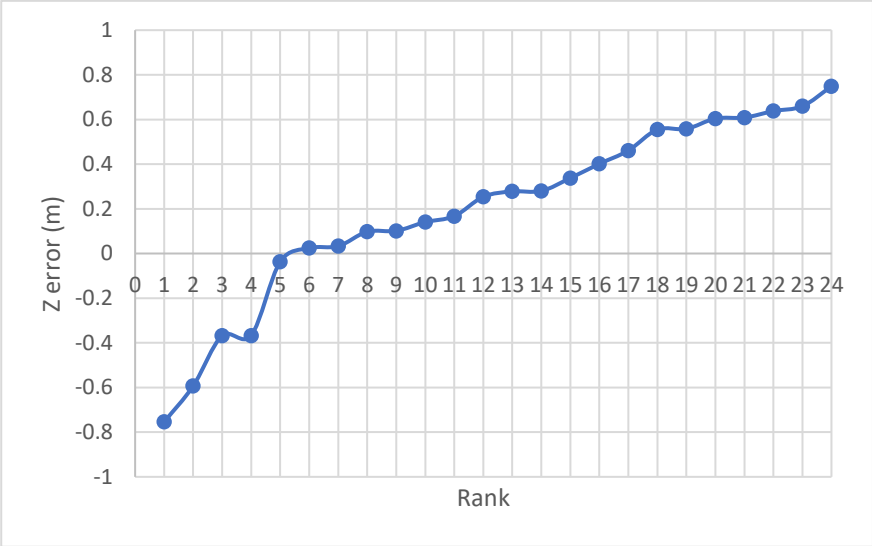

V.1.2. Uncertainty of Pleiades bundles adjustment

Pleiades bundles were adjusted based on 12 GCPs amongst which 4 corresponding to reconstructed centers of roundabouts number 12200, 12400, 13000 and 15700 and verified through 21 CPs as seen on figure 36. Average reprojection error of CPs was 0.309 pixel. CPs' X and Y root mean square errors are 0.402 m and 0.540 m respectively. CPs' Z inaccuracy is -0.117 m. This negative inaccuracy indicates that Pleiades tend to underestimate the altitude (also visible on table 7). On center points of roundabouts number 0, 11300 and 11600, Z error is large up to 5 m (on point 11300) and generally planimetric error of roundabouts is large too. This is due to the fact that center point was estimated based on four surveyed points on ground

level around the roundabout while some roundabouts' centre points were at certain altitude above mean altitude of surveyed points. Furthermore, accurate image measurements of those centre points were deteriorated by the presence of monuments or heightened vegetation on top area and by the limit in details based to Pleiades' spatial resolution of 50 cm. As consequences, the used GCPs have large planimetric uncertainty compared to Vexcel. Further details on reprojection, planimetric and altimetric errors of each CPs are in annex H.

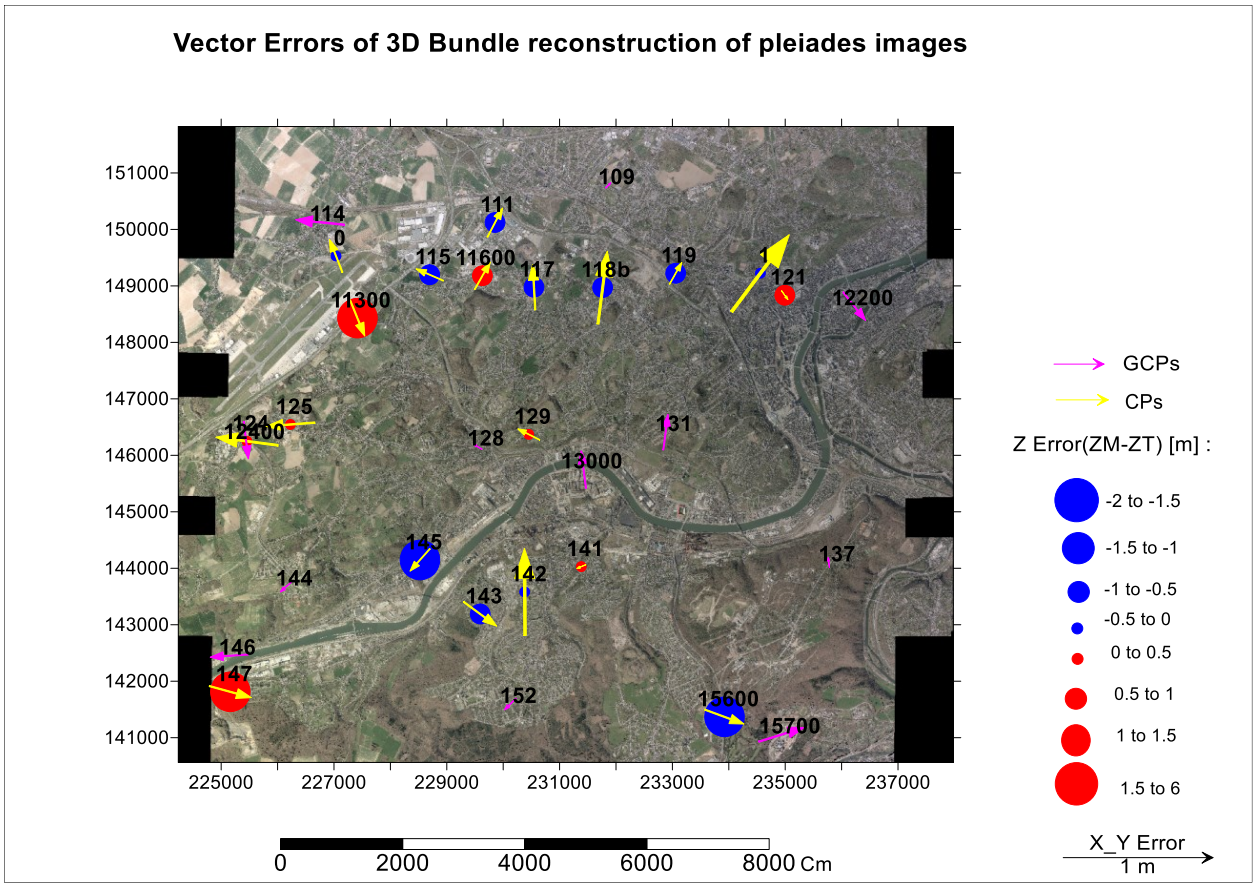

Figure 36: Planimetric and altimetric bundle errors of Pleiades stereopair

Pleiades' 3D bundle reconstruction has high planimetric error on North and East (figure 36). This error is not systematically oriented and not correlated to altimetric error. In North and West, there are diverging planimetric error vectors from centre area. Southern part has large altimetric errors while Northern part has medium errors.

Altimetrically, Pleaides is the least accurate with about -2 m and +6 m respectively as negative and positive extreme Z error values. Complete computations are found in annex H.

Table 7: elevation error of CPs of Vexcel: underestimation (in pink) and overestimation (in Blue)

Rank	ID	Z error (m)
1	15600	-1.622
2	145	-1.510
3	111	-0.920
4	117	-0.802
5	118b	-0.752
6	115	-0.605
7	119	-0.559
8	143	-0.511
9	142	-0.442
10	1	-0.418
11	0	-0.145
12	141	0.177
13	124	0.241
14	129	0.255
15	125	0.257
16	121	0.502
17	11600	0.774
18	147	1.691
19	11300	5.139

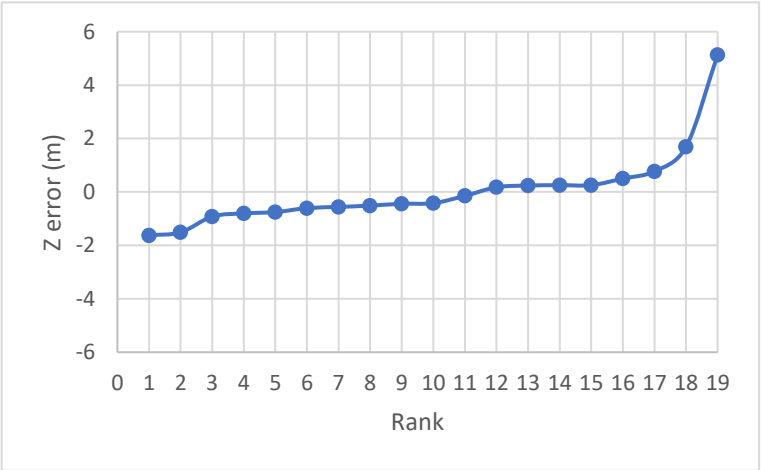

V.2. Quantitative and qualitative comparison of photogrammetric products

Using ArcGIS version 10.5, R and IDRISI software, photogrammetric products were post processed, compared and assessed.

V.2.1. Vexcel and Pleiades DSMs

In this analysis, Vexcel aerial DSM as well as Pleiades DSM produced at 50 cm spatial resolution were used.

Elevation difference image

DSM of Vexcel produced at 50 cm minus Pleiades' DSM shows high differences in a zone stretching in West-East direction of Southern part where there are relief variations and forest

cover. Slight inconsistency was found in the Central and Northern parts. Some of these differences are due to the remained shift effect in the adjusted Pleiades RPC related to used few GCPs in South and North which caused a North-East planimetric shift of Pleiades DSM with respect to Vexcel DSM. Three patterns can be distinguished as following:

i) Northern is dominated by general similarities of both digital surfaces except locally (see figure 37).

ii) Southern part (South-West, South-East) is highlighted by overestimated Pleiades altitude. This is actually the region dominated by forests and hills. This is also the area where less GCPs are available for dense matching of Vexcel and for correction of Pleiades RPC model.

iii) North-East has little differences especially along Meuse valley.

Minimum and maximum differences are -105.13 m and 58.20 m respectively. The mean difference is -0.19 m with standard deviation of 5.29 m. High standard deviation is due to presence of few large extreme values. As seen on the histogram (figure 37), error distribution is approximately normal but small asymmetry is hardly perceptible due to the excess of negative differences associated to the overestimation of Pleiades' height particularly in Southern part.

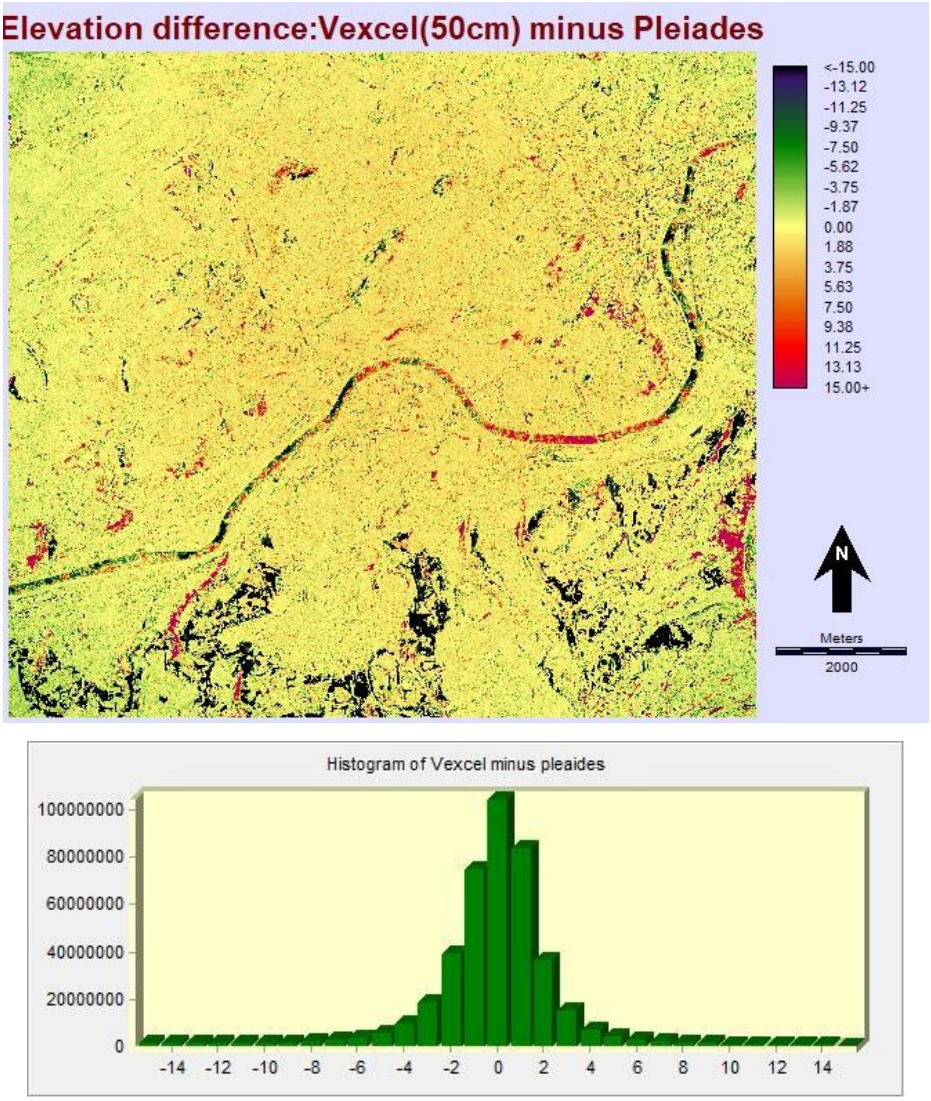

Figure 37: Vexcel DSM minus Pleiades DSM (top) and histogram of difference values within ±15m (bottom).

For pattern ii) Z difference between Vexcel and Pleiades is pronounced differently with respect to land cover types (figure 38 and figure 39) especially in deciduous forests, this was expected as Vexcel aerial images were acquired for agricultural and forestry applications in period (April) when vegetation cover is becoming dense and Pleiades images were acquired in early spring (March) for photogrammetric purposes when vegetation is absent. Furthermore, in grass land, bare soil, coniferous trees, and urban covers such as buildings and roads, small elevation difference (of a range of – and + 2 m) is detected with slight dominance of Vexcel (most of those areas are represented by colours in the middle of the colour palette with small variations towards red colour). Except in river area where differences from those DSMs is due to imperfections of image matching in homogeneous zones, zones covered by deciduous forests point out significant elevation differences depending to canopy cover differences based on

seasonal leaves-off phenomenon. For instance, Vexcel exceeds Pleiades in deciduous forest zones (red colour zone in figure 38) in which canopy leaves are denser on Vexcel than on Pleiades. On high rise buildings (like in figure 40) at Eastern façades Vexcel altitude is larger and at Western sides Pleaides is larger. Therefore, the presence of occlusions on Pleiades stereopair caused overestimation of Pleiades' altitude with respect to Vexcel's altitude and satellites' looking direction caused Pleaides' overestimation on the Western sides of buildings.

Figure 38: From left to right: DSM difference in meter, Vexcel orthomosaïc, Pleiades orthoimage

Figure 39: From left to right: DSM difference in meter, Vexcel orthomosaïc, Pleiades orthoimage

Difference in acquisition angles between Vexcel and Pleiades (Vexcel acquired nearly at nadir and incidence angle of Pleiades for first image was ~20° with satellite looking SW and for second image was ~15° with satellite looking NW) and small sun-elevation angle (34.6°) during Pleiades acquisition are reasons of enormous differences on edges of high rise buildings as seen for example on football stadium of Standard of Liège (figure 40).

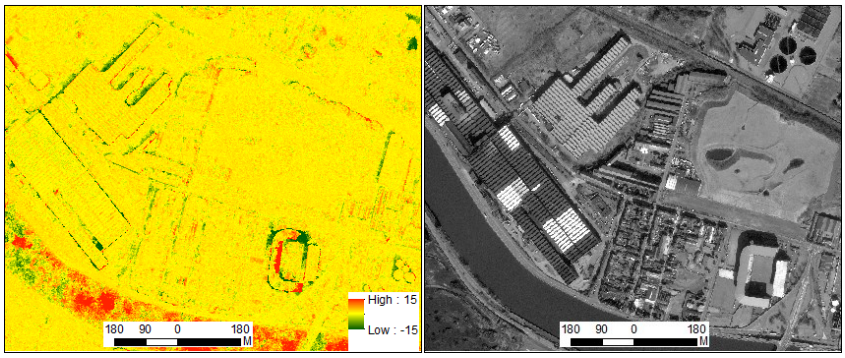

Figure 40: DSM difference in meter (left), panchromatic image of the Pleiades stereopair (right)

In effect, large incidence angles in addition to small sun elevation provoked Westward occlusions and long shadows in opposite sun position on Pleiades images which disturbed and affected negatively the quality of image matching and result in overestimation of elevation on Pleiades' DSM. On contrary, at Eastern parts of high rise buildings, Vexcel is greater than Pleiades (figure 40).

Profiles comparison

To understand the cause of high negative and positive difference values in South, topographic profiles were extracted from DSMs on some specific areas (figure 42, figure 44 and figure 46). On these figures, the arrow indicates the profile's direction.

Profile n°1 (figure 41) drawn across the Northern border of Sart-Tilman plateau, shows overestimation of Pleiades on buildings in the area of undergoing railways constructions (red line with double arrow n° 1) of Kinkempois. This difference is related to matching problems due to the use of 5000*5000 pixels as final resolution in multiple scale approach in detection of tie points of Vexcel aerial images. As consequences, North-Western part of this building was matched with nearest bare soil points (see Vexcel DSM on figure 42) while on Pleiades, the entire building was matched correctly. Also, it is likely that a part of this matching inconsistency is also related to the fact that MICMAC is not fully invariant in terms of contrast.

Red arrows 2, 3, 4 and 5 on figure 41 are located in deciduous forest zones (figure 42). Arrows 2, 3 and 5 indicate altitude overestimation of Pleiades with respect to Vexcel on Westwards sloping forests while arrow 4 shows overestimation of Vexcel with respect to Pleiades on Eastward sloping forests. This difference is related to the effect of slope orientation with respect to illumination which induces canopy cover differences on both Vexcel and Pleiades as

illustrated (figure 42). Also, few tie points detected in forests (figure 25), cause imprecise dense matching.

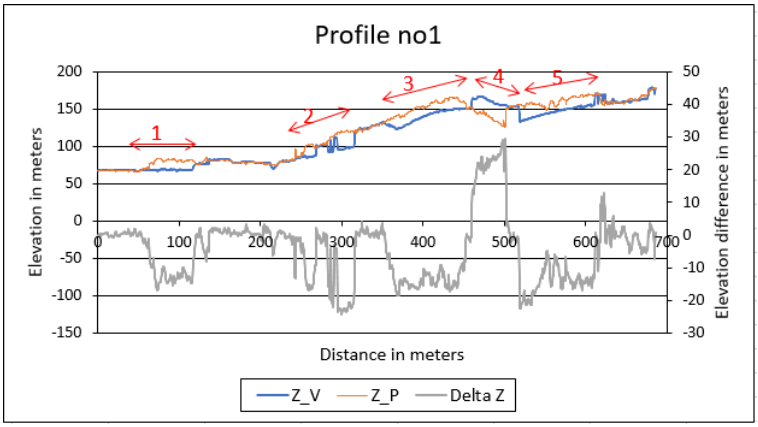

Figure 41: First profile: Delta Z is the difference in elevation between Vexcel and Pleiades; Z_P is the elevation of Pleiades, Z_V the elevation of Vexcel and Delta_Z equals the elevation difference (Vexcel minus Pleiades)

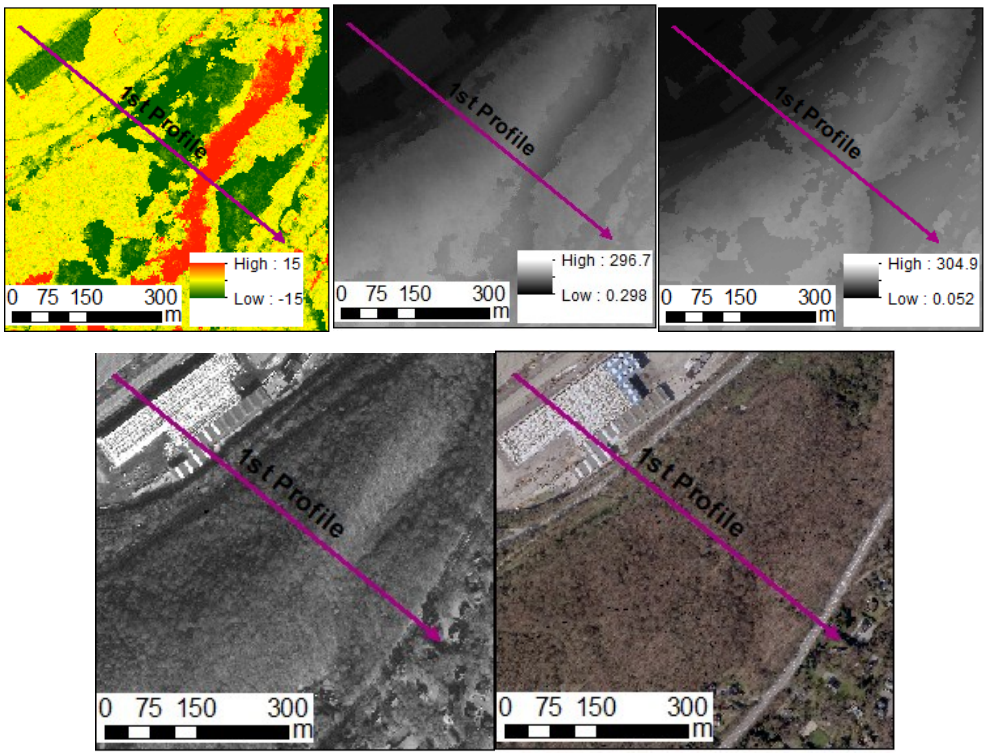

Figure 42: From top left to bottom right: DSM difference in meter, Pleiades DSM, Vexcel DSM, Pleiades orthoimage and Vexcel orthomosaïc.

On 2nd profile (figure 43), at arrow 1, Vexcel altitude is greater than Pleiades because, as seen on both orthomosaïc and orthoimage on figure 44, Vexcel has a denser leaf canopy than Pleiades. On arrow 2, there is aspect of canopy differences due to slope orientation with respect

to incident sun rays during Pleiades acquisition, this implies an error in intersection of homologous rays of Pleiades and results in overestimation of elevation in that particular area.

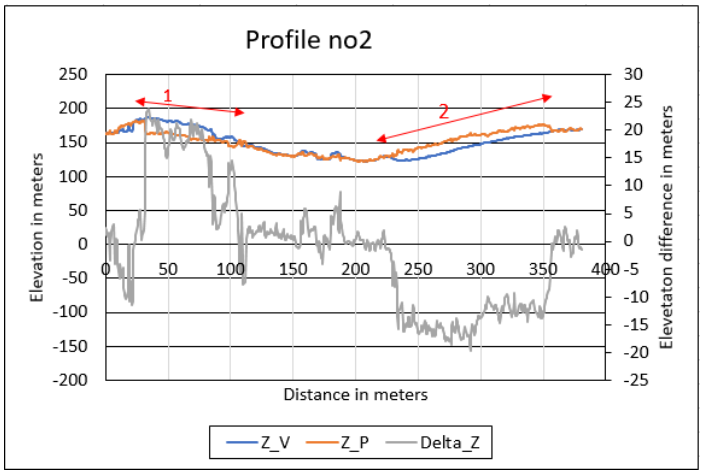

Figure 43: 2nd profile: Delta_Z is the difference in elevation between Vexcel and Pleiades

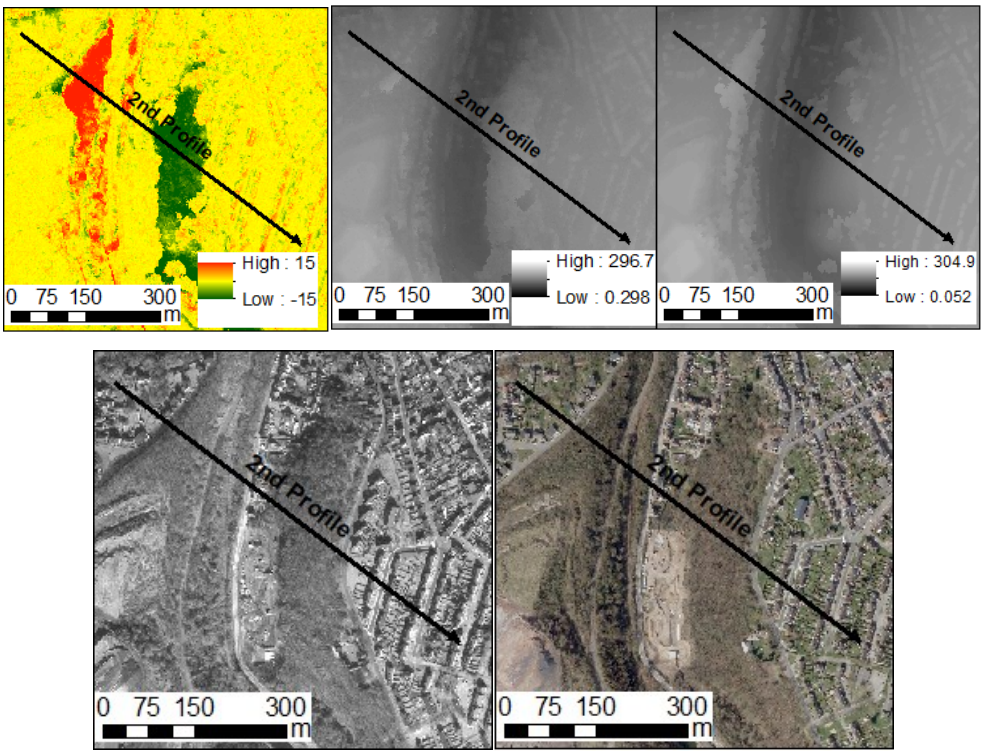

Figure 44: From top left to bottom right: DSM difference in meter, Pleiades DSM, Vexcel DSM, Pleiades orthoimage and Vexcel orthomosaïc.

3rd profile (figure 45) shows on the areas pointed out by red arrows n° 1, 2, 3, 4, 6 and 7), the overestimation of Pleiades altitude while the zone pointed out by red arrow 5 shows higher Vexcel altitude in forest. By analysing DSM surfaces aspect and the orthomosaïc and in those zones, we clearly notice that Pleiades and Vexcel behave differently in decidous forest

according to canopy differences. So, this confirms the findings on previous profiles and shows how dense matching is sensible to canopy cover. As already mentionned, a small difference is detected around urban structures like it is the case at the beginning of this profile (figure 45).

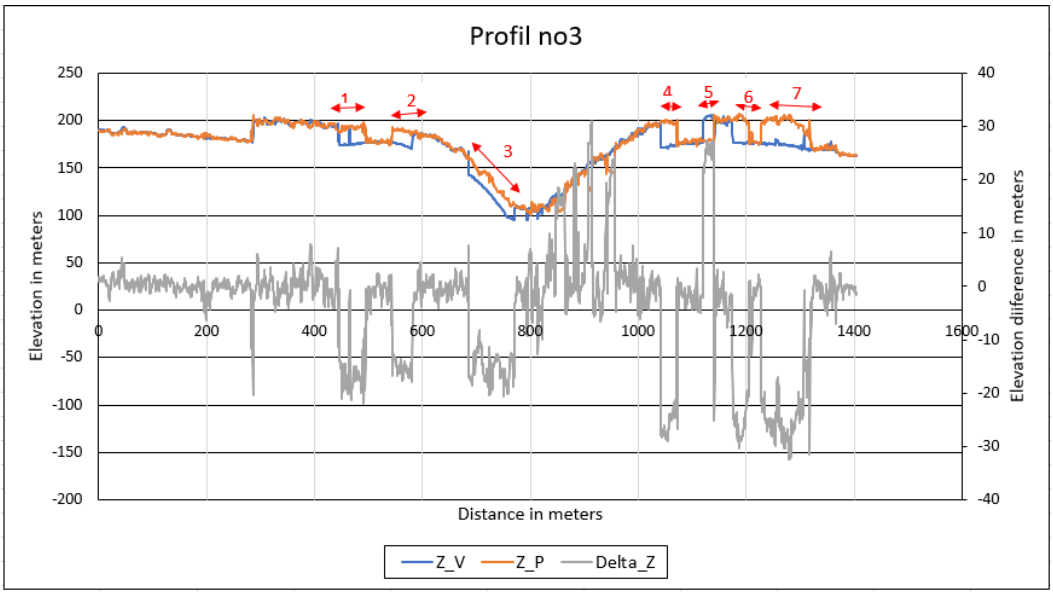

Figure 45: 3rd profile: Delta_Z is the difference in elevation between Vexcel and Pleiades

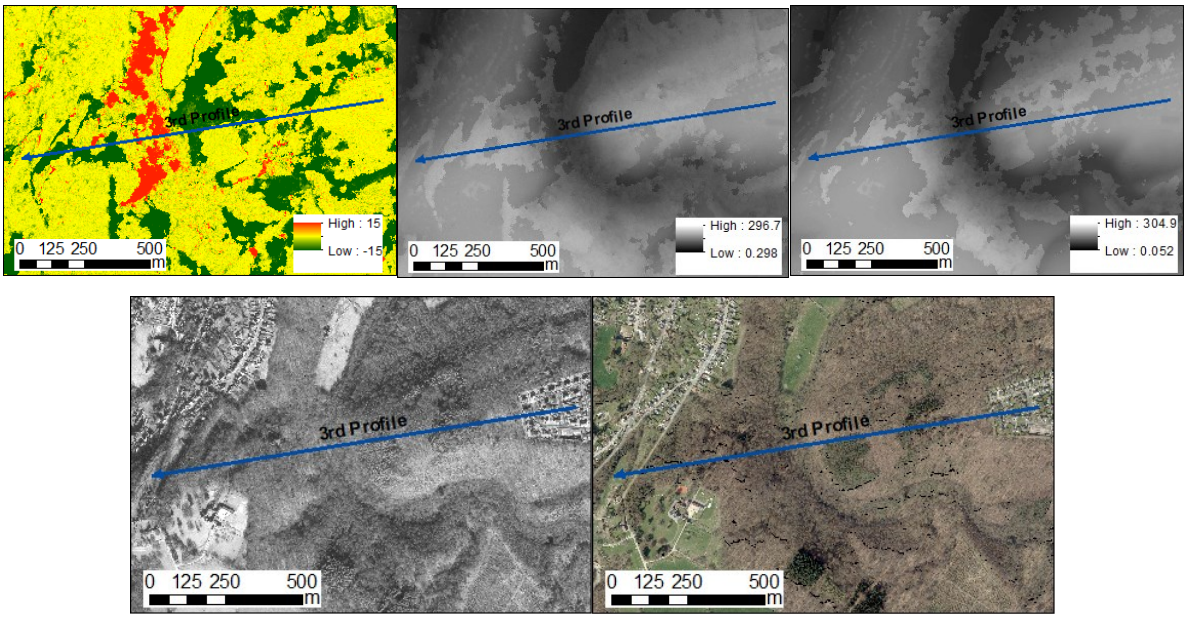

Figure 46: From top left to bottom right: DSM difference in meter, Pleiades DSM, Vexcel DSM, Pleiades orthoimage, Vexcel orthomosaïc.

Hillshaded DSM comparison

Pleiades DSM surface is very rough and noisy compared to Vexcel. Urban and canopy structures are clearly identifiable and better delineated on Vexcel DSM than on Pleiades DSM. This is also the case of buildings shapes and forest boundaries (figure 47).

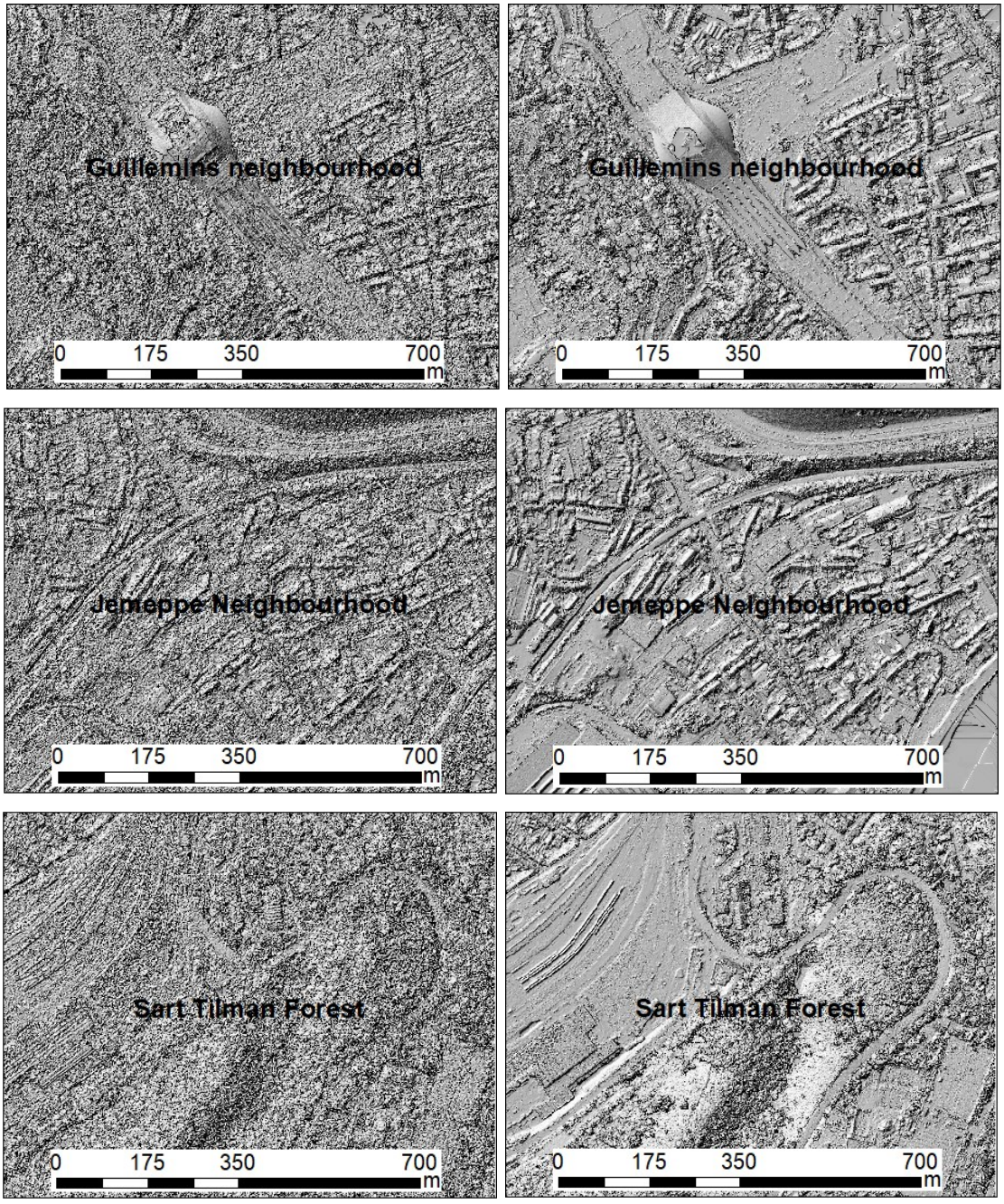

Figure 47: Hillshades comparison: Pleiades (Left) and Vexcel (Right)

V.2.2. Visual comparison of Vexcel 25-cm and Pleiades 50-cm orthoimages

Connections between individual Vexcel orthoimages on the orthomosaïc show very small planimetric shift and radiometric differences as seen on figure 48. Pleiades orthoimage was

produced using 16 bits depth as original radiometric resolution was in 16 bits, so, to avoid contrast issues, it has been converted into 8 bits for analysis purposes. On Pleiades, darkness increases from West to East in the Northern part while Southern is bright (figure 32).

Figure 48: Radiometric inconsistency and small shift between individual orthoimages on orthomosaïc of Vexcel tile_0_1.

Vexcel and Pleiades orthoimages show missing data region in forest (figure 49). West side of high buildings also present missing data parts on Pleiades orthoimage due to occlusions on processed images, this is not observed on Vexcel orthoimages. However, the latter show South-West missing data on buildings located in South of the study area due to the camera position and the resulting parallax distortion of vertical structures located in the border of images of the studied area..

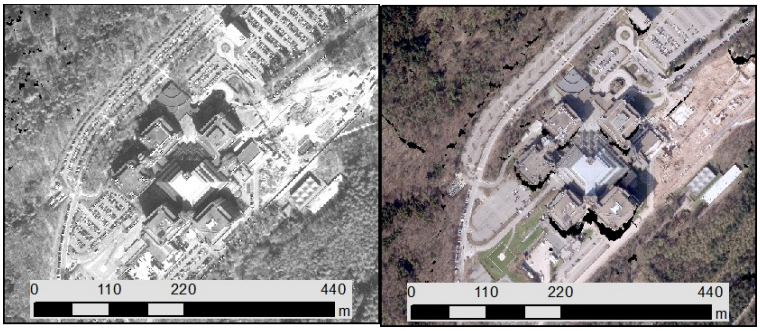

Figure 49: Missing data on orthomosaïc of Pleaides(left) and Vexcel (right)

Phenological differences of canopy are observed on both orthomosaïc in forest zones as a consequence of their respective seasonal acquisition period. A shift in North-East direction of features showed by Pleiades orthoimage with respect to Vexcel orthomosaïc is also detected as it is detailed in section *V.4.*

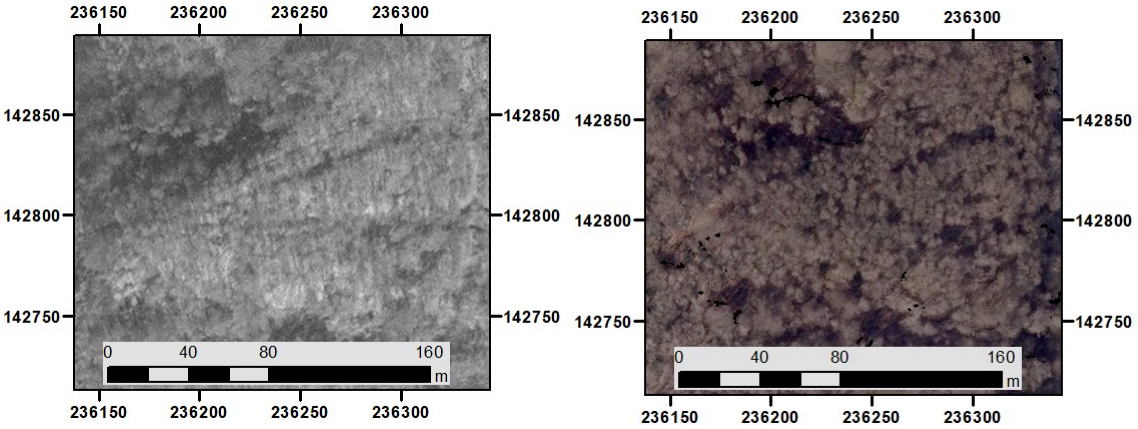

Figure 50: Phenological differences of canopy: Pleiades orthomosaïc (left)and Vexcel orthomosaïc (right)

V.3. Geometric accuracy and precision assessment of photogrammetric DSMs using reference datasets

For height validation, DSM products of Vexcel and Pleiades were compared to two reference data such as *PICC* data produced by the Walloon administration whose 3D uncertainty is at 25 cm and a 1 m resolution DSM also produced by this administration obtained from Lidar measurements carried out between 12/12/2012 and 09/03/2014. While PICC data covered the entire study area, Lidar DSM was only available for the central part of our study area.

Accuracy, precision and uncertainty of our products were assessed statistically with respect to PICC data. Signed error (e) was computed at each PICC point as the difference between PICC and DSM elevations. Imprecision was calculated as standard deviation of this error. Inaccuracy also called bias was defined as the mean of signed error. The evaluation of global geometric quality of products was quantified by uncertainty which integrates both imprecision and inaccuracy. Uncertainty was expressed as root mean square error (RMSE) (Cornet, 2008).

$$e = Z_{reference} - Z_{Vexcel\ or\ Pleiades};$$

$$Inaccuracy = Bias = Mean\ e = (\sum e)/n;$$

$$Imprecision = Standard\ deviaition\ of\ e = \left[\sum (e - \bar{e})^2\right]/n$$

$$Uncertainty = RMSE = \sqrt{\frac{\sum e^2}{n}}$$

V.3.1. Vexcel 25-cm and Pleaides 50-cm DSMs versus PICC reference

Ground level points (PICC code 185), points corresponding to vertices of axes of roads (PICC code 485) and cornice points of buildings (PICC code 204) were involved to stratify the validation of our photogrammetric products. Points from linear features (axes of roads and buildings) were obtained using ArcGIS tool "Feature Vertices to Points". Height values of Pleiades and Vexcel were attributed to PICC points by bilinear interpolation using ArcGIS function "Extract Value to Points". To avoid incoherence in heights, we only extracted elevation values of points inside a polygon excluding nodata zones and edges' artifacts of Vexcel and Pleiades DSM. Positive signed error indicates underestimation of DSM products while negative error means overestimation (table 8). 25% of cornice points have elevation error greater than +1m both on Vexcel and Pleiades due to smoothing effects of buildings shapes of DSM of high spatial resolution images.

Table 8: PICC altitude versus Vexcel and Pleiades DSMs altitude

	Vexcel DSM 25cm			Pleiades DSM		
	Level points	Roads 'axes	Buildings	Level points	Roads 'axes	Buildings
Number of points	193188	75685	521428	45170	67387	449846
Min error	- 63.88	- 93.2	- 35.94	- 117.49	- 96.8	- 35.31
Max error	36.21	135.33	84.69	34.60	16.62	86.69
Inaccuracy	- 2.25	-0.87	0.67	- 3.16	- 1.15	1.44
Imprecision	4.74	2.59	3.70	6.27	3.45	3.18
Uncertainty	5.25	2.73	3.76	7.02	3.6	3.50
Confidence interval at 95%	[-11.49;6.99]	[-5.92;4.18]	[-6.54;7.88]	[-15.39;9.07]	[-7.88;5.58]	[-4.76;7.64]
First Quartile	-1.99	-1.21	-1.05	-3.12	-1.7	-2.42E-10
Median	-0.93	-0.61	-0.28	-0.93	-0.34	1
Third Quartile	-0.12	0.07	1.17	0.05	0.52	2.33

Large maximum and minimum error values were due to urban activities like constructions, demolitions, renovation of urban structures which resulted into elevation value differences because of temporal discrepancy between PICC data and validated DSMs. Higher uncertainty found on level points on both DSMs contrary to the other two categories is caused by industrial activities like quarries which due to digging activities, error greater than 15 m was only observed in bare soil on quarry pit areas on both DSMs.

For roads 'axes points, only 2 and 11 points were beyond +15 m of error respectively on Pleiades and Vexcel. Error less than -15 m was mostly on Eastern part of the study area around Meuse River and with few points in South, this overestimation was found on roads passing through residential areas with high buildings and points under power lines or near electric pylons.

Error on buildings' points less than -15 m or greater than 15 m was observed on few points located at Eastern and centre parts of study area around Meuse River on either Pleiades or Vexcel

For all categories of points, Pleiades is the most uncertain, imprecise and inaccurate. Neither Vexcel nor Pleiades present symmetrical histograms in the three analysed point's categories. As seen on figure 51, level points and roads 'axes points on both Vexcel and Pleiades, have mean error which is smaller than median so, error distribution is skewed to the left while error of buildings points is skewed to the right on both Pleiades and Vexcel as mean error of those points is larger than their median error. It is however important to note that tails on the left of the histograms of level and roads 'axes points of Vexcel are less frequent than on Pleiades, this is to confirm that Vexcel altitude bias is smaller (for mean and median) than Pleiades.

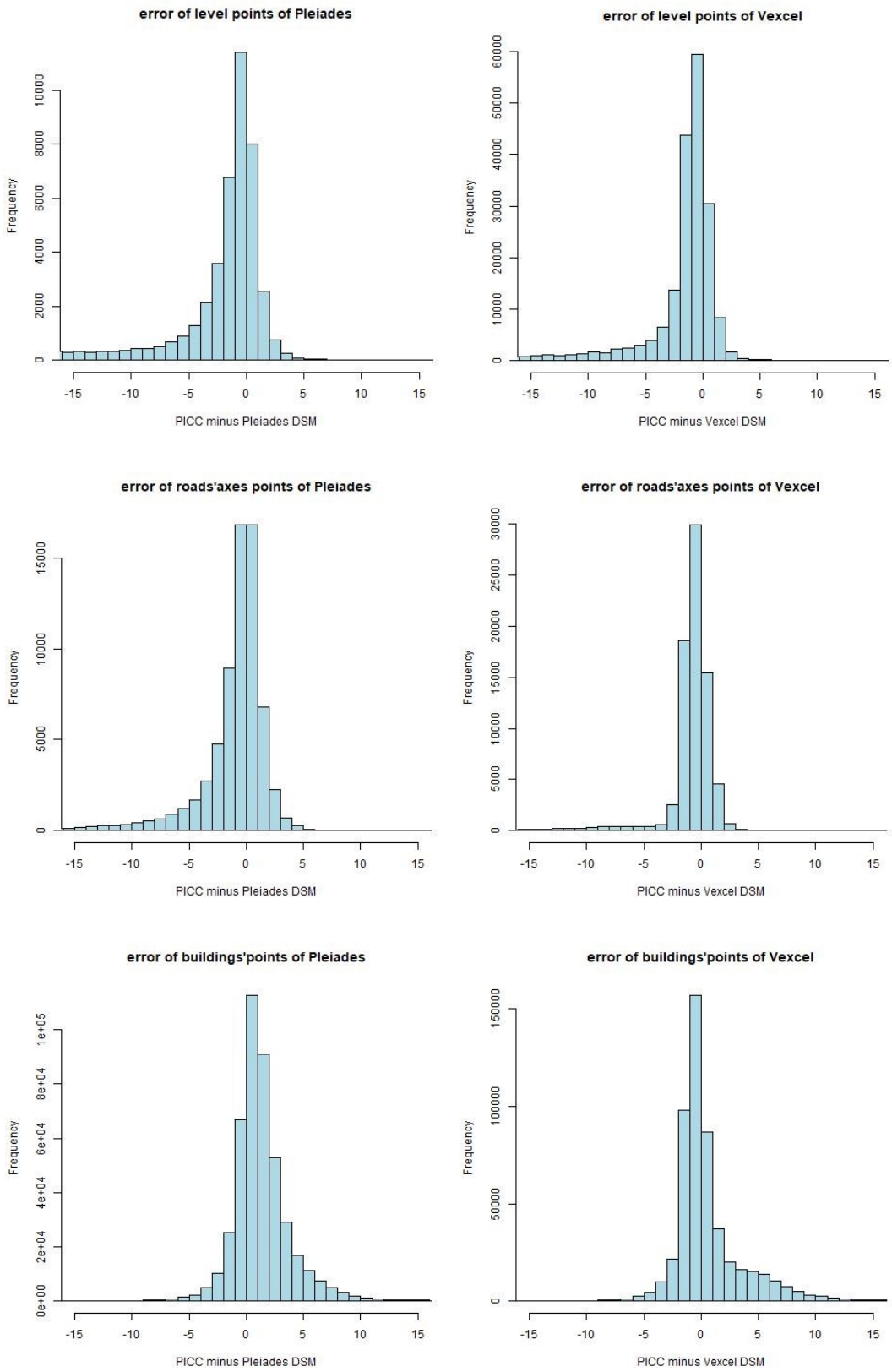

Figure 51: Signed error histogram: Pleiades (left) and Vexcel (right)

V.3.2. Vexcel 25-cm and Pleaides 50-cm DSMs versus Lidar DSM

Lidar reference data is a 1 m spatial resolution DSM. So, it was resampled using nearest neighbour interpolation method at 25 cm and at 50 cm in order to be compared respectively to the 25 cm resolution Vexcel DSM and 50 cm resolution Pleaides DSM.

Comparison of hillshaded DSMs (Vexcel versus Lidar and Pleiades versus Lidar)

As illustrated in figure 52, Vexcel DSM is rougher and noisier than Lidar DSM either in urban area or in forest area. Pleiades DSM is the noisiest at the point that fine structures are not visible (figure 53).

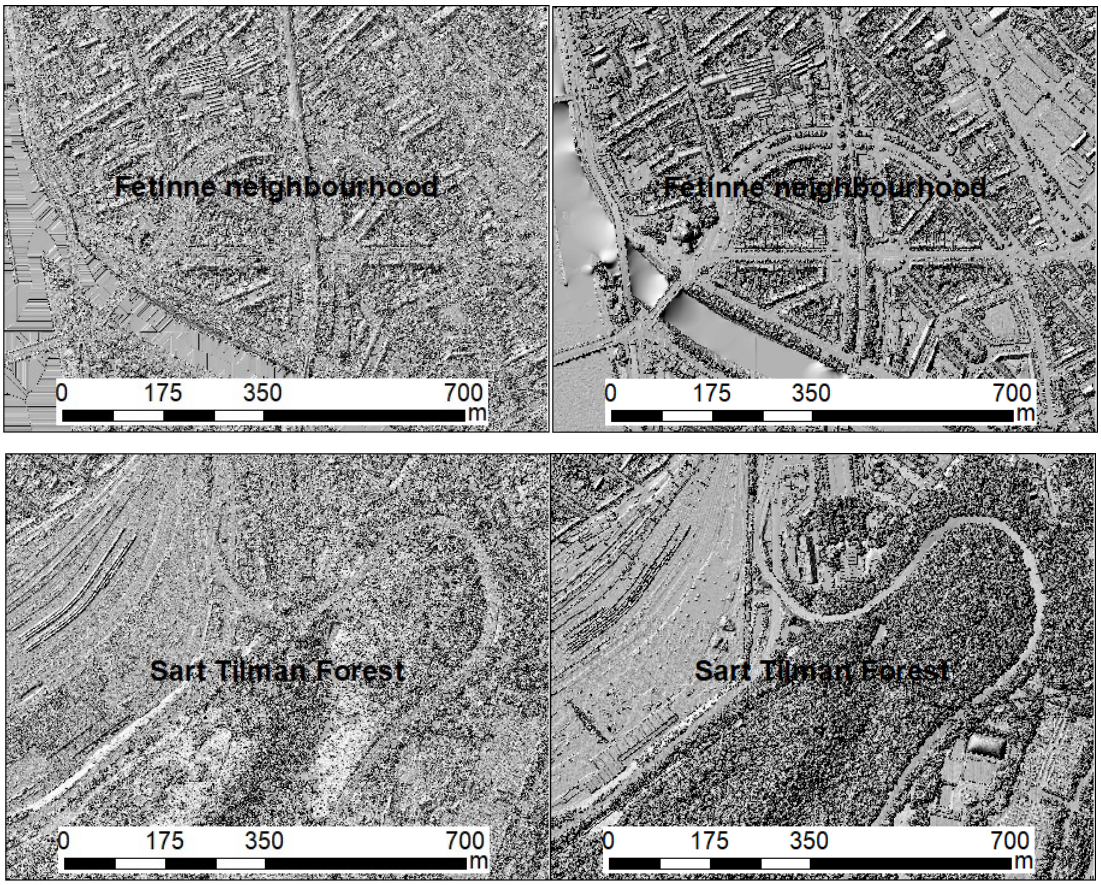

Figure 52: Hillshaded DSM: Vexcel 25cm (left) and Lidar 25cm (right)

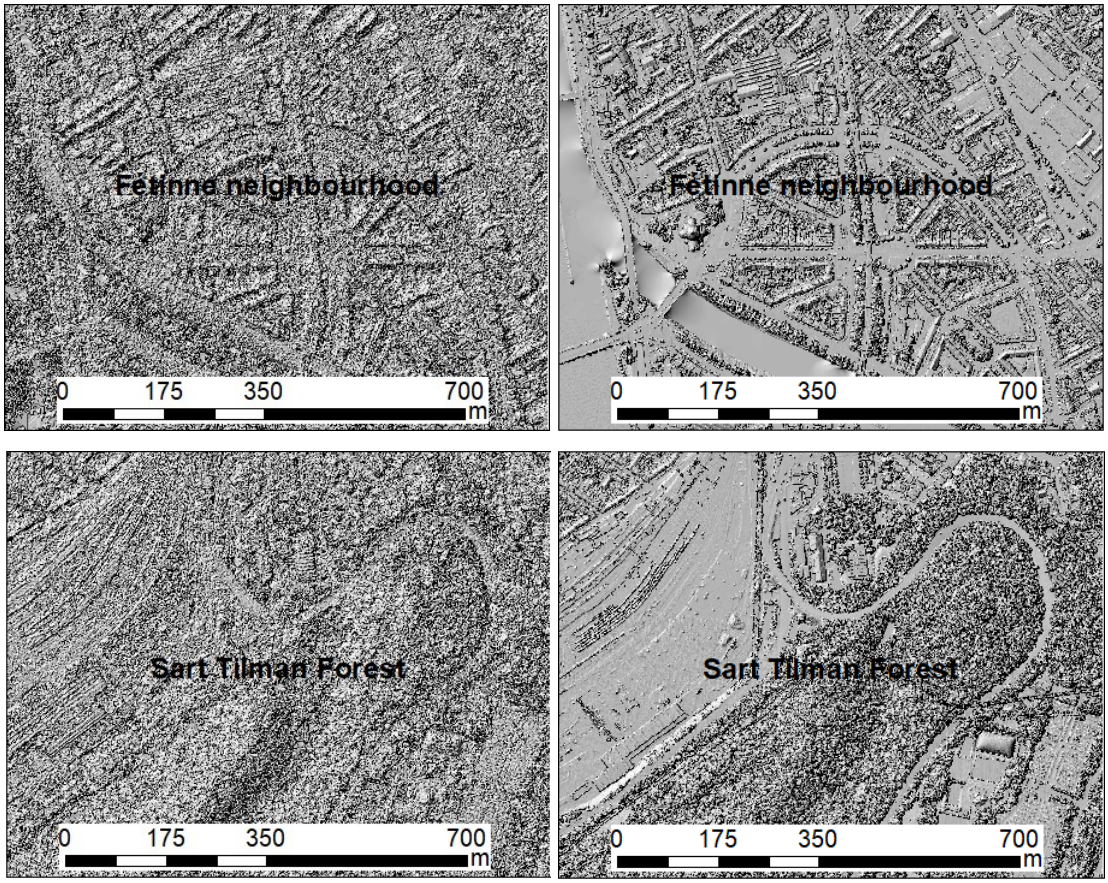

Figure 53: Hillshaded DSM: Pleiades (left), Lidar 50cm (right)

Image subtraction between Lidar and Vexcel DSMs

Elevation difference image (figure 54) was computed by subtracting Vexcel DSM at 25 cm from Lidar DSM resampled at 25 cm clipped at the same extend using the "Minus" function of ArcGIS. Difference image shows extreme positive difference of 201.18 m and extreme negative minimum of -70.40 m, inaccuracy of + 2.75 m and imprecision of 7.84 m. Underestimation of Vexcel elevation greater than 30 m occurs only on the top roofs of high rise structures like towers, antennas and on few buildings. Underestimation of Vexcel elevation within a range of 5 up to 30 m is observed in deciduous forest zones, precisely in trees whose leaves were not sprout, on the Meuse River and on top roof of moderate rise buildings. The main cause of Vexcel underestimation in deciduous forest is related to seasonal period of acquisition (early April) which is different to that of Lidar measurements.

Therefore, forested zones on Vexcel orthomosaïc whose leaves are present and trees seems to be dense, the underestimation is less than 2 m, while in trees which are sparse with few or no leaves, the underestimation is higher than 20 m. In those forested areas, overestimation is only observed on shadow parts due to too low sun elevation during aerial image acquisition.

Overestimation of Vexcel elevation greater than 30 m is observed on few pixels of roofs of high rise buildings at South and East sides of the area covered by both DSMs.

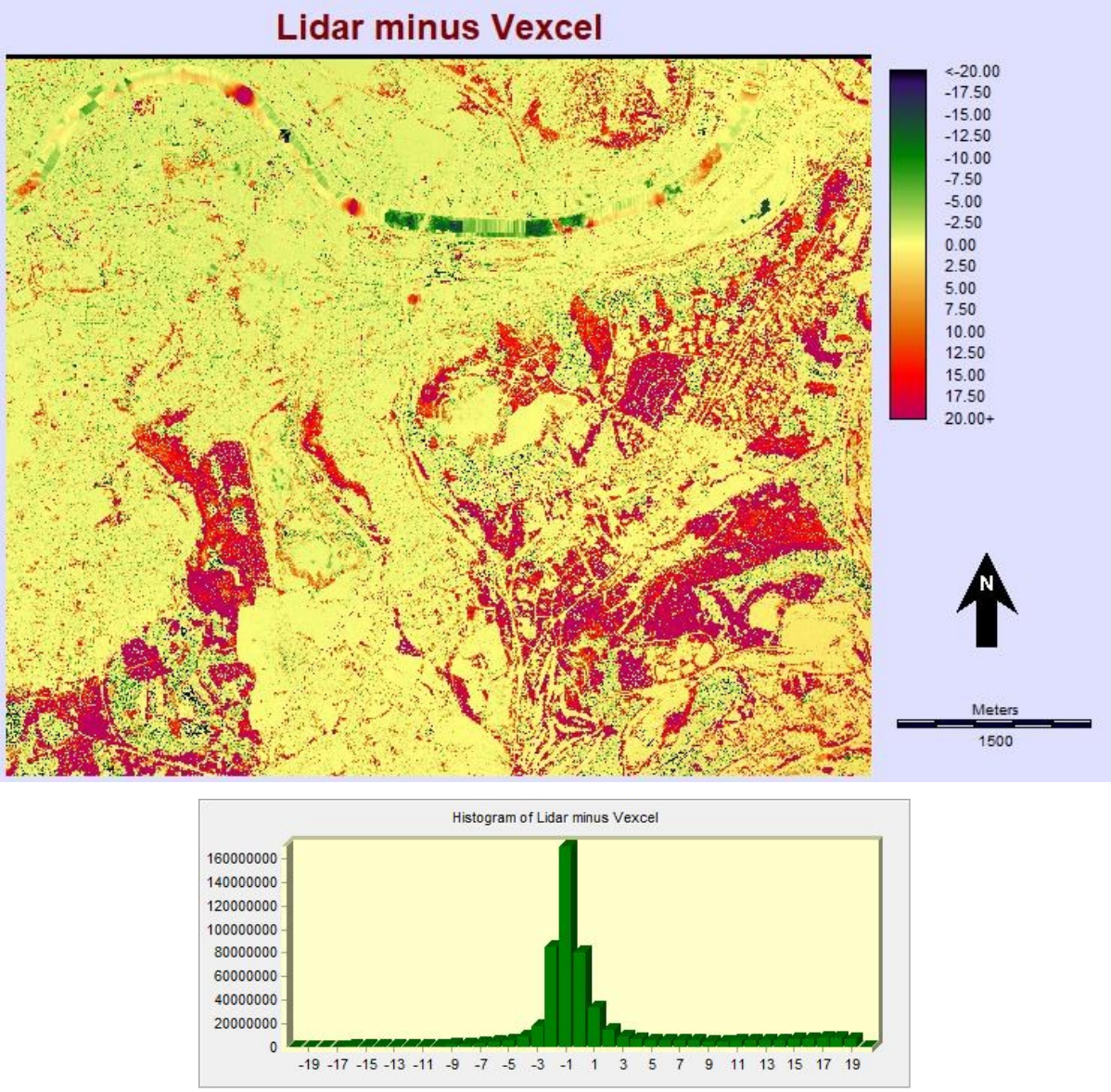

Figure 54: Elevation difference map between Lidar and Vexcel DSMs at 25cm resolution (top) and histogram of differences (bottom).

Overestimation of Vexcel elevation from 5 m up to 30 m is seen on shadow parts of features like buildings, edges of coniferous forests and shadow spaces inside coniferous and deciduous forests and parks, roads passing between high rise buildings and areas between high buildings. These are mainly due to the effect on dense matching of sun elevation during acquisition time of aerial images and to smoothing effect generally noted on photogrammetric DSM in area characterized by high spatial frequencies (road between buildings or urban canyons for instance).

In general, difference between both surfaces depends on land cover, sun elevation and azimuth during image acquisition, height and size of structures (high and low spatial frequencies). For urban structures, large differences exist at few edges of buildings, on top roof of high rise buildings and on roads within high rise building areas. Globally, small (even no) differences in urban areas (roof of buildings, roads and rails ways), coniferous trees, grasslands and bare soils areas.

Correlation between Vexcel and Lidar DSMs

Correlation between Vexcel and Lidar elevations has been analysed by computing the regression line using R software. A polygon covering common zone of Vexcel, Pleiades and Lidar was used to delimitate this analysis. In that polygon 99718 points were randomly sampled using nearest neighbour interpolation method and elevation values of Vexcel DSM, Lidar DSM and Pleiades DSM were attributed to those points through "extract multi values to points GIS tool".

Coefficients were calculated by least square adjustment algorithm which minimizes residuals by computing the tendency line that best fits the given cloud points. The simple linear model is formulated as:

$$y_i = a\,x_i + b + e_i$$

$$\hat{y}_i = a\,x_i + b$$

where x is the elevation value from the Lidar DSM at 25 cm of resolution, y is the elevation value from Vexcel DSM at 25 cm of resolution, a is the slope and b the intercept of the linear model, $\hat{y}$ the estimated value of y and e the residual value.

a and b coefficients were adjusted from next formulas:

$$a = \frac{cov(x,y)}{s_x^2} \text{ and } \mathrm{b} = c_y - a * c_x$$

with (c_x, c_y) the gravity centre of all the observations.

Using R software, we found:

```
Call:
lm(formula = vexcel_25 ~ lidar_25)

Coefficients:
(Intercept)     lidar_25
     2.9490       0.9648
```

The adjusted regression equation obtained is:

$$\hat{y} = 0.9648\,x + 2.949.$$

From complete statistics reported below, residual values (e_i) which are differences between observed and estimated values, showed large extreme values which means that some values are far away from regression line. Although residuals' median different and greater than zero (1.456) indicates that residuals are not normally distributed. 50% of pixels lying between the first and third quartile, have residuals values between -0.955 and 4.625 m.

The standard error of regression coefficients (slope and intercept) measure the uncertainty in their estimate, better values should be close to 0 as it is the case (0.0003 for slope and 0.057 for intercept). Obviously, large amount of points used in adjustment process makes a population instead of a sample, consequently, conformity tests on those coefficients (Student) show very small probability which means that regression coefficients are relevant. Residual standard error is the standard deviation of residuals; this value being high explains that residuals are very variable due to influence of high minimum and maximum residual values. The slope value near to 1 indicates a quasi-direct association between both elevations while the associated positive intercept far from 0 indicates a mean overestimation of Vexcel elevation.

R-square evaluates the goodness of fit of the model, it varies from 0 to 1 in which 1 means best fit. It indicates the ratio between the explained variance by the model and the total variance of the dependant variable (y). Having R^2 of 0.9887 means that 98.87% of total variance of Vexcel elevation is explained by regression model, this indicates a good correlation between Vexcel and Lidar. The signification test on R-square (F-test) which compares y variance explained by the model to the residual variance, shows small probability, hence, confirms that the R-square is highly significant but this is again due to the very large number of observations.

```
Call:
lm(formula = vexcel_25 ~ lidar_25)

Residuals:
    Min      1Q  Median      3Q     Max
-95.086  -0.955   1.456   4.625  44.786

Coefficients:
             Estimate Std. Error t value Pr(>|t|)
(Intercept) 2.9489561  0.0576923   51.12   <2e-16 ***
lidar_25    0.9648006  0.0003266 2954.13   <2e-16 ***
---
Signif. codes:  0 '***' 0.001 '**' 0.01 '*' 0.05 '.' 0.1 ' ' 1

Residual standard error: 7.321 on 99716 degrees of freedom
Multiple R-squared:  0.9887,    Adjusted R-squared:  0.9887
F-statistic: 8.727e+06 on 1 and 99716 DF,  p-value: < 2.2e-16
```

On figure 55, points located in forested areas are those that are far from the regression line and obviously they are the reasons of high residual standard error. Despite this, Vexcel elevation is well correlated to Lidar elevation.

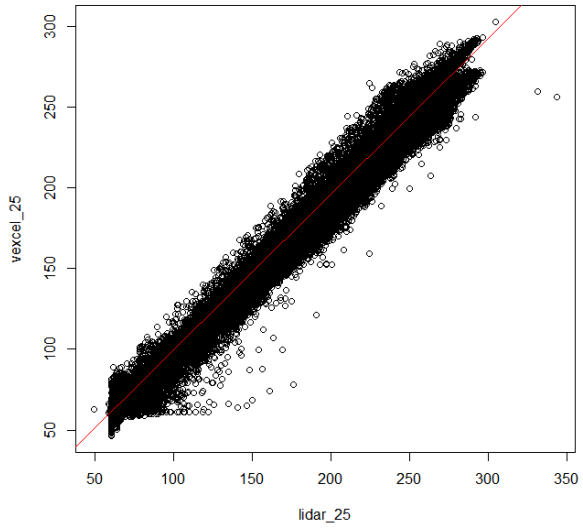

Figure 55: Regression line between Vexcel and Lidar elevations at 25 cm; values are expressed in meter

Topographic profile comparison: Vexcel versus Lidar DSMs

First and second topographic profiles analysed in section Vexcel (figure 42 and figure 44) were considered, Differences ($Z_{Lidar} - Z_{Vexcel}$) on first profile oscillate within + and - 20 m with some exceptional values reaching + 40 m. But positive difference values are predominating.

From figure 56, two DSM surfaces are nearly the same in deciduous forests whose leaves were greenish (example at arrow 7) and on urban structures (figure 57) like at arrow 1. At red arrow 2, the buildings were not yet constructed at the time of Lidar measurement, hence, Vexcel DSM is overestimated. At arrows 3, 4, 6, 8 and 9 located in deciduous forest whose leaves were not

yet out, there is an underestimation of Vexcel elevation. Arrow 5 indicates a zone of underestimated Vexcel elevation on power lines which is illustrated by blue line peaks. This profile shows that Vexcel DSM is sensible to seasons but independent to slope variation in the profile direction as it is shown by arrow 7 which is actually located in a changing slope from Eastward to Westward.

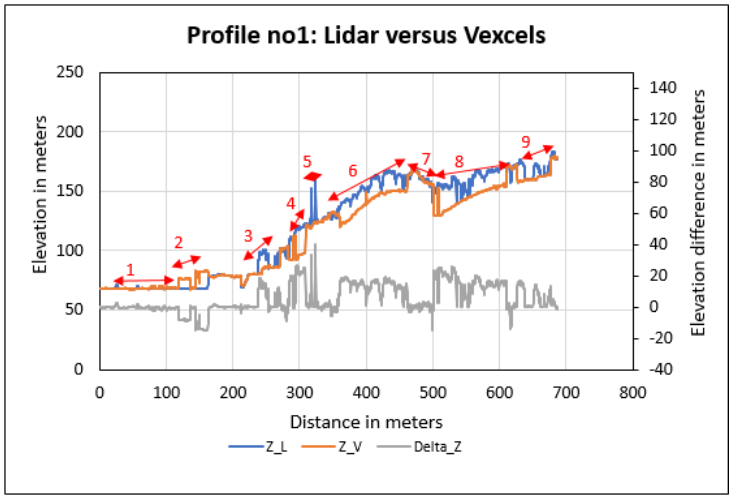

Figure 56: First topographic profile through Lidar and Vexcel DSMs: Z_L , Z_V are Lidar and Vexcel elevations respectively and Delta_Z is Z_L minus Z_V.

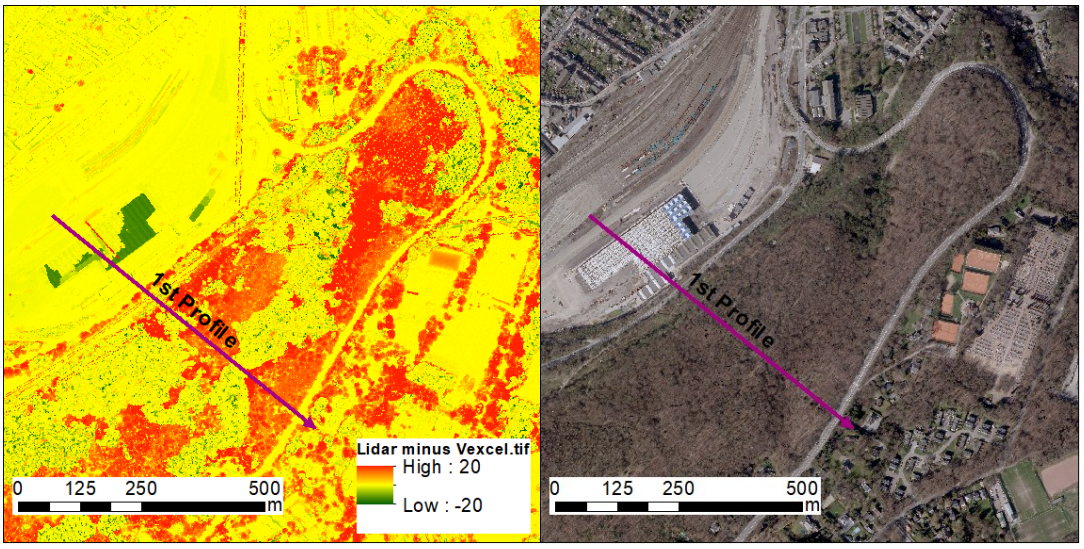

Figure 57: Altitude difference between Lidar and Vexcel DSMs at 25 cm (left) and Vexcel 25 cm orthomosaïc (right)

On second profile (figure 58), elevation difference is within + and – 20 m and positive differences are also predominating. Arrows 2, 3 and 4 are in leaves-free deciduous forests (see right image of figure 59), even though they indicate zones of underestimation of Vexcel elevation as it is commonly noticed in deciduous forests whose leaves were not yet green during

aerial flight mission in April. It is important to note that, the more trees are brown (means trees with no green leaves in April) the more Vexcel elevation is underestimated and more the leaves are green, the fewer the elevation difference.

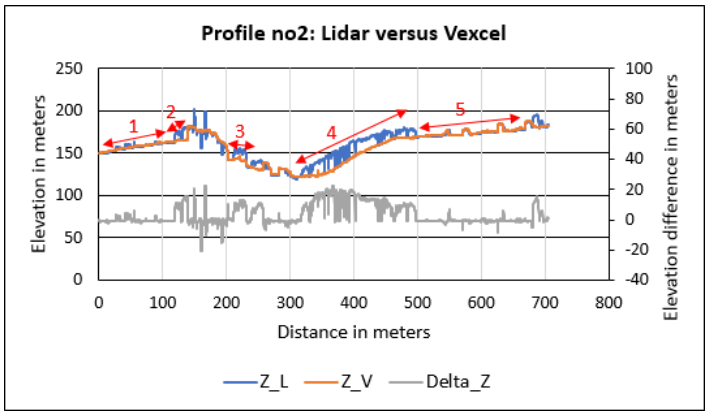

Figure 58: Second topographic profile and altitude difference profile between Lidar and Vexcel at 25 cm

Between arrow 2 and 3 there are forests whose leaves are becoming (or already) green, so there is small difference of elevation with downward-peaks in free space inside forests and upward-peaks in power lines passing over forested areas. On contrary to Vexcel DSM, power lines are visible on Lidar DSM, which obviously results in underestimation of Vexcel DSM. This second profile emphasize the findings on first profile that small differences are seen in urban structure areas while large differences are observed in forested areas.

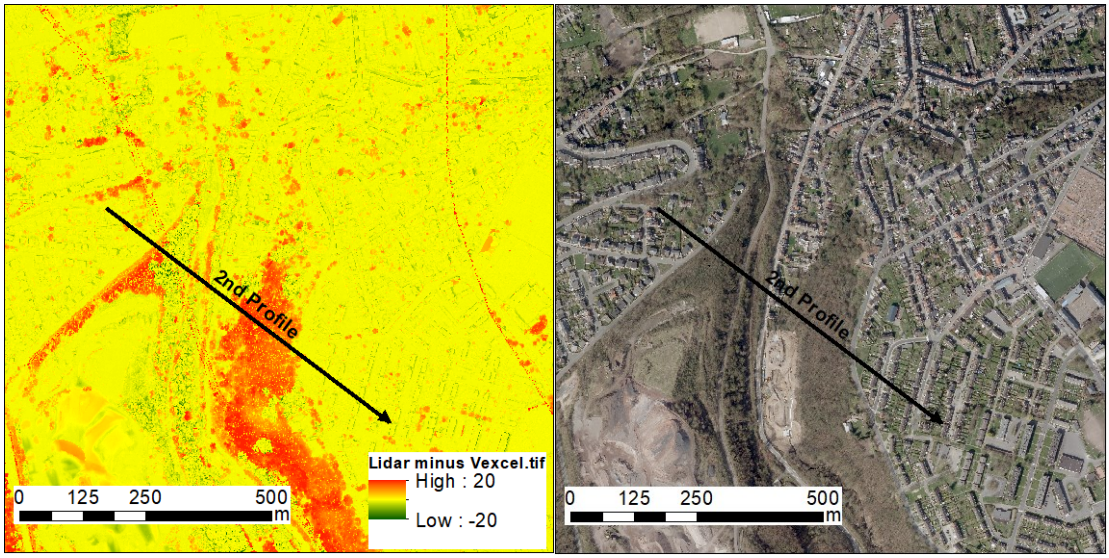

Figure 59: Altitude difference between Lidar and Vexcel DSMs at 25 cm (left) and Vexcel 25cm orthomosaïc(right)

Image subtraction between Lidar and Pleiades DSMs

With Minus function of ArcGIS, Pleiades DSM was subtracted from Lidar resampled at 50 cm. The difference image (figure 60) shows a maximum underestimation of altitude on Pleiades DSM of 193.28 m and a maximum overestimation of 64.74 m, a standard deviation (imprecision) of 7.15 m and an average difference values (uncertainty or bias) of + 2 m which explains that Pleiades elevation is generally underestimated with respect to Lidar measurements.

Overestimation of above 30 m is noted at few pixels at South and West sides of high buildings and few along Meuse River. Underestimation higher than 30 m is only detected at electric pylons and high gas chimneys of Cockerill-Sambre. Pleiades 'overestimation of 5 m up to 30 m are present at Western sides of buildings, Western borders of coniferous forests, free spaces insides coniferous forested zones and along roads surrounded by high residential buildings. This overestimation is due to the observation direction of Pleiades satellites (North-West and South-West) during images capture. Underestimation of Pleiades between 5 and 30 m is observed in deciduous forests whose leaves were not yet green, and at Eastern roofs of high buildings. As explained above, large differences in deciduous forests are the consequences of the acquisition season of Pleiades images (early Spring).

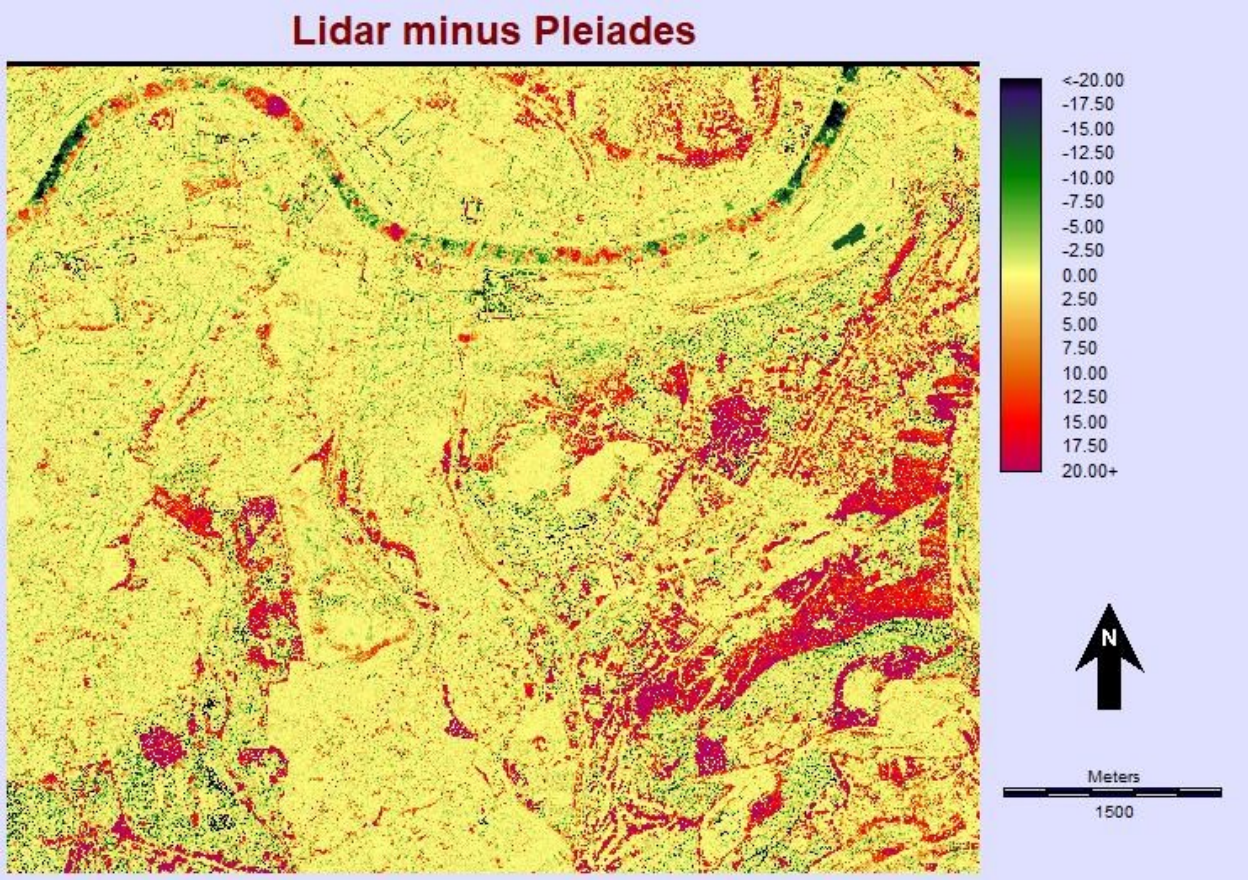

Figure 60: Elevation difference map between Lidar and Pleiades DSMs ($Z_{Pleiades} - Z_{Lidar}$) at 50 cm resolution

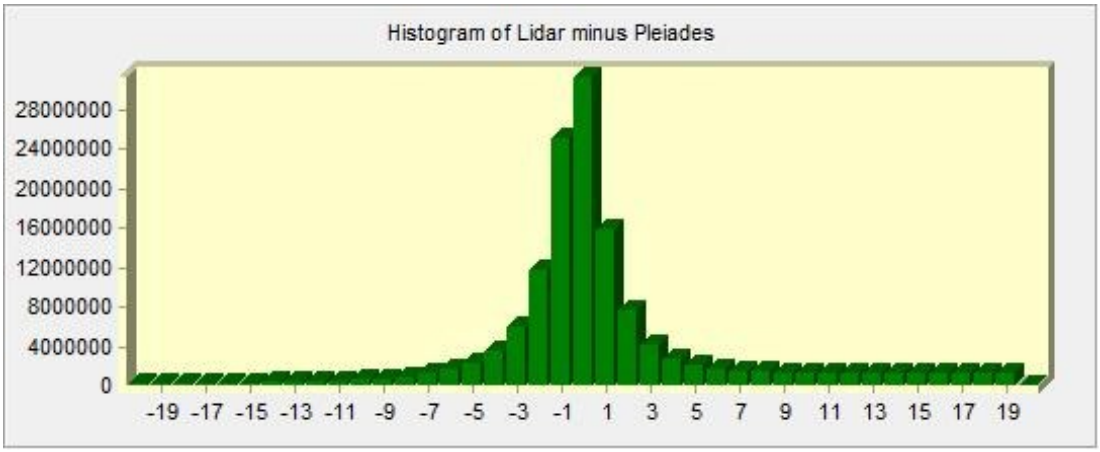

Figure 61: Histogram of elevation difference between Lidar and Pleiades DSMs ($Z_{Pleiades} - Z_{Lidar}$).

In general, overestimation greater than 20 m is discernible in occlusions areas between adjacent high buildings and insides forests, path-ways within forests and West sides of high-rise buildings. Underestimation greater than 20 m is apparent in deciduous forests whose leaves were still not yet coming (means not yet green). This large underestimation was also observed

on particularly roofs of high rise buildings. Middle range difference is visible in grasslands and bare soil areas. Almost null differences are observed in free sky-view roads and railways.

Profile comparison: Lidar DSM versus Pleiades DSM

Topographic cross sections used in the analysis of Vexcel DSM with Lidar measurements were kept to evaluate the elevation differences in the same areas on Pleaides DSM with respect to Lidar DSM.

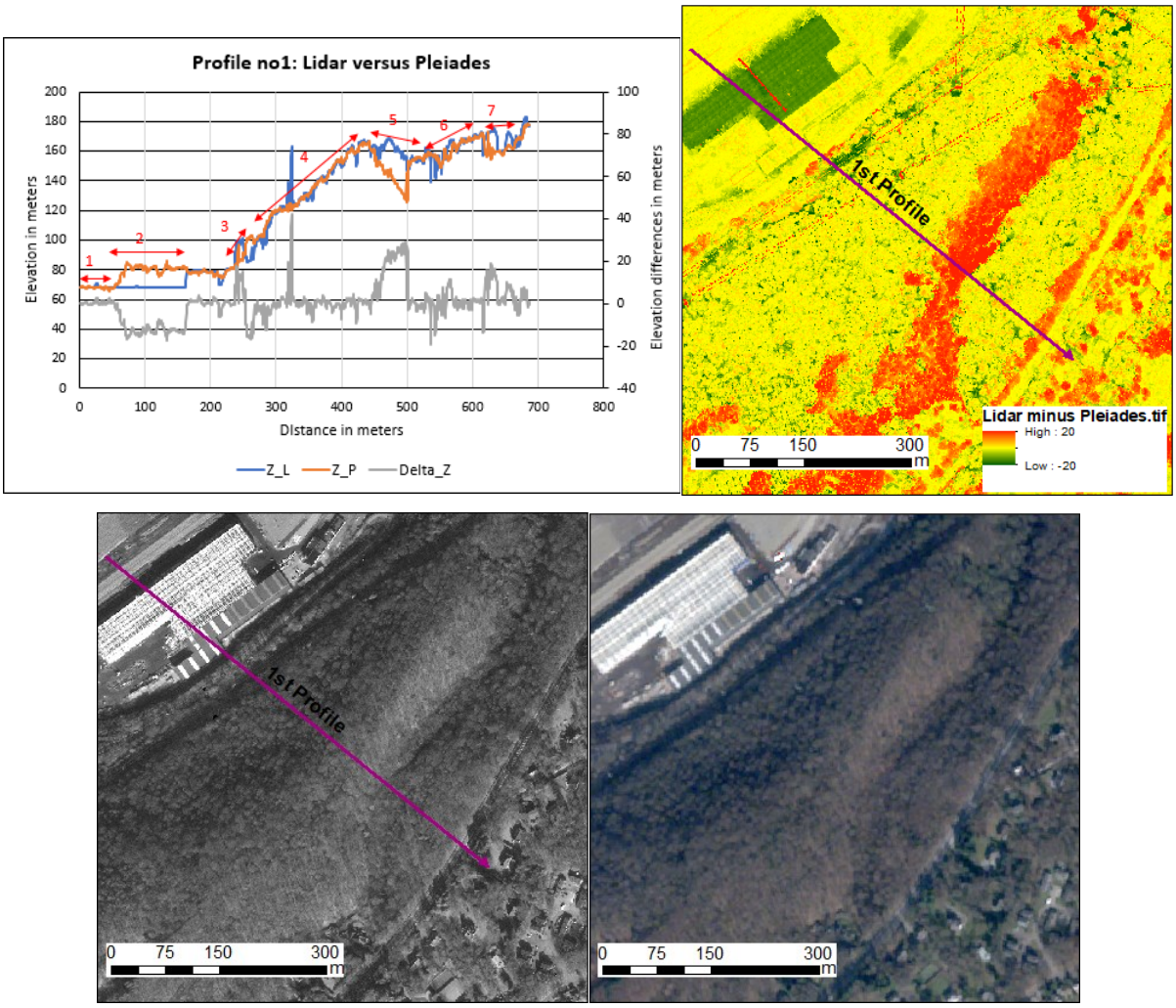

Figure 62: Topographic profiles (top left), altitude difference profile between Lidar and Pleiades DSMs at 50 cm resolution (top right), Pleiades orthoimage (bottom left) and multispectral Pleiades image (bottom right)

On profile n° 1 (figure 62), the difference values are within -20 m and +30 m. Along railways, they are smaller (red arrow 1). The building constructed in Kinkempois train station after Lidar measurements resulted into overestimation of Pleiades elevation *vis à vis* to Lidar (red arrow 2). At arrow 3, there is underestimation of Pleiades height in deciduous forests whose leaves

were not yet green but altitude is overestimated by Pleiades in coniferous forests. Slight differences are observed at arrow 4 which crosses deciduous forests whose leaves are dense and green. Blue line (Lidar DSM) shows peaks at arrow 4 where Pleiades altitude is underestimated due to the fact that matching procedure is not done on the powerline not visible at 50 cm resolution.

Arrow 5 and 4 are in the same deciduous forests, except that arrow 5 is located in a small valley between East-oriented and West-oriented slopes and whose leaves were not yet sprout (see multispectral image of Pleiades on figure 62). This underestimation is thus attributed to canopy differences due to slope orientation with respect to incident sun rays which cause a delay in leaves growth of trees in arrow 5 compared to surrounding trees (indicated by arrow 4 and 6). Arrow 6 indicates a deciduous forest covers with dense leaves in which there are small differences, however there exist on the blue line some downward peaks, due to free space between trees.

Arrow 7 is also located in deciduous trees. It presents the underestimation of Pleiades altitude related to leaves greenish issues evoked above.

On profile n° 2 (top left of figure 63), there is slight difference in residential areas (arrow 1). Low Leaves' density and low greenish deciduous forests cause underestimation of Pleiades altitude (red arrows 2, 3 and 5). Free space between trees caused downward peaks (at arrow 4) on blue line which represents Lidar DSM profile while powerlines crossing over forests caused upward peaks (arrow 2). In urban structures, there is small elevation difference between Lidar and Pleiades DSMs as shown at arrow 6 (top left of figure 63).

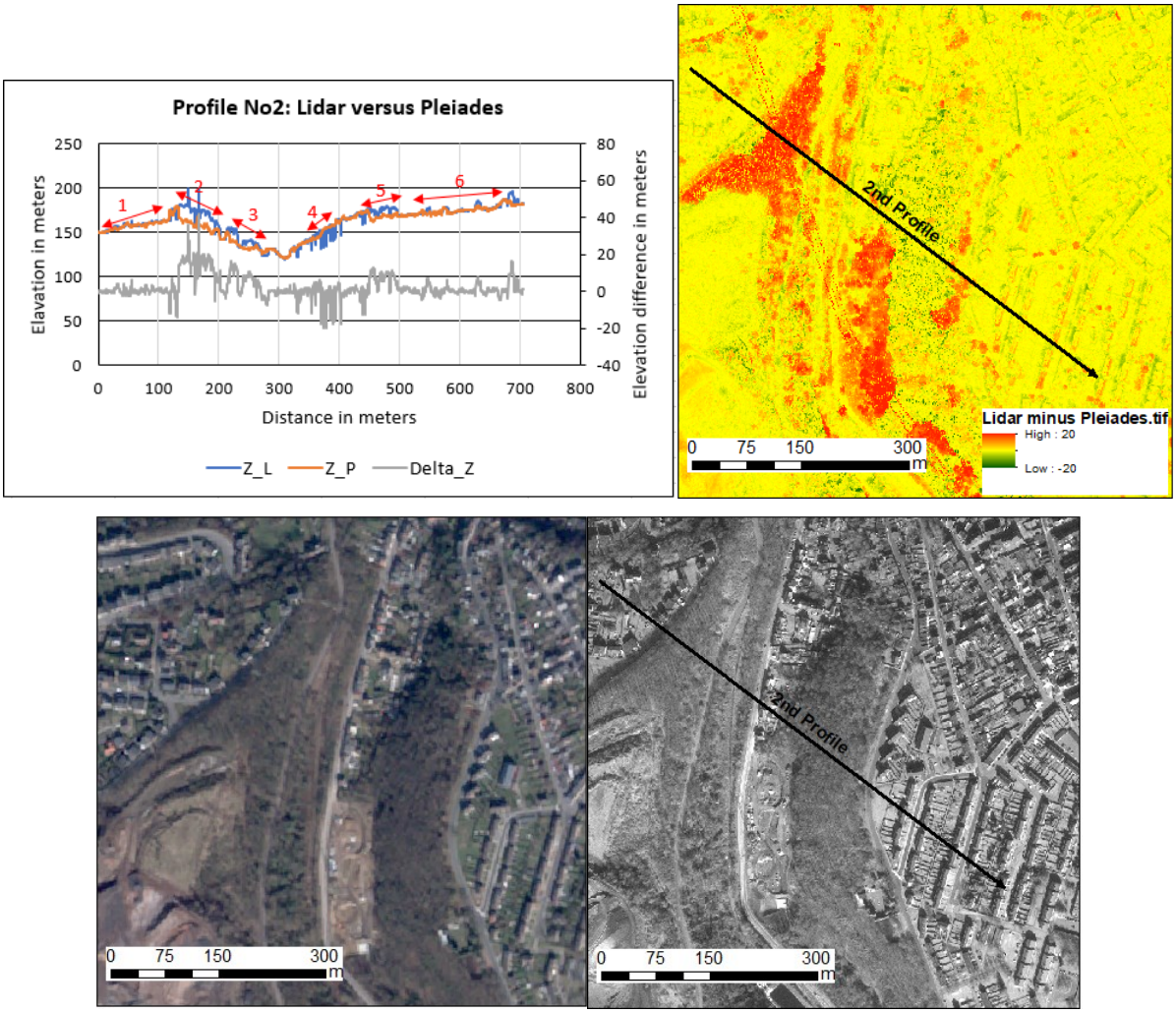

Figure 63: Topographic profile (top left), difference profile between Lidar and Pleiades (top right), Pleiades orthoimage (bottom left) and multispectral Pleiades image (bottom right).

Correlation between Pleiades and Lidar DSMs

Same 99718 points used in analysis above (correlation between Vexcel and Lidar DSMs) were kept and the same procedures were undertaken to evaluate the relationship between Pleaides and Lidar DSMs at 50 cm of resolution.

Based on statistics obtained from R, the regression model calculated by specifying Pleiades as the dependent variable and Lidar as the independent variable is:

$$\hat{y} = 0.9822\,x + 0.8798.$$

The slope value is similar to that found for Vexcel. It is quasi equal to the unity, therefore, there is a quasi-direct association between both altitude values. Small average of underestimation of Pleiades 'elevation is testified by its smaller intercept than that computed for Vexcel.

Complete statistics reported below show positive median residual. Frequent high extreme residuals produce high residual standard error of 6.822 m. 50% of residuals are between -0.867 and 3.2 m which is smaller interquartile dispersion of residual than the one obtained for Vexcel. Regression model best explains Pleiades elevation in function of Lidar elevation at 99.05%, this shows a strong relationship between Pleiades and Lidar elevation. Points falling far from tendency line are those in deciduous forests (figure 64).

```
Call:
lm(formula = pleiades ~ lidar_50)

Coefficients:
(Intercept)     lidar_50
     0.8798       0.9822

Call:
lm(formula = pleiades ~ lidar_50)

Residuals:
    Min      1Q  Median      3Q     Max
-95.598  -0.867   1.229   3.167  44.771

Coefficients:
             Estimate Std. Error t value Pr(>|t|)
(Intercept) 0.8797696  0.0537633   16.36   <2e-16 ***
lidar_50    0.9822432  0.0003043 3227.37   <2e-16 ***
---
Signif. codes:  0 '***' 0.001 '**' 0.01 '*' 0.05 '.' 0.1 ' ' 1

Residual standard error: 6.822 on 99716 degrees of freedom
Multiple R-squared:  0.9905,    Adjusted R-squared:  0.9905
F-statistic: 1.042e+07 on 1 and 99716 DF,  p-value: < 2.2e-16
```

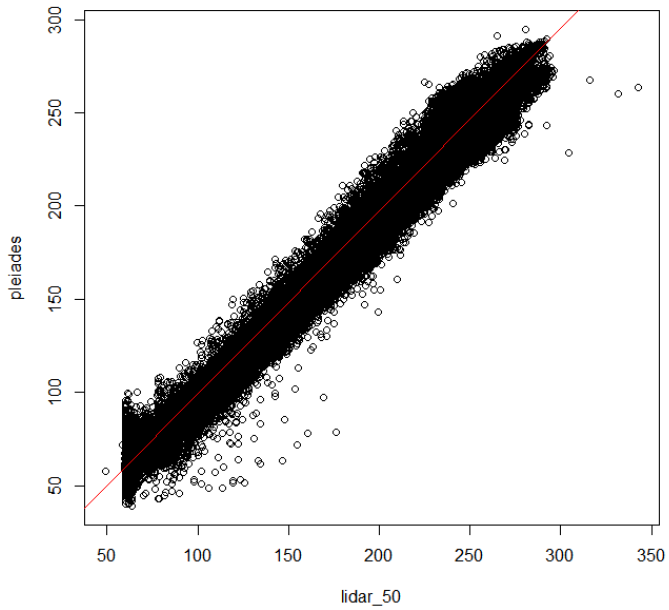

Figure 64: Regression line between Pleiades and Lidar elevations from 50 cm resolution DSMs; values are expressed in meter

As a conclusion, the use of a limited computer capacity during processing of aerial images caused possible final resolution for tie point detection to be 5 000 (5 000 * 5 000 pixels) instead of performing this computation on whole images; each of 17 310*11 310 pixels, as consequences, the quality of the resulted photogrammetric products was very degraded. This resulted for example into an underestimation of Vexcel DSMs on building located in Kinkempois train station.

50 cm of GSD of Pleiades played an important role in deteriorating precise image measurements of GCPs used in RPC refinement. On Vexcel, this problem was not present that's why planimetric errors of CPs are smaller on Vexcel than on Pleiades. The lack of GCPs in top and bottom part of block images in bundle adjustment, affected less Vexcel DSM than Pleiades DSM, in the way that, the refined RPC presented a geometric shift in those particular parts of stereopair.

Effects associated to canopy cover differences of deciduous forested areas was detected, for instance, where Vexcel presented denser leaf canopy than Pleiades, Vexcel elevation was greater than Pleiades elevation. However, Vexcel DSM and Pleiades DSM was found slightly different in coniferous forests.

Small elevation difference between Vexcel and Pleiades DSMs was found in areas covered by urban structures but roads within high-rise residential buildings had large differences, this is because, on high-rise buildings, Pleiades elevation is overestimated on West sides and underestimated on East sides. This behavior of Pleiades elevation with respect to high-rise buildings is a consequence of both Pleiades' small B/H ratio and satellites orientation during stereo pair acquisition.

Both Vexcel and Pleiades have similar slope value whose magnitude is near to 1, which indicates a quasi-direct relationship between each of them and Lidar measurements, thus, implies a quasi-direct association between themselves.

V.4. 2D geometric uncertainty of Vexcel and Pleiades orthoimages versus the reference datasets

By overlapping PICC data on Pleiades Orthoimage, we found that Pleiades orthoimage is geometrically shifted toward North-East. Insufficient GCPs in Southern and Northern parts, caused a failure of accurate RPC refinement and resulted into a planimetric shift.

The magnitude of this shift is larger on Southern part of the study area than on Northern part. However, in the central part, there isn't any shift observed (figure 66). The analysis of Vexcel orthomosaïc indicates perfect spatial correspondence with PICC data throughout the study area (figure 65, figure 66 and figure 67).

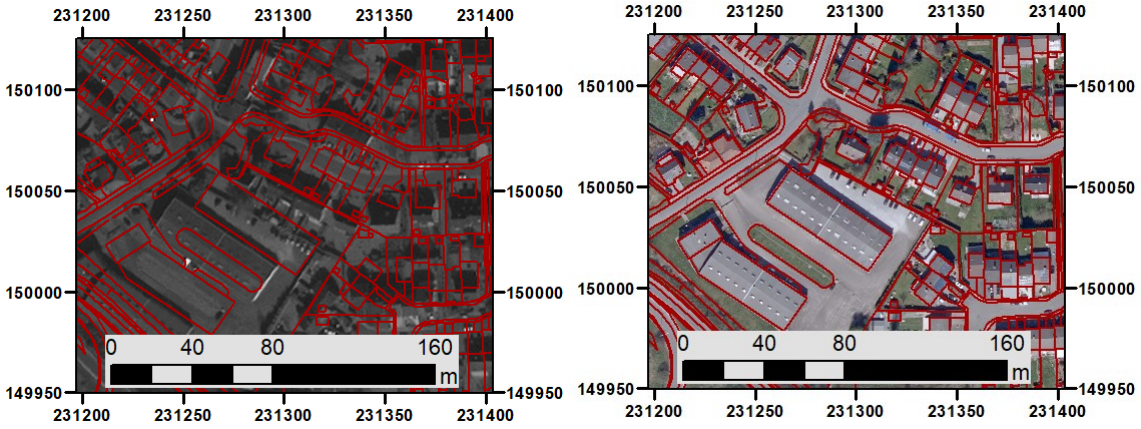

Figure 65: North-east shift of Pleiades orthoimage in the Northern part of the study area (left) and perfect spatial correspondence (right)between Vexcel orthomosaïc and PICC data at the same location

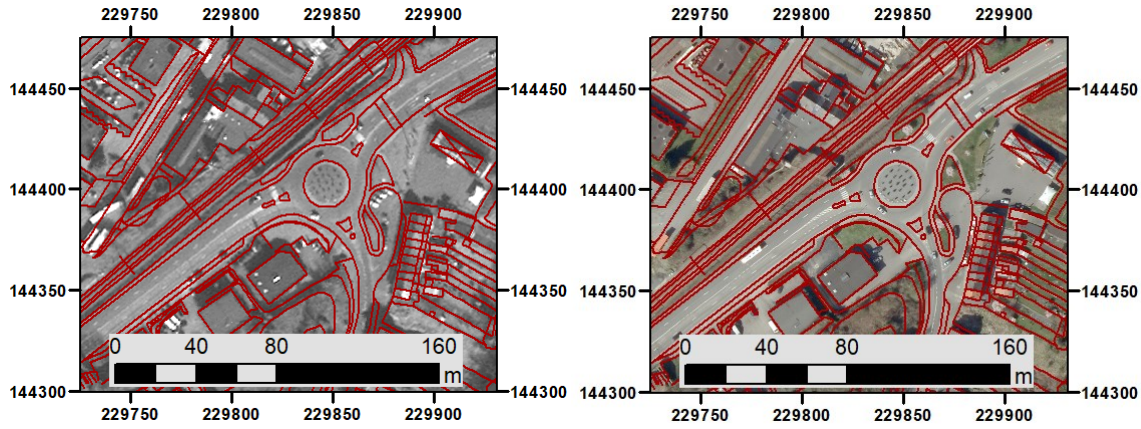

Figure 66: Perfect spatial correspondance between Pleiades orthoimage (left) and Vexcel orthomosaïc (right) with respect to PICC data in the Central part of the studied area

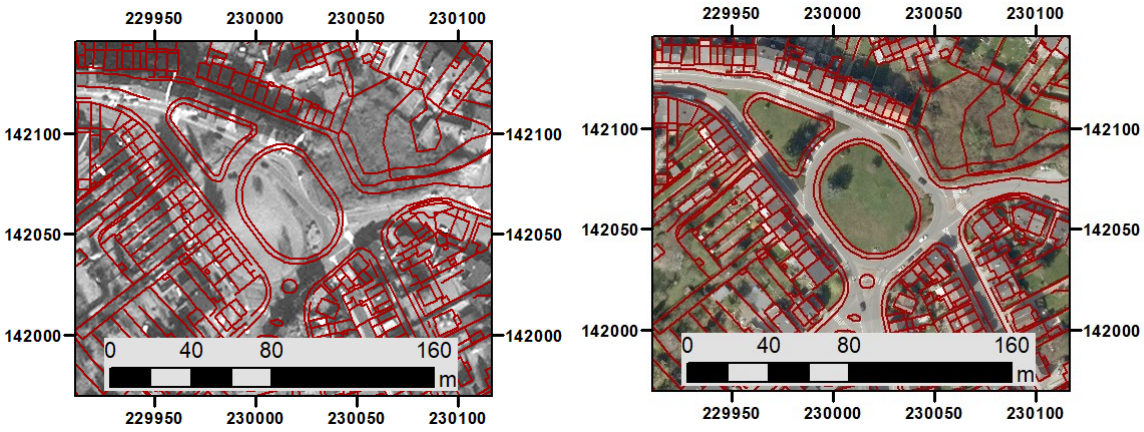

Figure 67: North-east shifted Pleiades orthoimage in the Southern part of the studied area(left) and perfect spatial correspondence (right) between Vexcel orthomosaïc and PICC data at the same location.

V.5. Radiometric analysis of Vexcel orthomosaïc

Radiometric imperfections were observed inside every tile (8 image files' pyramids automatically created by MICMAC for visualization of orthomosaïc of aerial images) as seen on examples of figure 68. This constitutes a weakness of MICMAC in mosaicking orthoimages of a block of images.

Figure 68: radiometric artefacts. From left to right: tile_0_0, tile_1_0, tile_2_0.

V.6. Final discussion

V.6.1. Hypothesis and aims reminders

This study aimed at assessing geometric quality of DEMs products from high spatial resolution satellites stereo-photogrammetry in comparison with those from aerial stereo-photogrammetry, with hypothesis that geometric accuracy of DSM and orthomosaïcs products generated from stereo-pair of Pleiades is equivalent to products from aerial UltraCam Falcon camera and that their structural richness describing 3D geometry of build-up area is similar. Quality was assessed through comparison of photogrammetric products themselves and their comparison with reference data sources.

V.6.2. Validation of hypothesis

During this research, photogrammetric products were generated from processed panchromatic Pleiades' stereo pair and pan-sharpened multispectral aerial stereoimages using bundle adjustment based on GNSS surveyed GCPs.

Using MICMAC, 3D bundles were reconstructed. Pleiades and Vexcel were respectively produced at reprojection errors of 0.309 pixel (~15.4 cm) and 0.346 pixel (~8.6 cm). Altimetric errors of Pleiades ranges from about -2 m to 6 m while for Vexcel, they are within - and + 1m. From the evaluation of quality of MICMAC's bundle adjustments, Vexcel's elevations were generally overestimated while Pleiades' elevations were underestimated as found on figure 35, table 6 , figure 36 and table 7.

Tie points detected on less than a half image (5000*5000 pixels) of original aerial images (each of 17 310 * 11 310 pixels) due to limited computer resources obviously participated in deterioration of quality of 3D reconstruction of the model and reduced altimetric accuracy. But also, low B/H ratio (0.27) of Vexcel images reduced altimetric accuracy because the latter is inversely proportional to this ratio see formula (6).

Pleaides reconstruction error was influenced by lack of tristereo pair, which should have corrected the overestimation found on Western sides of high-rise buildings. Quality of GCPs used, precisely, that of roundabouts centre points dramatically deteriorated Pleiades' DSM quality but also, this quality was affected by imprecise image measurements of GCPs associated to 50 cm of spatial resolution of Pleiades' stereopair.

The use of exactly same GCPs in aerial and satellite processing with MICMAC was impossible due to their respective 25 cm GSD difference; for instance, for GCPs taken as corners of high contrasted crosswalks visible on both datasets, their image positions on Pleiades stereo pair were manually hard to precise. In addition to that, GCPs' image measurements on converted 8bit images of corresponding 16bit original stereopair of Pleiades improved slightly the visibility to accurately carry out these measurements.

Even if we tried to respect the recommended GCPs distribution of figure 22 (right), we lacked surveyed ground points in upper and lower borders of the studied area as seen on figure 23, figure 35 and figure 36. By trying to maintain similar GCPs' distribution during Vexcel and Pleaides photogrammetric processing, we expected to introduce same errors (or effects) in resultant photogrammetric outputs, but Vexcel and Pleiades products were differently affected. In fact, Vexcel seemed to be slightly affected (or not affected at all) while Pleiades accuracy was highly deteriorated as the adjusted RPC still presented a geometric shift. This explains the obtained Pleiades' non-zero transverse parallax mean of 0.14 pixels from StatIm tool (in section RPCs' refinement). Consequently, Northern and Southern part of Pleiades DSM and orthomosaïc (see section V.4) were planimetrically shifted in North-East direction with respect to Vexcel and to reference datasets as developed below.

Comparison between photogrammetric products themselves and with reference data showed small elevation differences in urban structures areas and high differences in deciduous forested areas due to canopy cover differences associated to their acquisition season period (Pleiades acquired on 13th March and Vexcel on 12th -15th April 2015). Overestimation of Pleiades elevation was detected on Western edges of high rise buildings. This is due to satellites' position vector (orientation and elevation). Low sun-elevation angles are also responsible for long shadows during stereo pair acquisition with some implications in DSM quality due to matching imperfections in such context.

Comparison with PICC data proved (table 8) that neither level points, roads' axes points nor building points' errors are normally distributed. However, Vexcel rather than Pleiades showed small errors with respect to PICC data both planimetrically as proved in section V.4 and altimetrically as seen in table 8.

Comparison with Lidar data revealed that both Vexcel and Pleiades elevations are positively and strongly correlated (figure 55 and figure 64) with Lidar altitude. However, the existence of few high maximum and minimum elevation residuals of points located in deciduous forest

areas of canopy cover differences between each DSM and Lidar DSM resulted into points far from regression line.

Pleiades DSM are noisier than Vexcel as proved by either their respective hillshades (figure 47) or their comparison with hillshaded Lidar DSM (figure 52 and figure 53).

Radiometrically, Vexcel has inconsistency inside tiles of Orthomosaïc (figure 68) while Pleiades is darkened in the Northern part of the area of interest (figure 32).

From findings above, photogrammetry products of Vexcel are not equivalent to those of Pleiades. Based on fact that Pleiades DSM is noisier than Vexcel DSM and that slight elevation differences found in urban areas were far to be considered negligible, structural richness of Pleiades is not the same as that of Vexcel.

Without considering time required for field work, processing time of Pleiades can be estimated to maximum a week and that of aerial images to maximum three weeks for a user familiar with MICMAC. However, this can be even more than two months if the user is neophyte in MICMAC handling.

V.6.3. Transposition of the experiment in Rwanda

Carrying the same reconnaissance in Rwanda requires to be careful in GCPs selection especially if the images cover rural areas in which there are farmlands and no paved roads. In that particular case, GCPs can be selected around commercial centres as possible stable features around or fix some permanent marks visible and localisable without any ambiguity on the images (1 m cross with 10 cm width white branches on dark background). For the areas like Kigali this problem will not arise as most of the roads are paved with well-identified crosswalks. So, with RTK surveying using Rwanda Continuously Operating Reference Stations (CORS), the identified GCPs can be measured.

During reconnaissance, many GCPs should be selected on both aerial and satellite images. Their precise visibility in MICMAC's Elise window should be verified particularly for Pleiades satellite images before carrying out field work.

Rwanda is a country of thousand high hills therefore, tristereo satellite images are required to overcome occlusions effects and preferable tristereo pairs should be those acquired at one or two hours before noon or afternoon when the sun is at a small deviation with respect to zenith. Contrary to figure 16, in equatorial regions, flight mission for photogrammetric application has

to be done at the same day time; one or two hours (from 10 up to 11 am) before noon or after noon (from 1 to 2 pm) to ensure ideal sun elevation. In Rwanda, acquisition can be done throughout the year but the period from June up to August is ideal to ensure cloud free sky for optimal image acquisition. If available ASTRIUM archived images (http://www.intelligence-airbusds.com/en/4871-browse-and-order) have to be used, only tristereo Pleiades images with no clouds have to be chosen. Aerial flight mission has to be taken with digital cameras at nadir in previously specified period and daytime.

To avoid canopy cover difference effects, datasets acquired at the same date or month should be used. GCPs and CPs should be surveyed by ensuring evenly distributed GCPs and CPs particularly to cover image block corners as on figure 22 (right). These final remarks are common for accurate photogrammetric products from satellite and aerial images acquired not only in Rwanda but also in other countries.

CHAPTER VI. CONCLUSIONS

This chapter concludes our research and is mainly fed by results 'analysis, their discussions and verification of a priori hypothesis. It also suggests recommendations for future improvements.

The research's objective was to assess geometric quality of DSMs and orthomosaïc products from high spatial resolution aerial and Pleaides satellites stereo-photogrammetry. To be able to verify the hypothesis stated that photogrammetric products from Vexcel and Pleiades images were equivalent in both geometric and radiometric quality and that their structural realism and consistency in urban areas is similar, we used available datasets such as 48 aerial stereo images given by Walloon public services taken by a digital camera of Vexcel UltraCam Falcon cameras in a period from 12th to 15th April 2015 (see annex I) and an archived stereo pair of Pleiades of the same area taken on 13th March 2015.

Using GNSS surveyed GCPs, aerial and satellites images were processed. To deal with differences in details perception between Vexcel and Pleiades, GCPs corresponding to roundabouts centres were also surveyed and mainly used in Pleiades processing. However, their inaccurate and imprecise image measurements deteriorated the quality of 3D surface model extracted from Pleiades stereopair.

The limited capacity of computer used in processing aerial images allowed tie points computation of maximum image width of 5 000 instead of full resolution image of 17 310 height and 11 310 widths. This has dramatically reduced the accuracy of 3D reconstruction and obviously reduced photogrammetric products' accuracy as quality of image orientation depends on quality of tie points and quality of resulted DSM depends on quality of orientation and of used GCPs.

It has been found that the failure of fulfilling recommended GCPs configuration illustrated on figure 22 due to the lack of sufficient GCPs in Northern, Southern borders and in corners of images' block and of satellites' stereopair has reduced the accuracy of DSMs and orthoimages of Vexcel and Pleiades as shown by CPs' altimetric and planimetric errors illustrated by figure 35 and figure 36. Consequently, the accuracy of Pleiades' bundle adjustment outputs was degraded and produced a North-East shift of Pleiades photogrammetric products in Northern and Southern parts as detailed in sectionV.4. Thus, only Vexcel orthomosaïc geometrically fits with PICC data in planimetry.

Neither Vexcel nor Pleiades' bundle adjustments results show correlation between altimetric and planimetric errors (figure 35 and figure 36).

From the comparison between DSMs and orthomosaïc produced from Vexcel and Pleiades, the impact of using data taken in different seasons were highlighted by high elevation differences in deciduous forests zones whose canopy density varies differently on both products. This was also proved by comparison of these products with Lidar measurements. As seen on figure 25, in forests areas, few tie points were detected. This obviously causes uncertainty of dense matching in such areas. In coniferous forests, grass lands, bare soils and in urban cover areas, elevation differences between Vexcel and Pleiades were small but not negligible as they were in range of about – and + 2 m.

In our study area which has urban zones with high rise buildings, satellites looking directions – too large incidence angle and Eastern sector azimuths of both satellite images of the used stereopair – and too small sun elevation angle during images acquisition were found to be the source of occlusions and long shadows. Observation direction (SW and NW) of satellites caused the elevation overestimation of Pleiades in areas laying on Western sides of high rise buildings.

Based on significantly smaller altimetric errors found on Vexcel DSM rather than Pleiades in PICC and Lidar comparative analysis, Vexcel DSM was qualified as the best product. Structural richness of Vexcel and Pleiades DSMs is also different, with good promising on Vexcel. Thus, this research has demonstrated that Pleiades stereopair is not geometrically as accurate as aerial images taken by Vexcel UltraCam Falcon camera.

The above findings should be confirmed by using datasets having same spatial resolution and taken in the same period of the year and at same daytime in order to overcome differences in canopy cover of deciduous forests and their aspect due to illumination differences, by using GCPs in a strong configuration and carefully selected, by avoiding the use of roundabouts centres estimated from surrounded surveyed points and by using the improved computer capacity to ensure computation of tie points on resolution of the entire heavy aerial images if MICMAC software is used in photogrammetry processing. It would also be useful to take advantages of more GCPs and CPs and to keep them similar on both Vexcel and Pleiades to strengthen analysis.

REFERENCES

1. Abdel-Hakim, E. A. & Farag, A.A. (2006). CSIFT: A sift descriptor with color invariant characteristics. In Computer Vision and Pattern Recognition, 2006 IEEE Computer Society Conference ,2,1978-1983. http://www.vision.cs.chubu.ac.jp/CV-R/pdf/AlaaCVPR2006.pdf

2. Aggarwal, S. (n.d). Earth resource satellites. Satellite Remote Sensing and GIS Applications in Agricultural Meteorology, 39-65. http://www.wamis.org/agm/pubs/agm8/Paper-3.pdf

3. Agrafiotis, P. & Geogopoulos, A. (2015). Comparative assessment of very high resolution satellite and aerial orthoimagery. International archives of the Photogrammetry, Remote Sensing and Spatial Information Sciences, 40,1-7. http://dx.doi.org/10.5194/isprsarchives-XL-3-W2-1-2015

4. Airbus Defense and Space, (2017). Pléiades Satellite Imagery. http://www.intelligence-airbusds.com/pleiades/ . (lastly visited on 12th March 2017)

5. Astrium (2012). Pléiades imagery user guide, V2.0. http://www.intelligence-airbusds.com/pleiades/ first read on 24th November 2016.

6. Bartoli, A. (2003) Reconstruction et alignement en vision 3D : points, droites, plans et caméras. Interface homme-machine [cs.HC]. Institut National Polytechnique de Grenoble - INPG, 2003.HAL,2004. https://tel.archives-ouvertes.fr/tel-00004360

7. Baumann, R. P. (2009). History of remote sensing, satellite imagery, part II. https://www.oneonta.edu/faculty/baumanpr/geosat2/RS%20History%20II/RS-History-Part-2.html. Read on 20th February 2017

8. Bay, H., Tuytelaars, T. & Van Gool, L. (2006). SURF: Speeded Up Robust Features. In Leonardis A., Bischof H. & Pinz A. (eds), Computer Vision – ECCV 2006. Berlin: Springer, Lecture notes in computer science, 3951, 404–417. http://dx.doi.org/10.1007/11744023_32

9. Billen, R. & Cornélis, B. (2000). Géométrie de la spatiocarte : correction et validation. Bulletin de la Société Géographique de Liège, 38, 25-42.

10. Canada Centre for remote sensing. (n.d).Fundamental of remote sensing. http://sesremo.eu/downloads/teaching-material/gis-course_itc/ebooks/Fundamentals%20of%20Remote%20Sensing.pdf

11. Collignon, A (2008-2009). Notions de photogrammmetry. Leçon_02. 70p

12. Coulter, L. L. & Stow, A. D. (2008). Assessment of the spatial co-registration of multitemporal imagery from large format digital cameras in the context of detailed change detection. Sensors,8, 2161-2173.

13. D'Angelo, P. & Reinartz, P. (2012). DSM based orientation of large stereo satellite image blocks. International archives of the Photogrammetry, Remote Sensing and Spatial Information Science, 39-B1,209-214.

14. Dial, G. & Grodecki, J. (2005). RPC replacement camera models. In ASPRS 2005 Annual Conference "Geospatial Goes Global: From Your Neighborhood to the Whole Planet" March 7-11, 2005, Baltimore, Maryland.

15. Farag, A. A. & Abdel-Hakim, E. A. (2004). Detection, categorization and recognition of road designs for autonomous navigation. In Proceedings of Acivs 2004 (Advanced Concepts for Intelligent Vision Systems), Brussels, Belgium, 31st August-3rd September 2004,125-130.

16. Fowler, E. J. (2014). Compressive pushbroom and wiskbromm sensing for hyperspectral remote sensing imaging. http://dx.doi.org/10.1109/ICIP.2014.7025137

17. Förstner, W. & Wrobel, P. B. (2016). Photogrammetric computer vision-statistics, geometry, orientation and reconstruction, vol11. Switzerland: springer 2016,816p. http://dx.doi.org/10.1007/978-3-319-11550-4

18. Galland, O., Bertelsen, S.H., Guldstrand, L.G., Johannessen, F.B., Burchardt, S., Mair, K. (2016). Application of open-source photogrammetric software MicMac for monitoring surface deformation in laboratory models. In Journal of Geophysical Research: Solid Earth,121,1-21. http://dx.doi.org/10.1002/2015JB012564

19. Georgantas, A., Brédif, M. & Pierrot-Desseilligny, M. (2012). An Accuracy Assessment of Automated Photogrammetric Techniques for 3D Modeling of Complex Interiors. International Archives of the Photogrammetry, Remote Sensing and Spatial

Information Sciences, 39-B3,23-28. In XXII ISPRS Congress, 25 August – 01 September 2012, Melbourne, Australia.

20. Gomarasca, A.M. (2009). Basics of Geomatics. Italy: Springer, 656p. http://danida.vnu.edu.vn/cpis/files/Books/Basics%20of%20Geomatics.pdf

21. Govender, N. (2009). Evaluation of feature detection algorithms for structure from motion. In 3rd Robotics and Mechatronics Symposium (ROBMECH 2009). Pretoria, South Africa, 8-10 November 2009,4p. http://hdl.handle.net/10204/3855

22. Grodecki, J. & Dial, G. (2003). Block adjustment of High-Resolution Satellite Images Described by Rational Polynomials. Photogrammetric Engineering & Remote Sensing, 69, 59– 68.

23. Gruber, M, & Leberl, F. (2007). About Frame versus Pushbroom Aerial cameras. A Microsoft Photogrammetry Technical Report, 1-36. https://pure.tugraz.at/portal/files/1450315/289A%2520-%2520UltraCam%2520Microsoft-TechReport%2520on FAQ,%25202007.pdf

24. Gupta, R. & Hartley, I.R. (1995). Camera estimation for orbiting pushbrooms. http://users.rsise.anu.edu.au/hartley/public_html/Papers/pushbroom/ACCV/paper.pdf

25. Gupta, R. & Hartley, I.R. (1997). Linear pushbroom cameras. http://citeseerx.ist.psu.edu/viewdoc/download?doi=10.1.1.72.124&rep=rep1&type=pdf

26. Gupta, R. & Hartley, I.R. (n.d). Camera estimation for orbiting pushbroom imaging systems. http://citeseerx.ist.psu.edu/viewdoc/download?doi=10.1.1.5.3724&rep=rep1&type=pdf

27. Hasegawa, H., Matsuo, K., Koarai, M., Watanabe, N., Masaharu, H., & Fukushima, Y. (2000). DEM accuracy and the Base to Height (B/H) ratio of Stereo Images. In International Archives of Photogrammetry and Remote Sensing, XXXIII -part B4,356-359.

28. Hexagon geospatial. (2017). Photogrammetric concepts. https://hexagongeospatial.fluidtopics.net/#/reader/uOKHREQkd_XR9iPo9Y_Ijw/dOgfaa0UyXt3p6dFHUQocw (lastly visited on 15th April 2017).

29. Hu, F., Gao, M.X., Li, Y.G., Li, M. (2016). DEM extraction from Worldview-3 stereo-images and accuracy evaluation. In International Archives of Photogrammetry and

Remote Sensing, XXIII ISPRS Congress, 12–19 July 2016, Prague,327-333. http://dx.doi.org/10.5194/isprsarchives-XLI-B1-327-2016

30. Hu, Y., Tao, V. & Croitoru, A. (n.d). Understanding the rational function model: methods and applications. http://www.isprs.org/proceedings/XXXV/congress/comm4/papers/423.pdf

31. Jacobsen, K. (2007). Orientation of high resolution optical space images. In ASPRS annual conference, May 7-11, 2007, Tampa, Florida.

32. Jacobsen, K., Baltsavias, E. & Holland, D. (2008). Tutorial 10: Information extraction from high resolution optical satellite sensors. In XXIst ISPRS Congress, July 3rd, 2008, Beijing, China

33. JARS, (n.d). Plateforms. 94-119. http://www.jars1974.net/pdf/06_Chapter05.pdf

34. Jedlička, K. (2009). Accuracy of surface models acquired from different sources — important information for geomorphological research. Geomorphologia slovaca et bohemica,17-28. http://www.asg.sav.sk/gfsb/v091/gfsb090102.pdf .

35. Karabork, H., Yildiz, K. & Coskun, E. (2012). Object recognition for interior orientation in digital photogrammetry. In ISPRS proceedings: XXXV congress. http://www.isprs.org/proceedings/XXXV/congress/comm3/papers/380.pdf .

36. Kheiri, M. (2006). Digital Aerial Cameras. International archives of the Photogrammetry, Remote Sensing and Spatial Information Science. International Archives of the Photogrammetry, Remote Sensing and Spatial Information Science, 36-Part 6,229-234.

37. Kiema Kyalo, J. B. & Awange, J. L. (2013). Digital photogrammetry. In Allan, R., Förstner, U. & Salomons, W.(eds), Environmental Geoinformatics, Environmental Science and Engineering. London: Springer. 175p. http://dx.doi.org/10.1007/978-3-642-34085-7_12

38. Kraus, K. & Waldhäusl, P. (1998). Manuel de photogrammetrie : Principe et procédés fondamentaux. Paris : Hermes ,407p.

39. Leberl, F. & Gruber, M. (2003). Flying the new large format digital aerial camera ultracam. *Photogrammetric week,3,67-76.* In Dieter Fritsch (Ed.). http://www.ifp.uni-stuttgart.de/publications/phowo03/guber.pdf

40. Linder, W. (2009). *Digital photogrammetry: A practical course*, 3rd ed. Berlin: Springer,220p. http://dx.doi.org/10.1007/978-3-540-92725-9

41. Lowe, D.G. (1999). Object Recognition from Local Scale-Invariant Features. *In Proceedings of the International Conference on Computer Vision*, Corfu, Greece, September 1999, 1150–1157.

42. Lowe, D. G. (2004), Distinctive image features from scale-invariant keypoints. *International Journal of Computer Vision*. 60(2), 91–110.

43. Luhmann, T. (2004). A historical review on panorama photogrammetry. *In ISPRS proceedings /XXXIV/5-16.*

44. Microsoft UltraCam Team. (2012). UltraCam-White-Paper-The-New-Standard-of-Excellence-for-Aerial-Mapping. http://www.vexcel-imaging.com (lastly visited on 5thMay 2017)

45. Mikolajczyk, K. & Schmid, C. (2005). A performance evaluation of Local Descriptors. *IEEE transactions on pattern analysis and machine intelligence*, 27, October 2005,1615-1630.

46. Morel, J.-M. & Yu, G. (2009). ASIFT: A new framework for fully affine invariant image comparison. *Society for industrial and applied mathematics journal on imaging Sciences*, 2(2), 438–469. https://doi.org/10.1137/080732730

47. Moutinho, O'. (2015). *Evaluation of photogrammetric Solutions for RPAS: Commercial VS Open source*. Dissertation for master's degree, University of Porto, Inedit, 121p. http://hdl.handle.net/10216/82382

48. Neumann, J. K. (2009). Digital Aerial cameras. http://icaci.org/files/documents/ICC_proceedings/ICC2009/html/nonref/1_6.pdf (lastly visited on 4th June 2017)

49. NGA. (2009). NGA standardization document: pushbroom/whiskbroom sensor model metadata profile, supporting precise geopositioning,version1. http://www.gwg.nga.mil/documents/csmwg/PUSHBROOM_WHISKBROOM_PAPER_Version_1_0_GOLD_21JUL09.doc Read 26th May 2017

50. Nicolas, J. M. (2012). Les bases de l'imagerie satellitaire. Telecom ParisTech, 128 p. http://perso.telecom-paristech.fr/~almansa/MVA/biblio/polysatel_TelecomParisTech_2012.pdf

51. Pierrot-Deseilligny, M. (2017). *MicMac, Apero, Pastis and Other Beverages in a Nutshell*. https://github.com/micmacIGN/Documentation/blob/master/DocMicMac.pdf

52. Pierrot-Deseilligny, M. & Clery, I. (2011). Apero, an open source bundle adjustment software for automatic calibration and orientation of set of images. *International archives of the photogrammetry, remote sensing and spatial information sciences,* 38-5/W16,269-276. *In XXII ISPRS congress*, 25 August – 01 September 2012, Melbourne, Australia.

53. Poli, D. (2005). Modelling of spaceborne linear array sensors. Doctoral thesis, Zurich, Swiss federal institute of technology Zurich, edit, 204p. published by: Institute of Geodesy and Photogrammetry Swiss Federal Institute of Technology (ETH) CH-8093, Zurich.

54. Poli, D. & Caravaggi, I. (2013).3D modelling of large urban areas with stereo VHR satellite Imagery: lessons learned. International Society for the Prevention and Mitigation of Natural Hazards,68,53-78. http://dx.doi.org/10.1007/s11069-013-0583-4

55. Ramapriyan, H. K. (2001). Satellite imagery in earth science applications. In Castelli, V. & Bergman, L. D. (eds), *Image databases: search and retrieval of digital imagery*. New York: Wiley online library, 565p. http://dx.doi.org/10.1002/0471224634.ch3

56. Rupnik, E., Pierrot Deseilligny, M., Delorme, A. & Klinger, Y. (2016). Refined satellite image orientation in the free open-source photogrammetric tools Apero/Micmac. *ISPRS Annals of Photogrammetry, Remote Sensing and Spatial Information Sciences,8-1,83-90. In XXIII ISPRS Congress*, 12–19 July 2016, Prague, Czech Republic. http://dx.doi.org/10.5194/isprsannals-III-1-83-2016

57. Schenk, T. (2005). *Introduction to photogrammetry.* Ohio State University.95p

58. Shaker, A., Yan, Y. W. & Easa, S. (2010). Using Stereo Satellite Imagery for Topographic and Transportation Applications: An accuracy assessment. *GIScience & Remote Sensing*, 47, 321–337. http://dx.doi.org/10.2747/1548-1603.47.3.321

59. SPOT Image (2010). Preprocessing levels and location accuracy. https://spacedata.copernicus.eu/documents/12833/14537/SPOT-5_PreprocessingLevels.pdf

60. Tempelmann, U., Börner, A., Chaplin, B., Hinsken, L., Mykhalevych, B., Miller, S., Recke, U., Reulke, R., Uebbing, R. (2000). Photogrammetric software for the LH systems ADS40 airborne digital sensor**.** *International Archives of Photogrammetry and Remote Sensing*. 33,552-559.

61. Tihon, G., Cornet, Y., Drevesse, J., Binard, M., Peeters, C., Bastin, T. & Donnay, J.-P. (2005). DSM from SPOT5_HRS5 images: extraction and validation. *Proceedings of the EARSel workshop 3D_remote Sensing*, Porto, Portugal,10-11June 2005.

62. Toth, C. & Józ´ków, G. (2015). Remote sensing platforms and sensors: A survey. *International Society for Photogrammetry and Remote Sensing*, 22-36. https://doi.org/10.1016/j.isprsjprs.2015.10.004

63. Triggs, B., McLauchlan, P., Hartley, R., Fitzgibbon, A. (2010). Bundle adjustment – a modern synthesis. *International Workshop on Vision Algorithms,* September, 2000, Corfu, Greece. Springer-Verlag, 1883,298–372*, Lecture Notes in Computer Science; Vision Algorithms: Theory and Practice*. https://hal.inria.fr/inria-00548290

64. Vermeer, M. & Ayehu, T. G. (2014). Experiences with digital aerial photogrammetry software ‘e-foto’ in an educational setting in Bahir Dar,Ethiopia. In proceedings, third open source geospatial research & education symposium(OGRS),65-68, Espoo,Finland,10-13 June 2014.

65. Wiechert, A. and Gruber, M. (2015). UltraCam and Ultramap – an update. *Photogrammetric Week,15*,45-50. In Dieter Fritsch (Ed.). http://www.ifp.uni-stuttgart.de/publications/phowo15/050Wiechert.pdf

66. Yilmaz, A., Erdogan, M., Maras, H. H., Aktug, B. & Maras, S. S. (2016). Did satellite imagery supersede aerial imagery? a perspective from 3D geopositioning accuracy.

Arab Journal of Geosciences.
http://dx.doi.org/10.1007/s12517-016-2386-x

67. Zhou, Y., Parsons, B., John R Elliott, R. J., Barisin, I., & Walker, T. R. (2015). Assessing the ability of Pleiades stereo imagery to determine height changes in earthquakes: a case study for the El Mayor-Cucapah epicentral area. Journal of geophysical research: solid earth, 120, 8793-8808.
http://dx.doi.org/10.1002/2015JB012358

Web references:

http://www.intelligence-airbusds.com/en/4871-browse-and-order: Airbus Defense and Space, (2017). Pleiades archive. (lastly visited on 21th August 2017)

http://www.florianhillen.de/studium/projekt/index.php?id=grundlagen&uid=sensoren: Studien project. (lastly visited on 21st March 2017)

http://geoportail.wallonie.be/walonmap: Wallonia public service. (lastly visited on 10th April 2017)

https://ultracam.wordpress.com/page/7/: Skaw, J. (2013). UltraCam blog. (lastly visited on 5th May 2017)

http://www.vexcel-imaging.com:Vexcel imaging. (2016). Aerial products. (lastly visited on 5th May 2017)

ANNEXES

List of annexes

Annex A: Calibration certificate of Vexcel UltraCam Falcon camera used for production of the Wallonia orthoimage of 2015

Calibration Report

Camera:	**UltraCam Falcon, S/N UC-Fp-1-40616106-f100**
Manufacturer:	**Vexcel Imaging GmbH, A-8010 Graz, Austria**
Date of Calibration:	**Sep-24-2014**
Date of Report:	**Feb-12-2015**
Revision of Camera:	**Rev01.00**
Version of Report:	**V01**

Calibration Report

1) Geometric Calibration

Camera:	**UltraCam Falcon, S/N UC-Fp-1-40616106-f100**
Manufacturer:	**Vexcel Imaging GmbH, A-8010 Graz, Austria**
Panchromatic Camera:	**ck = 100.500mm**
Multispectral Camera:	**ck = 100.500mm**
Date of Calibration:	**Sep-24-2014**
Date of Report:	**Feb-12-2015**
Revision of Camera:	**Rev01.00**
Version of Report:	**V01**

2) Panchromatic Camera

Large Format Panchromatic Output Image

Image Format	long track	67.860mm	11310pixel
	cross track	103.860mm	17310pixel
Image Extent		(-33.93, -51.93)mm	(33.93, 51.93)mm
Pixel Size		6.000µm*6.000µm	
Focal Length	ck	100.500mm	± 0.002mm
Principal Point	X_ppa	0.000 mm	± 0.002mm
(Level 2)	Y_ppa	0.000 mm	± 0.002mm
Lens Distortion	Remaining Distortion less than 0.002mm		

3) Multispectral Camera

Medium Format Multispectral Output Image (Upscaled to panchromatic image format)

Image Format	long track	67.860mm	3770pixel
	cross track	103.860mm	5770pixel
Image Extent		(-33.93, -51.93)mm	(33.93, 51.93)mm
Pixel Size		18.000µm*18.000µm	
Focal Length	ck	100.500mm	
Principal Point	X_ppa	0.000 mm	± 0.002mm
(Level 2)	Y_ppa	0.000 mm	± 0.002mm
Lens Distortion	Remaining Distortion less than 0.002mm		

Full Pan Image, Residual Error Diagram

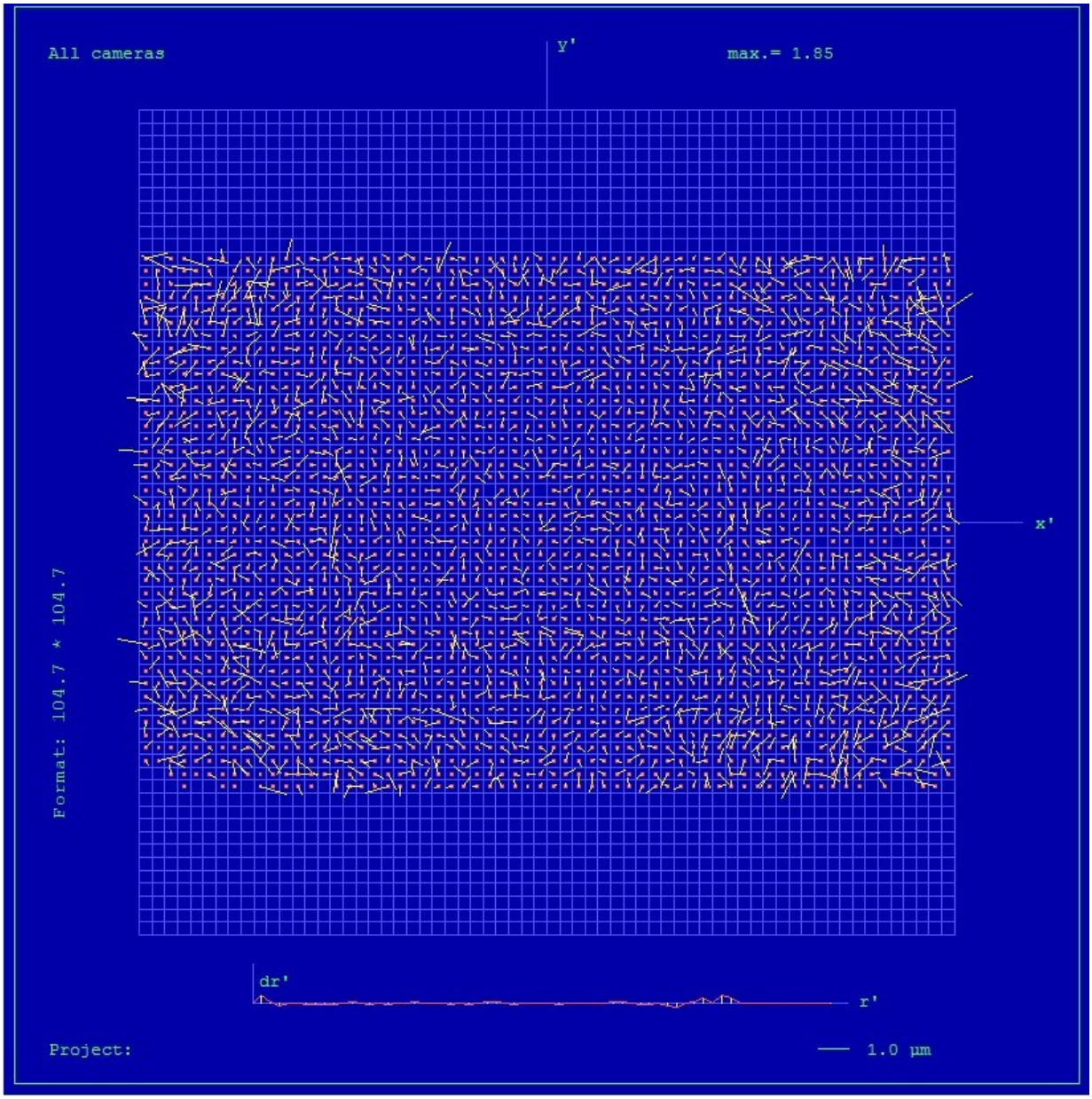

Residual Error (RMS): 0.95 µm

Explanations:

1) Calibration Method:

The geometric calibration is based on a set of 84 images of a defined geometry target with 394 GCPs.

Number of point measurements for the panchromatic camera :	18402
Number of point measurements for the multispectral camera :	72672

Determination of the image parameters by Least Squares Adjustment.

Software used for the adjustment: BINGO (GIP Eng. Aalen, Germany)

2) Level 2 Image Coordinate System:

PAN 17310 pixel by 11310 pixel
MS 5770 pixel by 3770 pixel

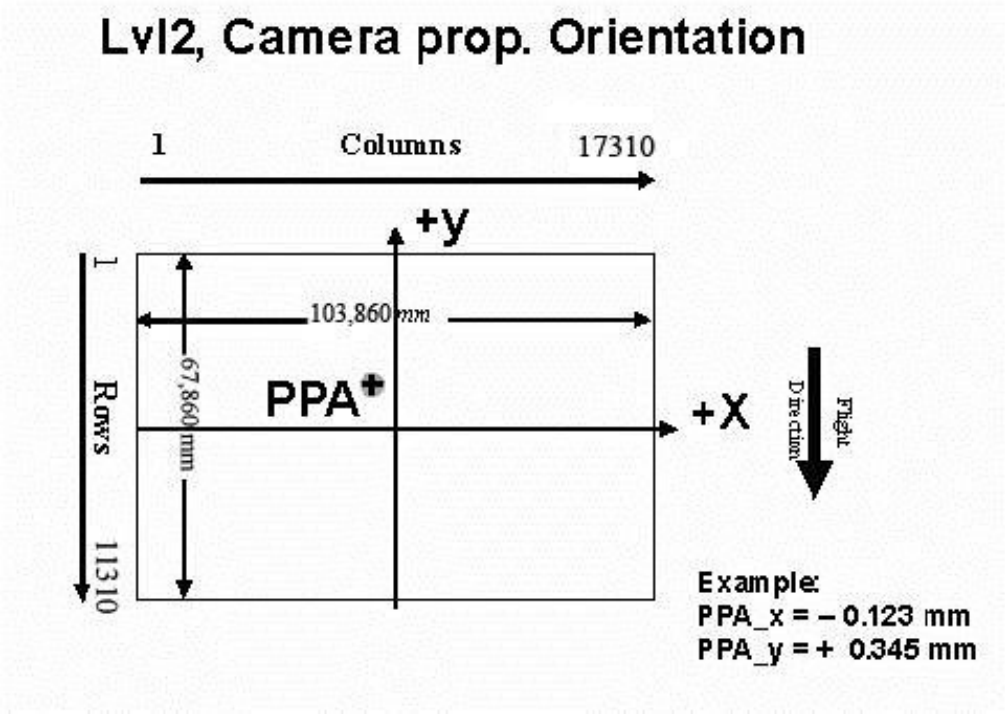

The image coordinate system of the Level 2 images is shown in the above figure. The level 2 image consists of 17310 columns and 11310 rows, which leads to a total image format of 103.860 x 67.860 mm. The coordinate of the principal point in the level 2 image is given on page 3 of this report. The above figure shows the position of an example principal point at the coordinate (-0.123 / 0.345).

3) Level 3 Image Coordinate System:

PAN 17310 pixel by 11310 pixel

(after rotation of 270° CW)

MS 5770 pixel by 3770 pixel

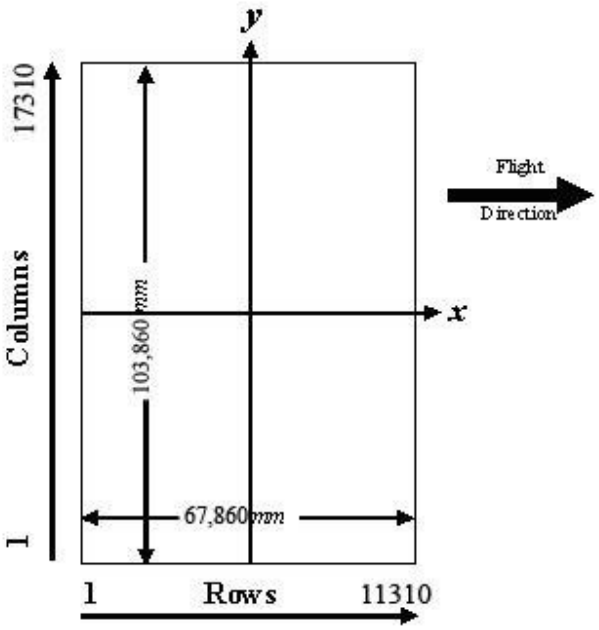

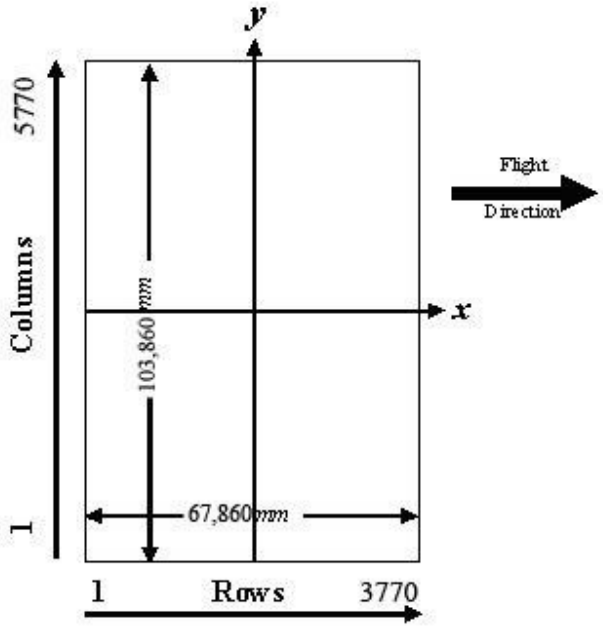

Panchromatic Image Format

Multispectral Image Format

==========

4) Position of Principal Point in Level 3 Image

The position of the principal point in the level 3 image depends on the “rotation” setting used in UltraMap during the pan-sharpening step. The exact position relative to the image center is given in the table below as a function of the rotation setting used in UltraMap. The coordinates are specified for clockwise (CW) rotation in steps of 90 degrees, according to the principal point coordinate given on page 3 for high- and low resolution images.

Image Format	Clockwise Rotation (Degree)	PPA	
		X	Y
Level 2	-	0.000	0.000
Level 3	0	0.000	0.000
Level 3	90	0.000	0.000
Level 3	180	0.000	0.000
Level 3	270	0.000	0.000

The coordinates in the figure below are only example values to illustrate the effect of image rotation on the principal point position, and do **not** correspond to the camera described in this report.

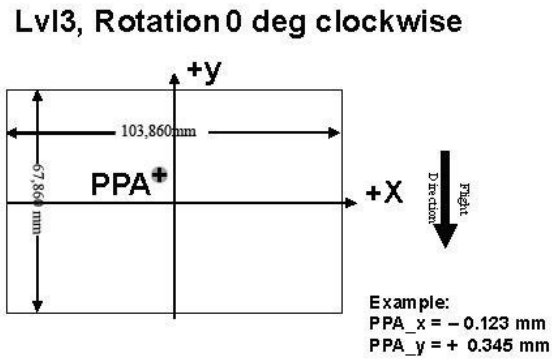

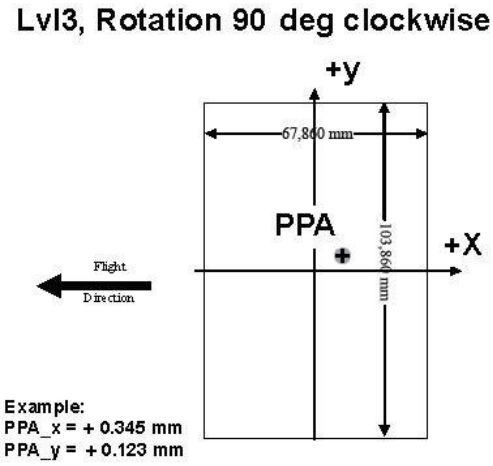

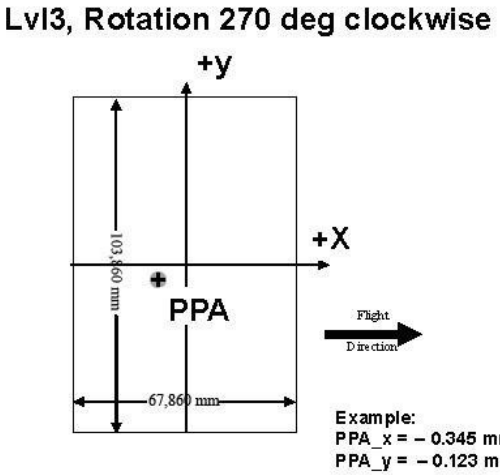

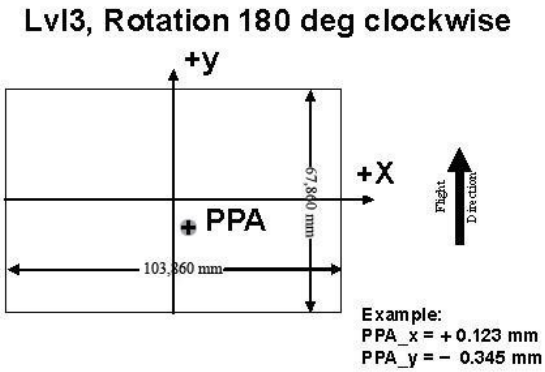

4) Lens Resolving Power

The following curves show the development of the modulation transfer function across different image heights of the panchromatic cones.

The curves are given for the meridonial (tangential) and sagital (radial) component of signals at frequencies of 10, 20, 40 and 80 line pairs per millimeter.

As the MTF is a function of the specific aperture size used, one set of curves is given for each aperture size.

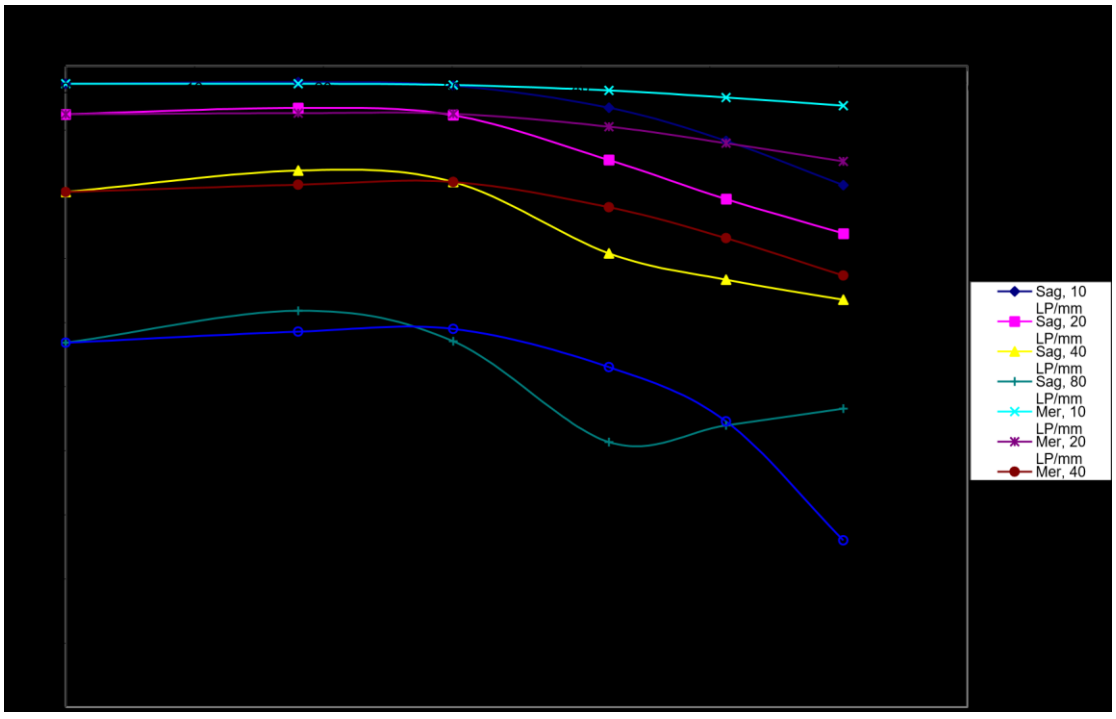

Modulation versus Image Height - Aperture f / 8

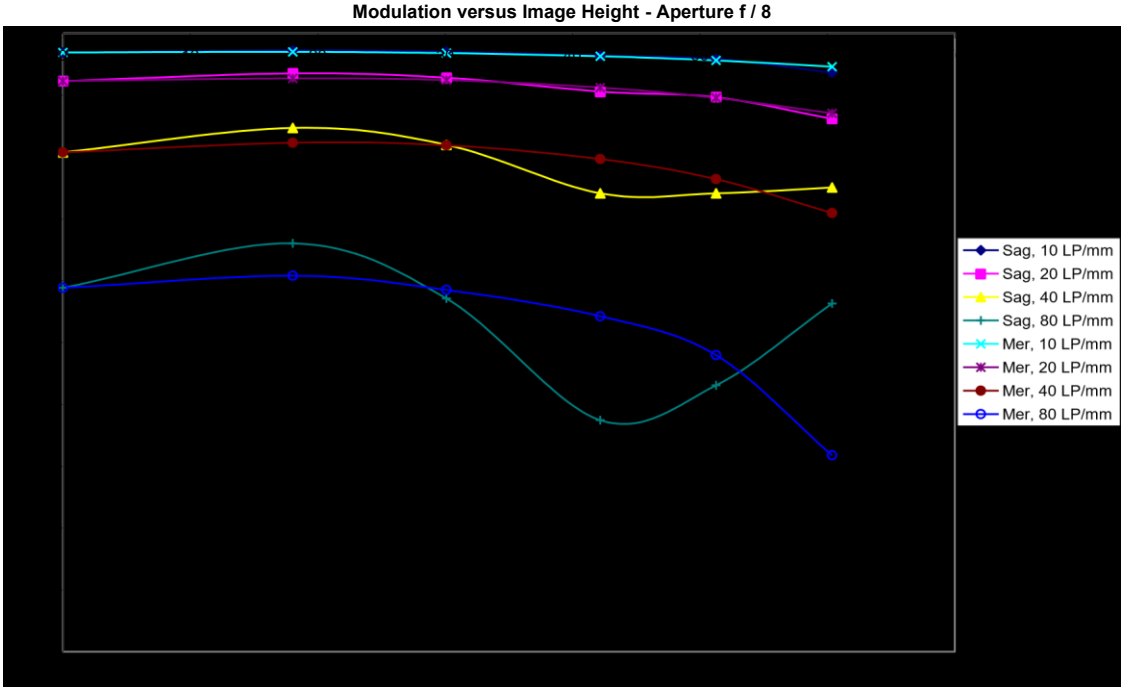

Modulation versus Image Height - Aperture f / 11

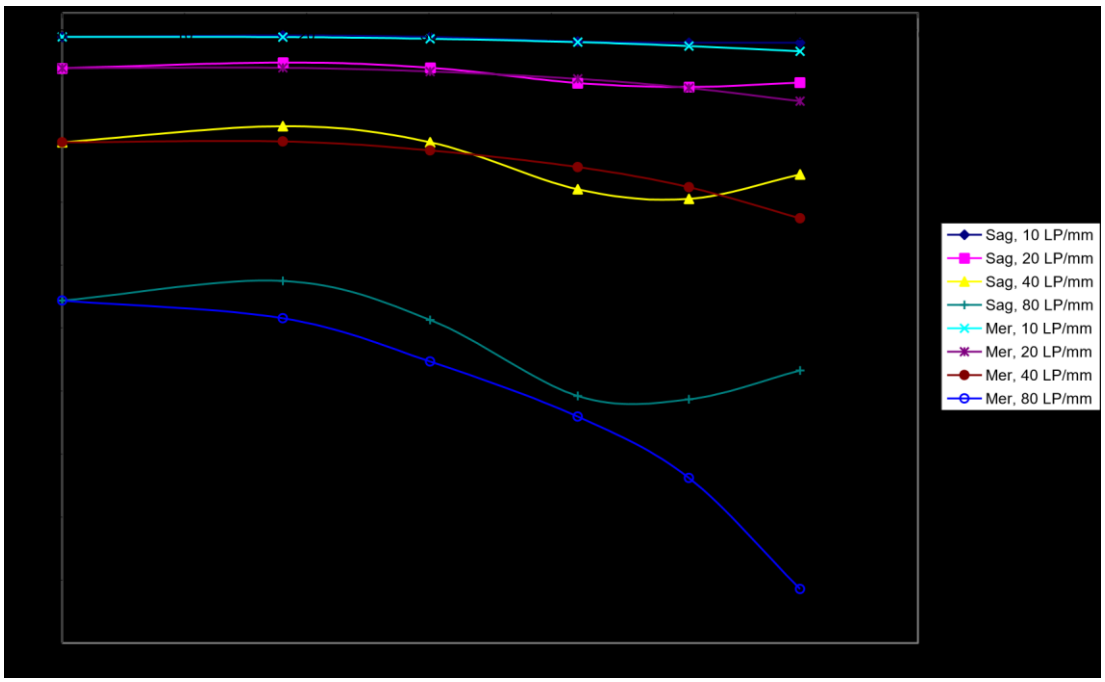

Modulation versus Image Height - Aperture f / 16

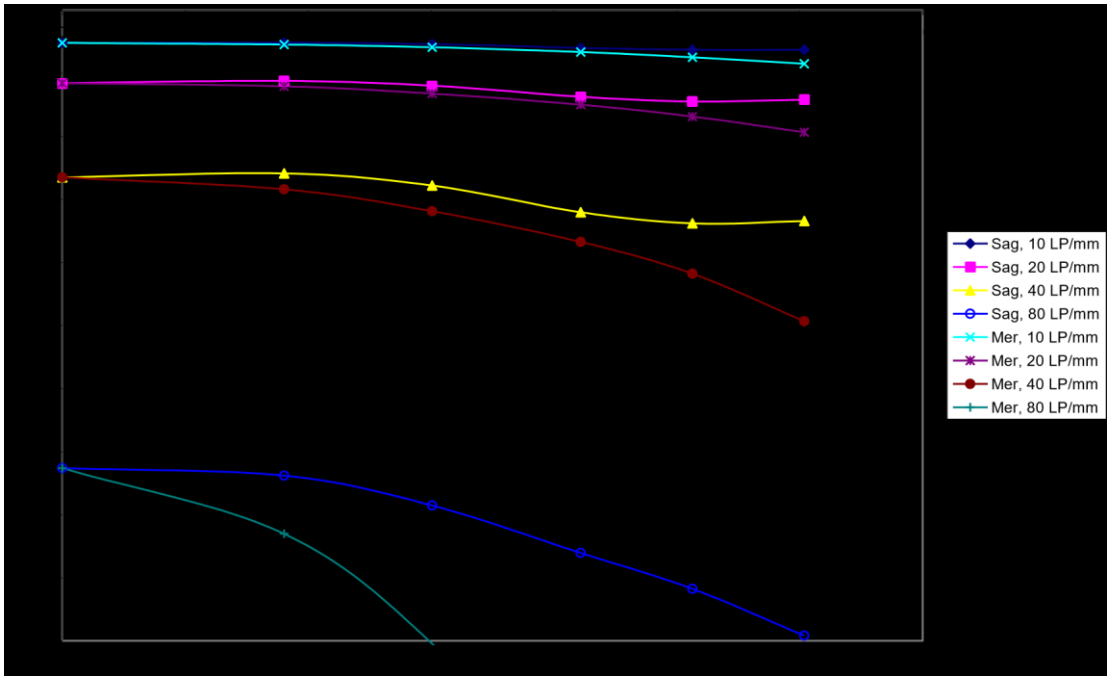

Modulation versus Image Height - Aperture f / 22

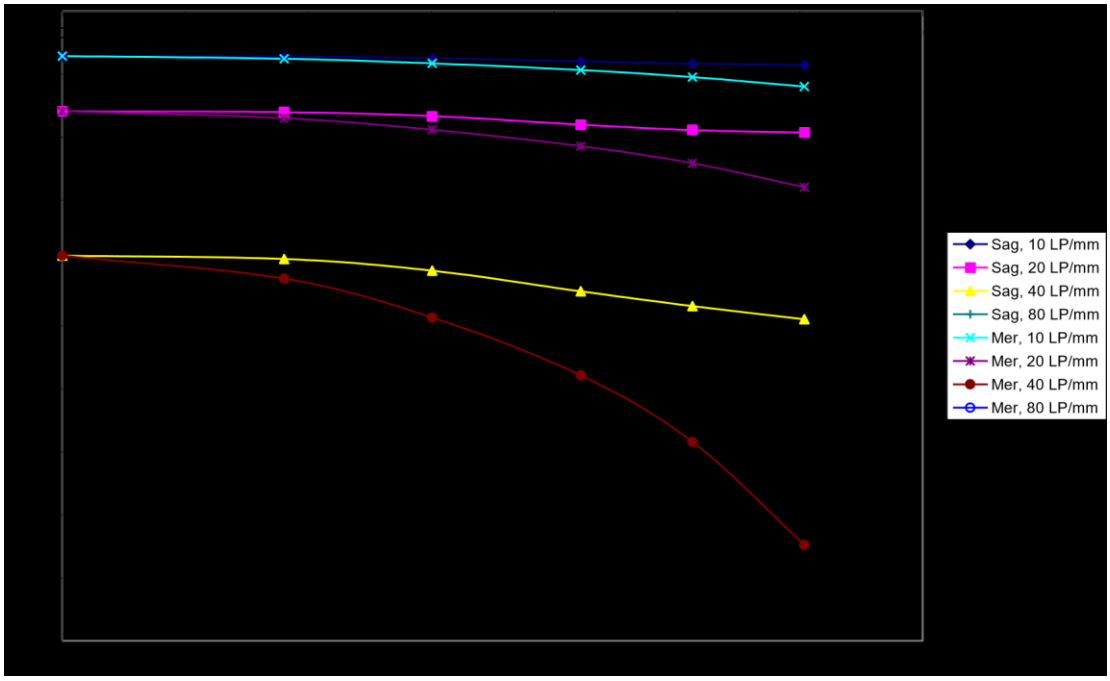

5) Spectral Sensitivity

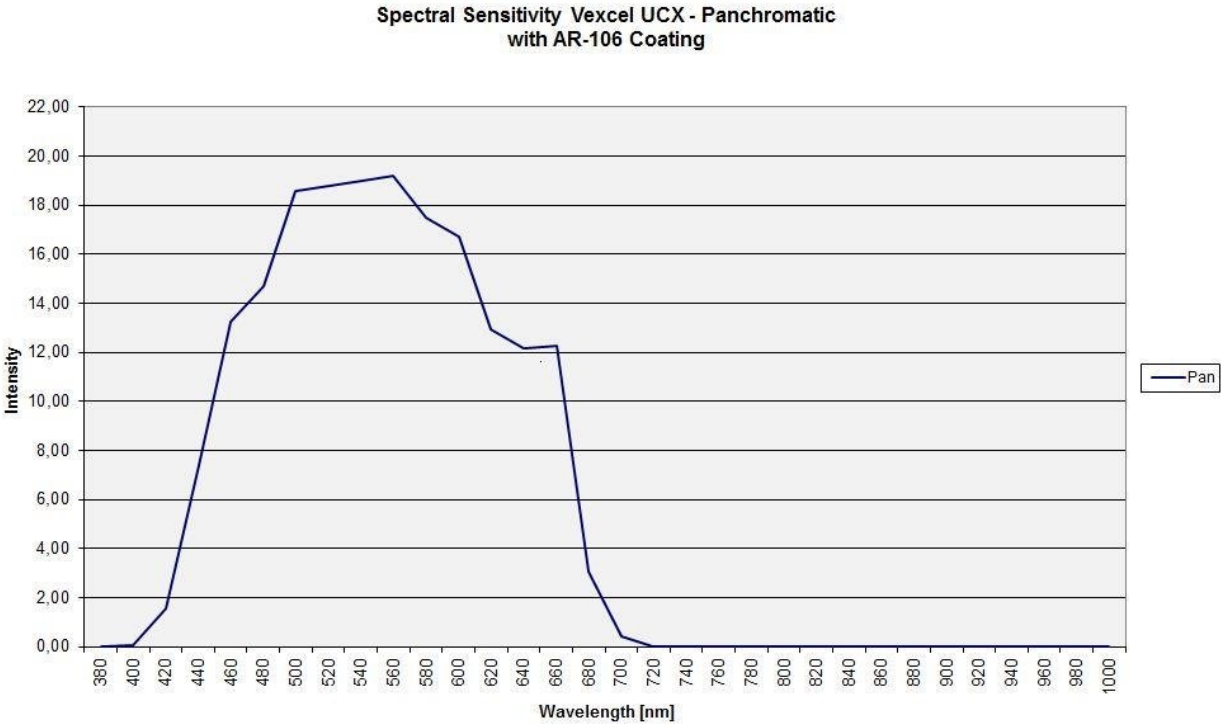

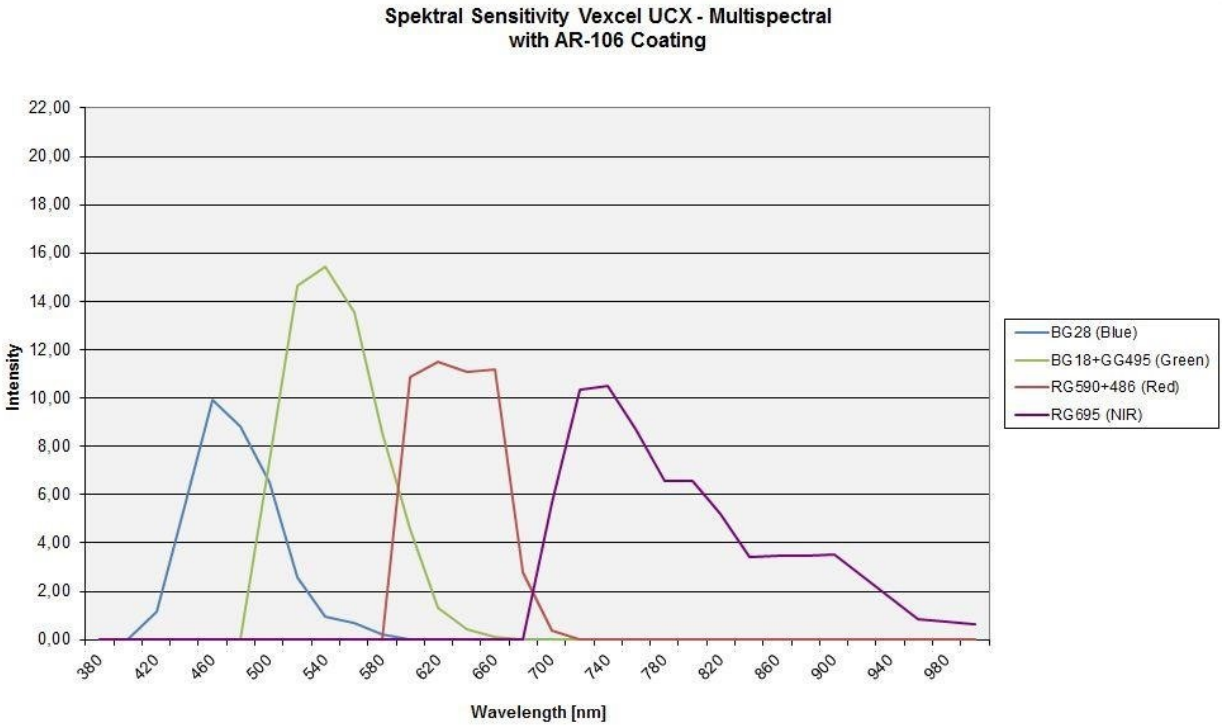

Calibration Report

Radiometric Calibration

Camera: **UltraCam Falcon, S/N UC-Fp-1-40616106-f100**

Manufacturer: **Vexcel Imaging GmbH, A-8010 Graz, Austria**

	PAN	R, G, NIR	B
Aperture	F5.6	F4.8	F4.0
	F6.7	F5.6	F4.0
	F8	F6.7	F4.8
	F9.5	F8	F5.6
	F11	F9.5	F6.7
	F13	F11	F8
	F16	F13	F9.5
	F22	F19	F13

Date of Calibration: **Sep-24-2014**
Date of Report: **Feb-12-2015**
Revision of Camera: **Rev01.00**
Version of Report: **V01**

Explanations:

Calibration Method:

The radiometric calibration is based on a series of 60 flat field images for each aperture size and sensor. The flat field is illuminated by eight normal light lamps with known spectral illumination curves.

These images are used to calculate the specific sensitivity of each pixel to compensate local as well as global variations in sensitivity. Sensitivity tables are calculated for each sensor and aperture setting, and applied during post processing from level 0 to level 1.

Outlier Pixels that do not have a linear behavior as described in the CCD specifications are marked as defective during the calibration procedure. These pixels are not used or only partially used during post processing and the information is restored by interpolation between the neighborhood pixels surrounding the defective pixels.

Certain pixels that are named Qmax pixels due to the fact that they can only store and transfer charge up to a certain maximum amount are detected in an additional calibration step. These pixels are treated differently during post processing, since their behavior can affect not only single pixel values but whole columns.

Calibration Report

Summary

Camera:	**UltraCam Falcon, S/N UC-Fp-1-40616106-f100**
Manufacturer:	**Vexcel Imaging GmbH, A-8010 Graz, Austria**
Date of Calibration:	**Sep-24-2014**
Date of Report:	**Feb-12-2015**
Revision of Camera:	**Rev01.00**
Version of Report:	**V01**

The following calibrations have been performed for the above mentioned digital aerial mapping camera:

- Geometric Calibration
- Verification of Lens Quality and Sensor Adjustment
- Radiometric Calibration
- Calibration of Defective Pixel Elements
- Shutter Calibration
- Sensor and Electronics Calibration

This equipment is operating fully within specification as defined by Vexcel Imaging GmbH.

Dr. Michael Gruber

Chief Scientist, Photogrammetry

Vexcel Imaging GmbH

Ing. Peter Prassl

Senior Calibration Engineer

Vexcel Imaging GmbH

Annex B: Metadata of Pleiades stereo-pair bought at Astrium for this research

Première image acquise	Deuxième image acquise
Identifiant	Identifiant
DS_PHR1A_201503131039220_FR1_PX_E005N50_0616_01426	DS_PHR1A_201503131039513_FR1_PX_E005N50_0616_01502
Description	Description
Pléiades DSP3 Archive	Pléiades DSP3 Archive
Date	Date
13 mars 2015 10:39:24	13 mars 2015 10:39:53
Angle d'incidence	Angle d'incidence
20.08922996181834° *I_global*	15.00061478767525° *I_global*
Angle d'incidence (Across Track)	Angle d'incidence (Across Track)
17.43105050896688° $I_{OrthoScan}$	13.46163648576237° $I_{OrthoScan}$
Angle d'incidence (Along Track)	Angle d'incidence (Along Track)
-10.62329682771709° I_{Scan}	6.867343556456544° I_{Scan}
Angle d'orientation	Angle d'orientation
179.9576550710607°	179.981863874832°
Angle de prise de vue	Angle de prise de vue
18.09985943507457° *o*	13.39951773794642° *o*
Angle de prise de vue (Across Track)	Angle de prise de vue (Across Track)
-13.57744929343182°	-12.96357865002741°
Angle de prise de vue (Along Track)	Angle de prise de vue (Along Track)
12.42018663517533°	-3.508709817038211°
Archive	Archive
Pléiades archive	Pléiades archive
Azimuth solaire	Azimuth solaire
158.9751479761348°	158.9756762742507°
Constellation	Constellation
Pleiades	Pleiades
Couvert neigeux	Couvert neigeux
0%	0%
Couvert nuageux	Couvert nuageux
0.003155%	0.7%
Elévation solaire	Elévation solaire
34.58692891581589°	34.58451725215483°

ID scène	ID scène
DS_PHR1A_201503131039220_FR1_PX_E005N50_0616_01426	DS_PHR1A_201503131039513_FR1_PX_E005N50_0616_01502
Produit	Produit
Pléiades 0.5-m	Pléiades 0.5-m
Résolution	Résolution
0.5m	0.5m
Satellite	Satellite
PHR1A	PHR1A
Station d'archivage	Station d'archivage
FR1	FR1

Computation of the geometric configuration of the stereo-pair acqusition

$$\begin{cases} \boldsymbol{X} = \dfrac{\boldsymbol{sin}(\boldsymbol{i_{ACT}})}{\boldsymbol{cos}(\boldsymbol{i_{ACT}})} \\ \boldsymbol{Z} = \dfrac{\boldsymbol{cos}(\boldsymbol{i_{ACT}})}{\boldsymbol{cos}(\boldsymbol{i_{ACT}})} = \mathbf{1} \end{cases}$$

$$\begin{cases} \boldsymbol{Y} = \dfrac{\boldsymbol{sin}(\boldsymbol{i_{ALT}})}{\boldsymbol{cos}(\boldsymbol{i_{ALT}})} \\ \boldsymbol{Z} = \dfrac{\boldsymbol{cos}(\boldsymbol{i_{ALT}})}{\boldsymbol{cos}(\boldsymbol{i_{ALT}})} = \mathbf{1} \end{cases}$$

$$\begin{cases} \boldsymbol{X'} = \dfrac{\boldsymbol{X}}{\sqrt{\boldsymbol{X}^2 + \boldsymbol{Y}^2 + \boldsymbol{Z}^2}} \\ \boldsymbol{Y'} = \dfrac{\boldsymbol{Y}}{\sqrt{\boldsymbol{X}^2 + \boldsymbol{Y}^2 + \boldsymbol{Z}^2}} \\ \boldsymbol{Z'} = \dfrac{\boldsymbol{Z}}{\sqrt{\boldsymbol{X}^2 + \boldsymbol{Y}^2 + \boldsymbol{Z}^2}} \end{cases}$$

	Image 1	Image 2
X' (~vers l'Est)	0.298701905	0.23262011
Y' (~vers le Nord)	0.183824225	-0.1194815
Z' (verticale)	0.936475214	0.96520052
Angle de phase		17.93°

Position of the satellite on a sky-plot (orthogonal projection of the sensor position vector at the target point)

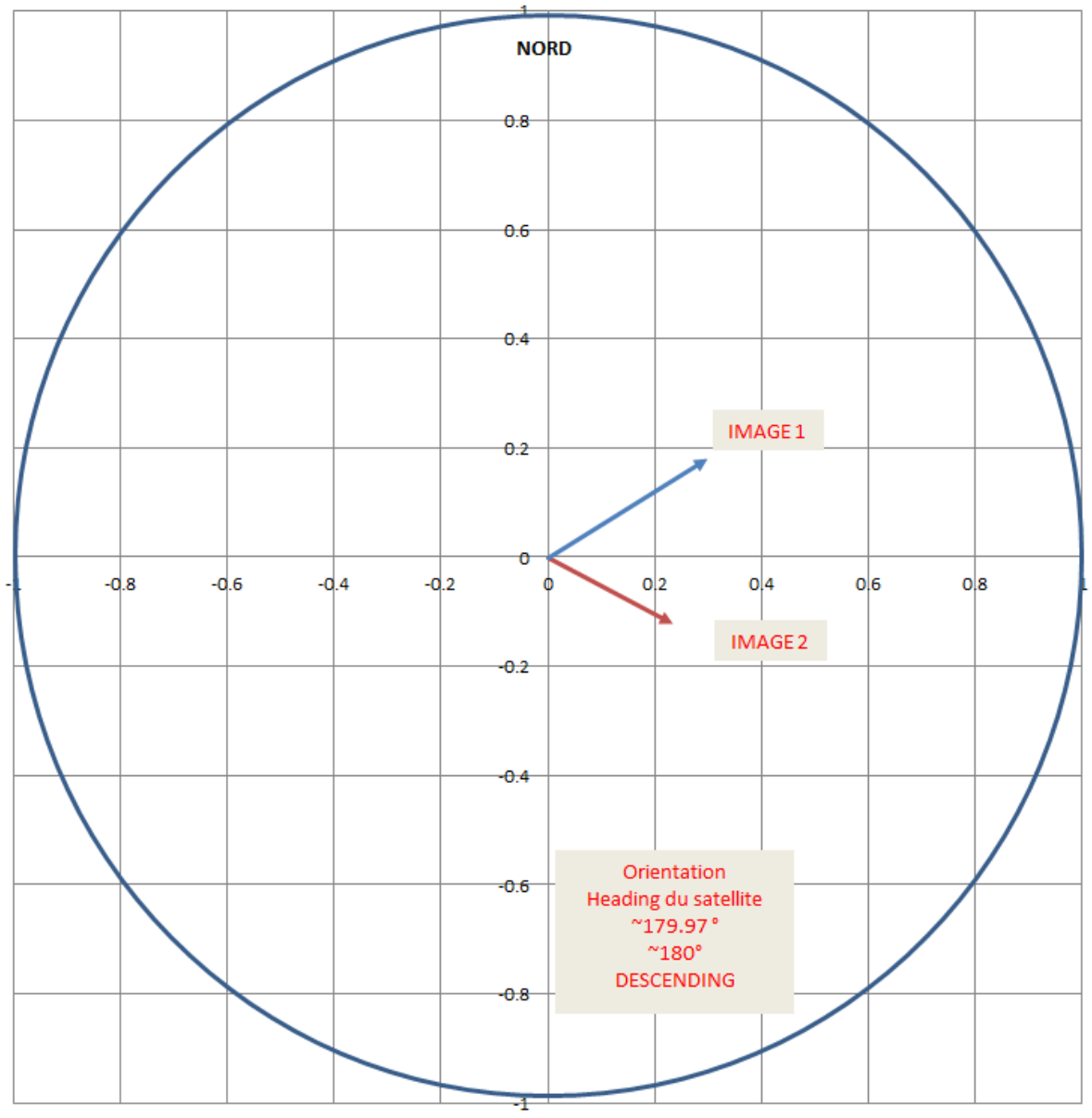

Base to height ratio estimation for a nominal Pleiades height of 694 km

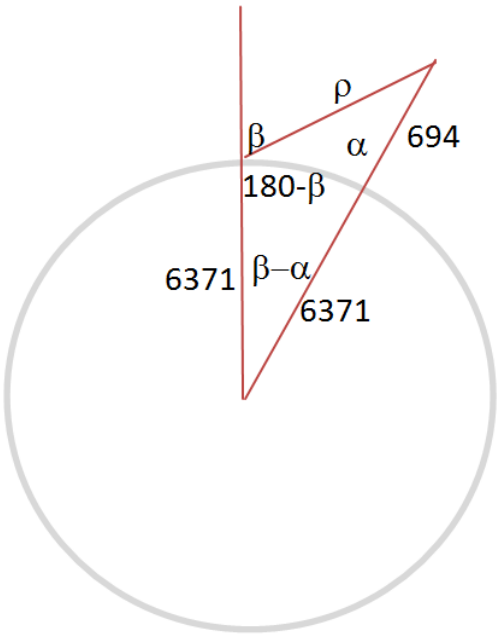

β = incidence angle (see p. 88 of Astrium (2012))

α = viewing angle (see p. 88 of Astrium (2012))

$\rho = \beta - \alpha$

Using the sinus law:

$$\frac{sin(\beta - \alpha)}{\rho} = \frac{sin(180 - \beta)}{(6371 + 694)} = \frac{sin(\alpha)}{6371}$$

$$\frac{sin(\beta - \alpha)}{\rho} = \frac{sin(\beta)}{(6371 + 694)} = \frac{sin(\alpha)}{6371}$$

$$\rho = \frac{(6371 + 694) * sin(\beta - \alpha)}{sin(\beta)} = \frac{6371 * sin(\beta - \alpha)}{sin(\alpha)}$$

ρ_{image1} = 714.02348 km (1st equation) and 711.88254 km (2nd equation - control)

ρ_{image2} = 762.67067 km (1st equation) and 768.14929 km (2nd equation - control)

Phase angle:

$$\phi = arcos(X'_1 X'_2 + Y'_1 Y'_2 + Z'_1 Z'_2)$$

ϕ = 17.93493 °

Computation of the distance (H) and base (B) of stereopair in phase plane.

Note that α et β reported in the next explications don't have the same signification than the one reported in p. 88 of Astrium (2012).

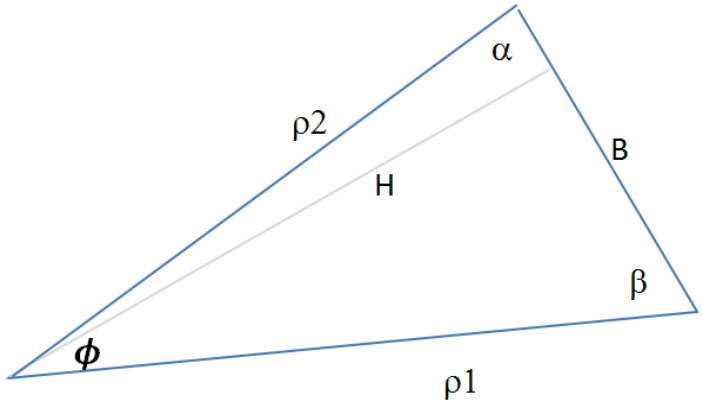

Base (B) :

$$B^2 = \rho_1^2 + \rho_2^2 - 2 * \rho_1\rho_2 cos\phi$$

B = 237.29845 km

Distance (H)

According to trigonometric sinus law:

$$\frac{\rho_2}{sin\beta} = \frac{B}{sin\phi} ; \beta = arcsin(\frac{\rho_2 * sin\phi}{B})$$

$$\frac{\rho_1}{sin\alpha} = \frac{B}{sin\phi} ; \alpha = arcsin(\frac{\rho_1 * sin\phi}{B})$$

β = 85.42208 ° and α = 76.64299 °

$$H = \rho_1 sin\beta$$

H = *709.61143km*

B/H ratio = 237.29845 km / 709.61143km= 0.33441

Time interval between acquisition: ~29 sec

Satellite velocity at 694 km above the Earth surface is $v = \sqrt{\frac{g * R_T^2}{R}}$= 7507.34 m/sec

Distance between two acquisition stations (~B) for 29 sec delay =v*29/1000= 217.71 km

Annex C: Terrain coordinates of 49 surveyed points (GCPs and CPs) and computation table of roundabouts centre

Terrain coordinates of 49 surveyed points (GCPs and CPs):

N°	Point	Est	Nord	Alti	SigmaHZ	SigmaV
1	118	231751.51	148925.8	177.15	0.004	0.008
2	118b	231762.673	148970.788	178.379	0.005	0.01
3	100	224817.801	147874.021	185.663	0.008	0.013
4	111	229855.21	150122.349	186.814	0.007	0.007
5	113	227459.539	148390.315	185.133	0.005	0.008
6	114	226751.345	150127.369	160.783	0.006	0.009
7	115	228696.606	149197.602	189.699	0.006	0.007
8	116	229614.547	149198.029	190.374	0.005	0.01
9	117	230545.261	148976.198	193.623	0.004	0.007
10	124	225456.408	146248.771	189.572	0.006	0.008
11	125	226226.726	146545.375	190.566	0.006	0.008
12	127	228397.756	146380.167	147.239	0.005	0.007
13	128	229547.235	146152.428	83.539	0.005	0.006
14	129	230453.075	146370.816	137.012	0.005	0.007
15	144	226150.248	143672.099	166.476	0.006	0.007
16	145	228523.84	144146.172	65.949	0.006	0.008
17	146	225140.134	142449.364	66.526	0.008	0.01
18	11300	227416.156	148429.103	185.68325	0.007	0.01
19	11600	229631.879	149179.986	190.76125	0.005	0.009
20	12400	225441.204	146267.91	190.8025	0.007	0.009
21	1	234560.559	149225.088	95.848	0.008	0.011
22	119	233058.312	149223.958	146.868	0.01	0.021
23	120	233995.346	149120.345	90.504	0.004	0.009
24	121	234992.99	148834.281	64.198	0.012	0.015
25	122	236221.095	148655.423	63.337	0.009	0.013
26	131	232879.933	146410.834	147.963	0.005	0.007
27	132	233844.457	146072.474	106.228	0.005	0.006
28	134	235926.096	146255.947	67.333	0.005	0.009
29	135	236928.139	145796.773	66.685	0.016	0.026
30	141	231384.195	144028.743	83.803	0.004	0.006
31	142	230381.419	143580.232	119.634	0.007	0.01
32	143	229592.298	143190.314	124.074	0.006	0.009
33	147	225162.339	141812.313	95.086	0.006	0.009
34	150	229225.384	141841.96	197.987	0.013	0.013
35	152	230123.787	141594.23	216.285	0.006	0.008
36	154	232348.874	141220.068	245.433	0.004	0.006

37	155	233556.648	141945.658	242.304	0.009	0.017
38	156	233944.407	141380.599	258.446	0.01	0.021
39	12200	236226.414	148637.16	63.42	0.009	0.01
40	13000	231424.481	145748.365	64.96125	0.01	0.01
41	15600	233923.628	141369.081	259.556	0.003	0.006
42	15700	234934.384	141055.09	239.7735	0.01	0.02
43	0	227035.25	149530.122	170.72825	0.006	0.009
44	108	232965.857	151788.191	172.132	0.009	0.011
45	109	231864.538	150780.778	183.377	0.007	0.009
46	137	235772.208	144101.51	191.506	0.006	0.008
47	138	234639.075	143777.397	197.672	0.004	0.005
48	157	235455.856	141451.625	226.194	0.004	0.008
49	158	236410.122	141481.754	176.856	0.003	0.006

Computation table of roundabouts centre:

The centre points of 9 roundabouts were estimated by least square adjustment from 4 points surveyed around each roundabout. Find below the calculation details:

Circle equation of radius R and centre (x_c,y_c) is written as

$$(x - x_c)^2 + (y - y_c)^2 = R^2.$$

By developing this equation, we get:

$$x^2 + y^2 - 2 * \mathrm{x} * \mathrm{x_c} - 2 * \mathrm{y} * \mathrm{y_c} + x_c^2 \quad + y_c^2 - R^2 = 0.$$

Let us assume that

$$-2 * \mathrm{x_c} = \mathrm{B}; -2 * \mathrm{y_c} = A \text{ and } \mathrm{x_c^2} + \mathrm{y_c^2} - R^2 = -C,$$

we can thus write the corresponding equation as:

$$x^2 + y^2 + \mathrm{B} * \mathrm{x} + \mathrm{A} * \mathrm{y} - \mathrm{C} = 0.$$

This is a multiple linear regression model that can be re-written as:

$$x^2 + y^2 = -\mathrm{B} * \mathrm{x} - \mathrm{A} * \mathrm{y} + \mathrm{C}$$

in which

$x^2 + y^2$ is the dependent variable,

x and y are the independent variables,

-B and -A the regression coefficients of variables x and y respectively and C the intercept.

Using the function "**DROITEREG**" of Excel, the following table was computed. z_c was computed as the average of elevation values of the surveyed 4 points. Error_XY was calculated as an error in estimated radius value of every surveyed point of each roundabout:

$$(\text{Error}_{\text{XY}} = \sqrt{(x - x_c)^2 + \left(y - y_c\right)^2}) - \text{R}\,.$$

RMSE is the root mean square error obtained from of the four Error_XY values.

ID_ter	Z	ID_fin	ZC	X²+Y²	X	Y	A	B	C	Xc	Yc	R	Error_XY	RMSE_XY
11301	185.49	11300	185.683	-73753157450	227427.676	148424.424	-296858.2	-454832.3	73749306415	227416.156	148429.1	12.4449741	-0.01134058	0.0137878
11302	185.7			-73754386521	227419.489	148441.108							0.014509364	
11303	185.8			-73746151622	227405.286	148435.129							-0.01602475	
11304	185.74			-73743023714	227408.996	148418.908							0.012825387	
11601	190.9	11600	190.761	-74983009934	229625.912	149180.932	-298360	-459263.8	74985468172	229631.879	149179.99	6.04514558	-0.0033999	0.0030556
11602	190.88			-74983175210	229630.746	149174.045							0.00304755	
11603	190.6			-74987871410	229637.822	149178.893							-0.00269188	
11604	190.67			-74987144506	229631.604	149186.028							0.003041908	
12401	190.15	12400	190.803	-72218756706	225448.253	146259.502	-292535.8	-450882.4	72218037807	225441.204	146267.91	10.9860092	-0.01383835	0.015342
12402	190.62			-72223547597	225447.638	146276.827							0.009824267	
12403	191.6			-72213778616	225430.427	146269.96							-0.01598126	
12404	190.85			-72212418020	225434.301	146259.338							0.01995218	
12201	63.359	12200	63.42	-77896524810	236223.108	148644.435	-297274.3	-472452.8	77895923918	236226.414	148637.16	8.00196933	-0.01118447	0.0121905
12202	63.415			-77891531767	236220.559	148631.69							0.010634728	
12203	63.445			-77896493444	236231.497	148630.997							-0.0130869	
12204	63.461			-77900398136	236233.16	148641.489							0.013600597	
13001	65.011	13000	64.9613	-74795829217	231414.238	145750.745	-291496.7	-462849	74799876417	231424.481	145748.37	10.5174207	-0.00148204	0.0014117
13002	64.644			-74795348925	231420.936	145738.462							0.001466823	
13003	64.925			-74803600337	231434.513	145745.211							-0.00133662	
13004	65.265			-74804024532	231427.013	145758.575							0.00135519	
15701	239.8	15700	239.774	-75090470337	234937.618	141048.878	-282110.2	-469868.8	75090703139	234934.384	141055.09	6.98407678	0.019120747	0.0172995
15702	239.78			-75094318698	234941.193	141056.565							-0.01719249	
15703	239.76			-75090750908	234930.856	141061.135							0.015331865	
15704	239.76			-75086904174	234928.083	141052.118							-0.01734462	
1	170.82	0	170.728	-73903969095	227040.532	149521.122	-299060.2	-454070.5	73904261975	227035.25	149530.12	10.444566	-0.00855662	0.0085457
2	171.01			-73909816882	227045	149533.892							0.00910999	
3	170.65			-73905322405	227031.239	149539.757							-0.00852361	
4	170.43			-73898719812	227025.465	149526.446							0.00795341	

Annex D: Command lines for DSM and orthoimages production from Vexcel images

step 1: *********tie point computation**********

mm3d Tapioca MulScale .*tif 1000 5000

mm3d SEL ./ 1_10A_16278.tif 1_10A_16279.tif KH=NB SzW=[500,500] R=1

step 2: *********relative orientation **********

N.B:ignore calibration by ommitting distortion coefficiens in relevant file because distortions were less than 2 microns)

Hint: create a folder named " Ori-vexcel" that will contain relative orientation information(means file " AutoCal_Foc-100500_Cam-UltraCamFalcon.xml")

mm3d Tapas Figee .*tif InCal=Ori-Vexcel/

mm3d AperiCloud .*tif Ori-Figee/

CloudCompare AperiCloud_Figee.ply

step 3: *******measuring image coordinates of GCPs and CPs*********

Hint: measure at least 3 points in atleast 2 images and do "GCPBascule" , then do "SaisieAppuisPredic" with estimated orientation from "GCPBascule"

3.A. taking measurements:

mm3d SaisieAppuisInit .*tif Ori-Figee/ gcp-S3D.xml gcp-2D.xml

3.B. GCPBascule to estimate exterior orientation parameters

mm3d GCPBascule .*tif Ori-Figee/ Bascule gcp-S3D.xml gcp-2D-S2D.xml

3.C. SaisieAppuisPredic to measure remaining GCPsand CPs******

mm3d SaisieAppuisPredic .*tif Ori-Bascule/ gcp-S3D.xml gcp-2D.xml

Step 4: ***Computing complete exterior orientation parameters with GCPBascule on a set of measured GCPs****

mm3d GCPBascule .*tif Ori-Figee/ Bascule_final gcp-S3D.xml gcp-2D-S2D.xml

4.A. evaluate geoereferenciation precision of absolute orientation using only CPs

Hint: during measurements GCPs and CPs were stored in same file called "gcp-2D-S2D.xml" so here in order to use only CPs, they have to be separated from GCPs, so, another file called "cp-2D-S2D.xml" was created and used. Note that even if file "gcp-S3D.xml" contains also GCPs and CPs , it

doesn't cause a problem as only points whose image measurements are in "cp-2D-S2D.xml"will be taken into computations.

mm3d GCPCtrl .*tif Ori-Bascule_final/ gcp-S3D.xml cp-2D-S2D.xml

4.B. evaluate if any systematic error remains in exterior orientation results

mm3d MMTestOrient 1_10A_16278.tif 1_10A_16279.tif Ori-Bascule_final

mm3d StatIm ./GeoI-Px/Px2_Num16_DeZoom2_Geom-Im.tif [0,0] Sz=[8650,5580]

Statistics output:

ZMoy=0.00243401 ; Sigma=0.16376

ZMinMax=[-2.20082 , 2.67632]

Step 5: ***use Campari to eliminate any non-linear errors in absolute orientation results (weight of tie point as well as of GCPs was reduced by a factor of 10 because tiepoints were computed at a half resolution of images and GCPs were precise at cm level) *******

mm3d Campari .*tif Ori-Bascule_final/ Campari GCP=[gcp-S3D.xml,10,gcp-2D-S2D.xml,10]

outputs:

Residual = 0.659481 ;; Evol, Moy=3.72328e-09 ,Max=8.09848e-08

| | Worst, Res 0.728661 for 1_12A_46196.tif, Perc 98.5636 for 1_12A_46196.tif

| | Cond , Aver 8.12407 Max 13.5608 Prop>100 0

--- End Iter 5 STEP 0

N.B: to testify the choice of 13GCPS and assess the benefit of more GCPs, all points (GCPs and CPs) were converted into GCPs and by recalculating Camapari we found residuals of 0.66pixels which was equal to 0.659 pixels obtained by only 13 GCPs.so, the later were optimally chosen.

5.A. Assessment of values of transverse parallax using Campari results

mm3d MMTestOrient 1_10A_16278.tif 1_10A_16279.tif Ori-Campari

mm3d StatIm ./GeoI-Px/Px2_Num16_DeZoom2_Geom-Im.tif [0,0] Sz=[8650,5580]

Statistics outputs.

ZMoy=-0.00113295 ; Sigma=0.16264

ZMinMax=[-2.47791 , 2.70144]

Note: mean and sigma was reduced, thus, we kept Campari results for further computations.

Step 6: ******export of cameras centres and omega,phi ,kappa angles********

mm3d OriExport Ori-Campari/Orientation-.*xml PK_cameras_centres.txt

Step 7: *********DSM calculations at 50cm*********

mm3d Malt UrbanMNE .*tif Ori-Campari/ EZA=1 DoOrtho=1 ResolTerrain=0.5 BoxTerrain=[224123,139218.5,236716,151264] NbVI=2

Step 8: ********orthomosaic*********

mm3d Tawny Ortho-MEC-Malt/

Step 9: *********DSM calculations at 25cm*********

mm3d Malt UrbanMNE .*tif Ori-Campari/ EZA=1 DoOrtho=1 NbVI=2

Step 10: ********orthomosaic*********

mm3d Tawny Ortho-MEC-Malt/

Annex E: Commands lines for DSM and orthoimages production from Pleiades stereopair

N.B: except step 3 which was executed in another file, others were executed in working folder containing original images, projection system transformation file "WGS84toL72.xml",xml file terrain coordinates of GCPs and CPs

step 1: ********RPC conversions into Lambert72*****

mm3d Convert2GenBundle "IMG_(.*).tif" "IMG_\$1.xml" RPC-LB72-d0 Degre=0 ChSys=WGS84toL72.xml

step 2: ****tie points computation*****

mm3d Tapioca All .*tif -1

step 3: *****conversion from 16bits to 8bits for GCPs and CPs' image measurement***µ

mm3d to8Bits IMG_001.tif Dyn=0.1

mm3d to8Bits IMG_002.tif Dyn=0.1

step 4: *******use of converted 8bits images whose contrast was improved to measure image coordinates of GCPs and CPs (copy 8bit images and change their names assame as original images, copy results of step1 and xml file containing 3D coordinates of GCPs into another folder in which these measurements will be made : here we used "test for 8 bits"). N****

mm3d SaisieAppuisPredic .*tif Ori-RPC-LB72-d0/ gcp-S3D.xml gcp-2D.xml SzW=[500,500]

step 5: ********Campari:tie points + GCPs by reducing GCPs' weight by a factor of 10**********

Hint: copy in working folder the xml file containing image measurements taken (i.e file " gcp-2D-S2D.xml")

mm3d Campari .*tif Ori-RPC-LB72-d0/ campari_gcp-LB72 GCP=[gcp-S3D.xml,10,gcp-2D-S2D.xml,1]

Results of Campari:

========== ERRROR MAX PTS FL ==========

|| Value=1.27761 for Cam=IMG_002.tif and Pt=12200 ; MoyErr=0.503422

==========

RES:[IMG_001.tif][g] ER2 0.293632 Nn 99.8112 Of 51905 Mul 0 Mul-NN 0 Time 5.40377

RES:[IMG_002.tif][g] ER2 0.293803 Nn 99.8034 Of 55965 Mul 0 Mul-NN 0 Time 5.78747

| | Residual = 0.293717 ;; Evol, Moy=1.08163e-08 ,Max=1.09656e-08

| | Worst, Res 0.293803 for IMG_002.tif, Perc 99.8034 for IMG_002.tif

| | Cond , Aver 6.79361 Max 5000.85 Prop>100 2.32126e-05

--- End Iter 5 STEP 0

step 6: ******** evaluation of bundle adjustment quality******

mm3d MMTestOrient IMG_001.tif IMG_002.tif Ori-campari_gcp-LB72/ ZMoy=200 ZInc=400 GB=1

mm3d StatIm ./GeoI-Px/Px2_Num16_DeZoom2_Geom-Im.tif [30,40] Sz=[11500,11500]

Statistics output:

ZMoy=0.136884 ; Sigma=0.122605

ZMinMax=[-1.67729 , 2.1992]

step 7: *******DSM generation *********

mm3d Malt UrbanMNE "IMG_00[0-2]{1}.tif" Ori-campari_gcp-LB72/ DoOrtho=1 EZA=1

7.A. OUTPUTS:

========== PARAMS ==========

- SzWindow 1 (i.e. : 3x3)
- Regul 0.02

- Final Zoom 1
- Initial Zoom 32
- Use TA as Mask No
- Z Step : 0.4
- Nb Min Visible Images : 2

==========

7.B. Visualisation of DSM

mm3d Vino ./MEC-Malt/Z_Num8_DeZoom1_STD-MALT.tif Dyn=[60,280]

Hint: we put in Dyn the range of altitude values of studied area.

step 8:***** orthomosaic *****

mm3d Tawny Orth-MEC-Malt/

Annex F: Exterior orientation results per image (angles are in degrees and X,Y,Z in meters)

Image_Name	Omega(W)	Phi(P)	Kappa(K)	X_camera	Y_Camera	Z_Camera
1_10A_16278.tif	0.435493	-0.244146	-90.469793	237140.2218	149962.9892	4103.203458
1_10A_16279.tif	0.035201	-0.255919	-90.106846	236079.0219	149957.8599	4105.971592
1_10A_16280.tif	-0.484418	-0.355022	-90.140932	235026.5025	149950.305	4105.075703
1_10A_16281.tif	-0.744879	-0.348351	-90.443123	233973.4401	149947.377	4105.311666
1_10A_16282.tif	-0.782533	-0.408894	-90.952003	232918.038	149952.4013	4107.443505
1_10A_16283.tif	-0.242362	-0.572196	-91.184275	231866.7673	149964.6875	4106.38584
1_10A_16284.tif	0.887022	-0.530482	-90.649	230815.9637	149974.6811	4105.588126
1_10A_16285.tif	0.108555	-0.440897	-90.102226	229762.2043	149971.4937	4103.422862
1_10A_16286.tif	-0.305329	-0.446947	-89.966424	228706.641	149962.7443	4104.241678
1_10A_16287.tif	-0.538151	-0.432929	-90.15349	227650.0765	149955.2773	4103.341517
1_10A_16288.tif	-0.441233	-0.29323	-90.42751	226597.3722	149952.8268	4101.740522
1_10A_16289.tif	-0.333069	-0.287665	-90.761161	225544.6172	149954.2327	4102.245811
1_11A_46330.tif	-0.078269	-0.274796	89.203831	225430.6643	147377.8745	4076.061428
1_11A_46331.tif	-0.090653	-0.267079	89.279773	226483.3164	147374.0865	4078.078413
1_11A_46332.tif	-0.114826	-0.266009	89.05787	227538.5951	147369.6524	4079.272859
1_11A_46333.tif	-0.107096	-0.261877	89.105426	228592.529	147364.6675	4077.818279
1_11A_46334.tif	-0.104562	-0.276113	89.204838	229646.7104	147359.1627	4076.886957
1_11A_46335.tif	-0.114756	-0.261849	89.109526	230699.9341	147353.7081	4076.948681
1_11A_46336.tif	-0.087689	-0.258993	89.359138	231754.0189	147350.4095	4078.13229
1_11A_46337.tif	-0.091614	-0.243185	89.49154	232808.8279	147352.0014	4079.738034
1_11A_46338.tif	-0.085275	-0.238371	89.65946	233874.9936	147356.7589	4079.783364
1_11A_46339.tif	-0.104358	-0.231108	89.816228	234943.3388	147363.6732	4077.743144
1_11A_46340.tif	-0.095768	-0.232113	89.845673	236013.2069	147371.8306	4075.612299
1_11A_46341.tif	-0.118063	-0.220183	89.997138	237081.9535	147380.1979	4073.316764
1_12A_46196.tif	0.09086	0.290454	-89.917703	236798.0618	144907.6226	4077.62627
1_12A_46197.tif	0.10477	0.271209	-89.756353	235753.5181	144893.9691	4075.422125
1_12A_46198.tif	0.101235	0.278634	-89.864022	234714.3241	144880.2003	4073.906829
1_12A_46199.tif	0.119078	0.258697	-90.115864	233675.1045	144866.9551	4075.198382
1_12A_46200.tif	0.106377	0.255484	-90.795768	232629.6387	144863.0799	4077.724035
1_12A_46201.tif	0.112985	0.242921	-90.929755	231579.6744	144864.524	4079.823678
1_12A_46202.tif	0.119324	0.236121	-90.860246	230531.3954	144867.6763	4080.180871
1_12A_46203.tif	0.101868	0.236345	-91.038808	229474.7756	144872.437	4078.97482
1_12A_46204.tif	0.094892	0.234029	-90.954382	228410.6301	144877.9553	4077.858458
1_12A_46205.tif	0.086761	0.23745	-91.188721	227348.6792	144885.2288	4077.44351
1_12A_46206.tif	0.111803	0.232015	-91.129853	226289.4839	144894.3781	4075.526266
1_12A_46207.tif	0.117339	0.225479	-90.973462	225238.5751	144902.8113	4074.760701
1_13A_46086.tif	-0.078061	-0.284298	89.254928	225150.506	142489.2613	4072.714377

1_13A_46087.tif	-0.083879	-0.271098	89.342022	226192.2678	142486.6217	4074.864953
1_13A_46088.tif	-0.075406	-0.242123	89.533576	227235.0563	142484.6979	4077.016787
1_13A_46089.tif	-0.090568	-0.260816	89.124467	228280.0487	142482.2906	4079.664944
1_13A_46090.tif	-0.073437	-0.258311	89.175596	229331.8161	142477.919	4081.456973
1_13A_46091.tif	-0.098843	-0.251709	89.14943	230364.7743	142473.3253	4079.494399
1_13A_46092.tif	-0.082285	-0.254094	89.046213	231398.6885	142468.3485	4076.594796
1_13A_46093.tif	-0.094318	-0.2527	89.172318	232431.1261	142464.1783	4074.803901
1_13A_46094.tif	-0.077509	-0.247652	89.148984	233462.6223	142460.1354	4075.476239
1_13A_46095.tif	-0.089035	-0.2359	89.259679	234496.7502	142457.0941	4077.373082
1_13A_46096.tif	-0.088052	-0.234553	89.278036	235533.3626	142454.821	4078.213417
1_13A_46097.tif	-0.084511	-0.216947	89.758272	236575.6597	142455.2747	4080.222951

Annex G: Visual identity of GCPs and CPs used in processing Vexcel and Pleiades images

(GCPs are ground control points used in adjustment and CPs are points used in quality assessment of created 3D models)

Graphical position	characteristics
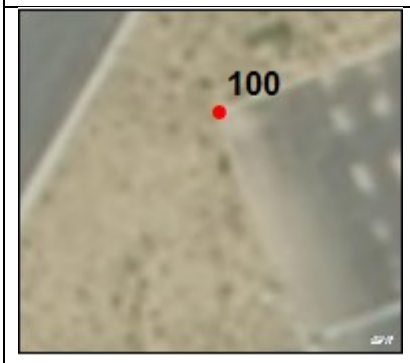	Terrain Coordinates : X : 224817.801 m Y : 147874.021 m Z : 185.663 m Nature: Parking Surveyed point: wedge point joining parking to lawn Use : GCPs on Vexcel
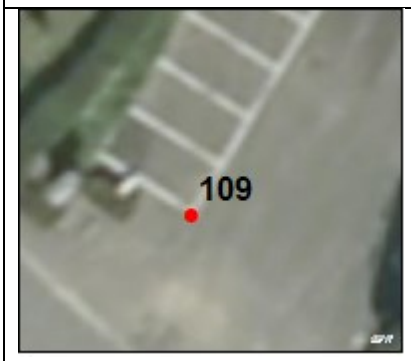	Terrain Coordinates: X :231864.538 m Y : 150780.778 m Z : 183.377 m Nature: Parking Surveyed point: exterior wedge point Use : GCPs on Vexcel and Pleiades
	Terrain Coordinates: X : 226751.345 m Y : 150127.369 m Z : 160.783 m Nature: Parking Surveyed point: inner wedge point Use : GCPs on Vexcel and Pleiades
	Terrain Coordinates: X : 236221.095 m Y : 148655.423 m Z : 63.337 m Nature: Surveyed point: inner wedge point Use : GCPs on Vexcel

	Terrain Coordinates: X : 226226.726 m Y : 146545.375 m Z : 190.566 m Nature: parking Surveyed point: exterior wedge point Use : GCPs on Vexcel
	Terrain Coordinates: X : 229547.235 m Y : 146152.428 m Z : 83.539 m Nature: Crosswalk Surveyed point: exterior wedge point Use : GCPs on Vexcel and Pleiades
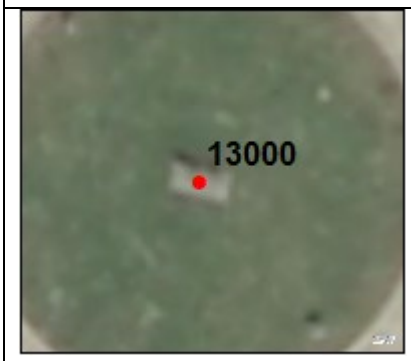	Terrain Coordinates: X : 231424.481 m Y : 145748.365 m Z : 64.96125 m Nature: Roundabout Surveyed point: estimated centre point Use: GCPs on Vexcel and Pleiades
	Terrain Coordinates: X : 231424.481 m Y : 145748.365 m Z : 64.96125 m Nature: Crosswalk Surveyed point: exterior wedge point Use: GCPs on Vexcel

	Terrain Coordinates: X : 235772.208 m Y : 144101.51 m Z : 191.506 m Nature: Crosswalk Surveyed point: exterior wedge point Use: GCPs on Vexcel and Pleaides
	Terrain Coordinates: X : 226150.248 m Y : 143672.099 m Z : 166.476 m Nature: Crosswalk Surveyed point: exterior wedge point Use: GCPs on Vexcel and Pleiades
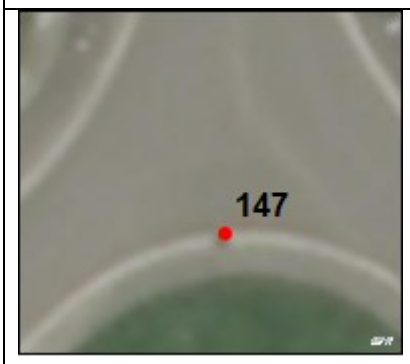	Terrain Coordinates: X : 225162.339 m Y : 141812.313 m Z : 95.086 m Nature: drain (avaloir in French) Surveyed point: exterior wedge point Use: GCPs on Vexcel
	Terrain Coordinates: X : 232348.874 m Y : 141220.068 m Z : 245.433 m Nature: speed bump Surveyed point: inner wedge point Use: GCPs on Vexcel

	Terrain Coordinates: X : 236410.122 m Y : 141481.754 m Z : 176.856 m Nature: joins of two streets Surveyed point: intersection point Use: GCPs on Vexcel
	Terrain Coordinates: X : 236226.414 m Y : 148637.16 m Z : 63.42 m Nature: roundabouts Surveyed point: estimated central point Use: GCPs on Pleiades
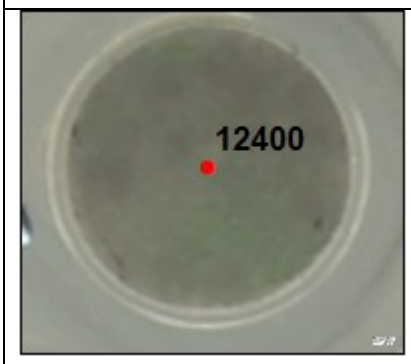	Terrain Coordinates: X : 225441.204 m Y : 146267.91 m Z : 190.8025 m Nature: roundabouts Surveyed point: estimated central point Use: GCPs on Pleiades
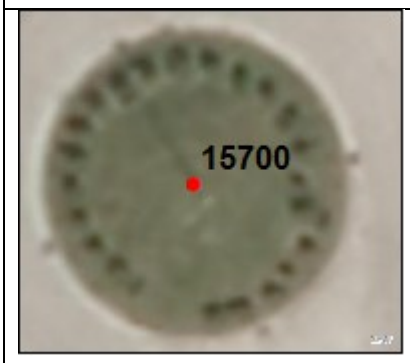	Terrain Coordinates: X : 234934.384 m Y : 141055.09 m Z : 239.7735 m Nature: roundabouts Surveyed point: estimated central point Use: GCPs on Pleiades

	Terrain Coordinates: X : 232879.933 m Y : 146410.834 m Z : 147.963 m Nature: Crosswalk Surveyed point: exterior wedge point Use: GCPs on Pleiades
	Terrain Coordinates: X : 225140.134 m Y : 142449.364 m Z : 66.526 m Nature: Crosswalk Surveyed point: exterior wedge point Use: GCPs on Pleiades
	Terrain Coordinates: X : 230123.787 m Y : 141594.23 m Z : 216.285 m Nature: Crosswalk Surveyed point: exterior wedge point Use: GCPs on Pleiades
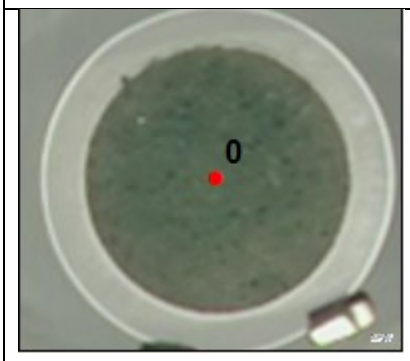	Terrain Coordinates: X : 227035.25 m Y : 149530.122 m Z : 170.72825 m Nature: roundabouts Surveyed point: estimated central point Use: CPs

	Terrain Coordinates: X : 234560.559 m Y : 149225.088 m Z : 95.848 m Nature: Crosswalk Surveyed point: exterior wedge point Use: CPs
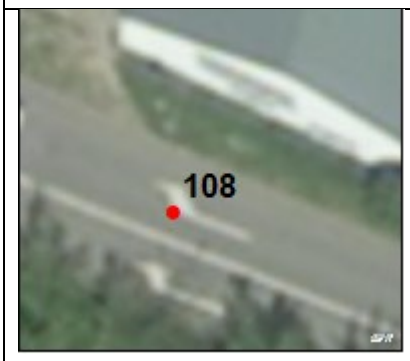	Terrain Coordinates: X : 232965.857 m Y : 151788.191 m Z : 172.132 m Nature: direction marks in the roads Surveyed point: exterior wedge point Use: CPs
	Terrain Coordinates: X : 229855.21 m Y : 150122.349 m Z : 186.814 m Nature: paved surface Surveyed point: exterior wedge point Use: CPs
	Terrain Coordinates: X : 227459.539 m Y : 148390.315 m Z : 185.133 m Nature: parking Surveyed point: wedge point joining parking to lawn Use: CPs

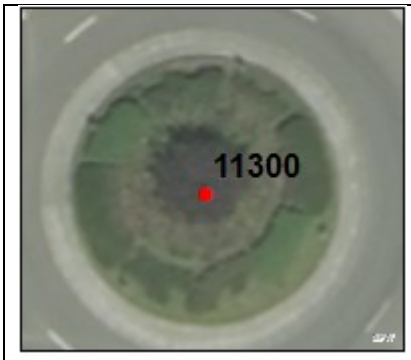	Terrain Coordinates: X : 227416.156 m Y : 148429.103 m Z : 185.68325 m Nature: roundabouts Surveyed point: estimated central point Use: CPs
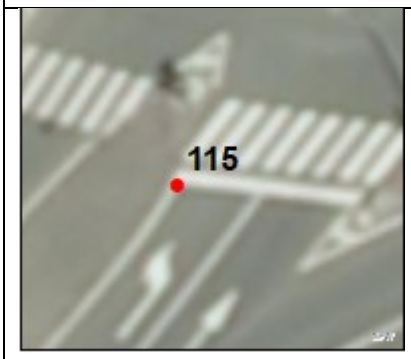	Terrain Coordinates: X : 228696.606 m Y : 149197.602 m Z : 189.699 m Nature: Roads' marks Surveyed point: inner wedge point Use: CPs
	Terrain Coordinates: X : 229614.547 m Y : 149198.029 m Z : 190.374 m Nature: Crosswalk Surveyed point: exterior wedge point Use: CPs
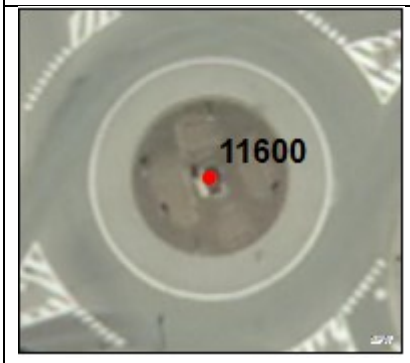	Terrain Coordinates: X : 229631.879 m Y : 149179.986 m Z : 190.76125 m Nature: roundabouts Surveyed point: estimated central point Use: CPs

	Terrain Coordinates: X : 230545.261 m Y : 148976.198 m Z : 193.623 m Nature: Crosswalk Surveyed point: exterior wedge point Use: CPs
	Terrain Coordinates: X : 231751.51 m Y : 148925.8 m Z : 177.15 m Nature: Crosswalk Surveyed point: exterior joining point of crosswalk and edge of the road Use: CPs
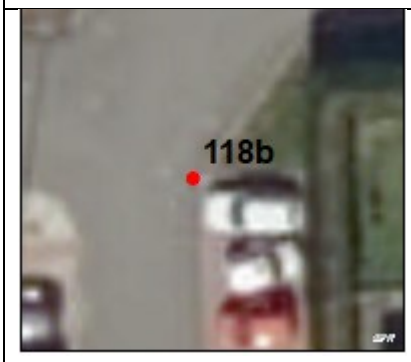	Terrain Coordinates: X : 231762.673 m Y : 148970.788 m Z : 178.379 m Nature: Parking Surveyed point: exterior wedge point Use: CPs
	Terrain Coordinates: X : 233058.312 m Y : 149223.958 m Z : 146.868 m Nature: Crosswalk Surveyed point: exterior wedge point Use: CPs

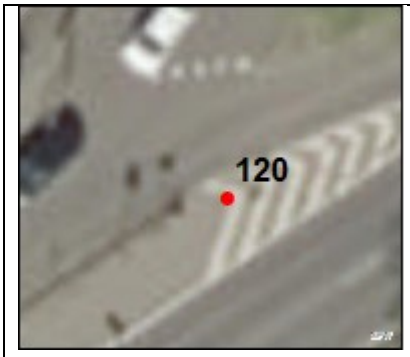	Terrain Coordinates: X : 233995.346 m Y : 149120.345 m Z : 90.504 m Nature: Roads' marks Surveyed point: inner wedge point Use: CPs
	Terrain Coordinates: X : 234992.99 m Y : 148834.281 m Z : 64.198 m Nature: paved edge of lawn Surveyed point: inner wedge point Use: CPs
	Terrain Coordinates: X : 225456.408 m Y : 146248.771 m Z : 189.572 m Nature: Crosswalk Surveyed point: exterior wedge point Use: CPs
	Terrain Coordinates: X : 228397.756 m Y : 146380.167 m Z : 147.239 m Nature: speed bump Surveyed point: joining wedge inner point Use: CPs

	Terrain Coordinates: X : 230453.075 m Y : 146370.816 m Z : 137.012 m Nature: joins of roads Surveyed point: joining wedge inner point Use: CPs
	Terrain Coordinates: X : 235926.096 m Y : 146255.947 m Z : 67.333 m Nature: Crosswalk Surveyed point: exterior wedge point Use: CPs
	Terrain Coordinates: X : 236928.139 m Y : 145796.773 m Z : 66.685 m Nature: Crosswalk Surveyed point: exterior wedge point Use: CPs
	Terrain Coordinates: X : 234639.075 m Y : 143777.397 m Z : 197.672 m Nature: Parking with T marks Surveyed point: middle T point Use: CPs

	Terrain Coordinates: X : 231384.195 m Y : 144028.743 m Z : 83.803 m Nature: Crosswalk Surveyed point: exterior wedge point Use: CPs
	Terrain Coordinates: X : 230381.419 m Y : 143580.232 m Z : 119.634 m Nature: Crosswalk Surveyed point: exterior wedge point Use: CPs
	Terrain Coordinates: X : 229592.298 m Y : 143190.314 m Z : 124.074 m Nature: Crosswalk Surveyed point: exterior wedge point Use: CPs
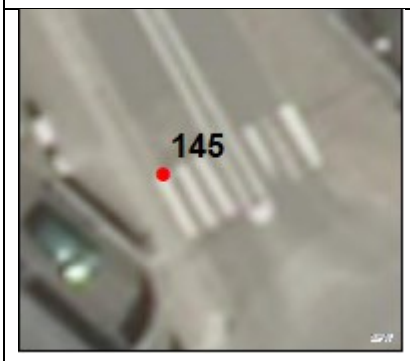	Terrain Coordinates: X : 228523.84 m Y : 144146.172 m Z : 65.949 m Nature: Crosswalk Surveyed point: exterior wedge point Use: CPs

	Terrain Coordinates: X : 229225.384 m Y : 141841.96 m Z : 197.987 m Nature: Crosswalk Surveyed point: exterior wedge point Use: CPs
	Terrain Coordinates: X : 233556.648 m Y : 141945.658 m Z : 242.304 m Nature: speed bump Surveyed point: exterior wedge point Use: CPs
	Terrain Coordinates: X : 233944.407 m Y : 141380.599 m Z : 258.446 m Nature: Crosswalk Surveyed point: exterior wedge point Use: CPs
	Terrain Coordinates: X : 233923.628 m Y : 141369.081 m Z : 259.556 m Nature: Roads' marks Surveyed point: inner wedge point Use: CPs

	Terrain Coordinates: X : 235455.856 m Y : 141451.625 m Z : 226.194 m Nature: Crosswalk Surveyed point: exterior wedge point Use: CPs

Annex H: Reprojection, planimetric and altimetric errors of CPs on Vexcel and Pleiades

Pleiades					
CPs	DX [m]	DY [m]	DZ [m]	ERR_X_Y[m]	Err_reproj [pixel]
0	-0.17275039	0.440099516	-0.145410223	0.472789891	0.11261026
1	0.773791113	1.032031931	-0.418405701	1.289900226	0.17748143
111	0.203716877	0.389009699	-0.919986527	0.439123117	0.132154248
113	-0.582417505	0.516247869	-1.864638744	0.778281448	0.375886962
11300	0.196633284	-0.480873897	5.139171315	0.519523198	0.709124008
115	-0.364167297	0.158078065	-0.605040878	0.396996845	0.141131993
116	0.165768482	0.99371963	-1.351616753	1.007451187	0.141131993
11600	0.209000583	0.368152343	0.773838255	0.423340751	0.079247184
117	-0.033937415	0.605950412	-0.802027982	0.606900033	0.072494188
118b	0.126340824	0.976325801	-0.752425985	0.98446639	0.239944481
119	0.163884294	0.29064747	-0.559540895	0.333667519	0.136327339
121	0.08479611	-0.117012314	0.501624711	0.144506961	0.684111957
124	-0.834857769	0.108769607	0.241201546	0.841913489	0.272099242
125	-0.657410108	-0.050304256	0.256538411	0.659331911	0.348401837
129	-0.293851615	0.147756795	0.255170914	0.328908562	0.010589463
141	-0.120840522	-0.051662116	0.177440495	0.131420721	0.101497014
142	-0.007341944	1.164391689	-0.441950621	1.164414836	0.281362114
143	0.444181364	-0.325723374	-0.51137441	0.550811039	0.184395002
145	-0.266952563	-0.299420598	-1.510310095	0.401143822	0.420620115
147	0.563816523	-0.155461072	1.691204268	0.584856577	1.072457082
15600	0.525987805	-0.193315669	-1.622340435	0.560387472	0.798060507
Vexcel					
1	-0.104169276	0.207166216	0.167171482	0.231881606	0.280464482
100	-0.02	0.015	0.05	0.025	0.512025
108	0.591340396	-0.797151797	0.024571806	0.992539395	0.062033695
109	-0.049253266	-0.026304052	0.230231141	0.05583715	0.318143576
111	0.319919407	-0.14352396	0.27808335	0.35063878	0.363477201
113	0.422518034	-0.041729031	0.279870664	0.42457367	0.610658984
114	-0.007252613	-0.013155403	-0.450239194	0.015022151	0.546657901
115	0.104751564	-0.104319972	0.604385311	0.147836216	0.28941938
117	0.339295765	0.177796931	0.659661539	0.383057913	0.379049117
118	0.087422185	-0.137007082	0.748346538	0.162522549	0.412183709
119	-0.22800597	-0.175994335	0.637612436	0.28802904	0.426225584
120	-0.30861644	-0.173819418	0.460948026	0.354199516	0.386172472
121	-0.116385931	-0.178166587	0.032868636	0.212812165	0.275685606
122	-0.02550909	-0.039323153	-0.070315257	0.046872423	0.410435201
124	0.064736386	-0.308069827	-0.367738219	0.314798059	0.435643233
125	0.007939596	-0.140914717	0.216770445	0.141138211	0.503024268
127	0.062128415	-0.121507054	0.557982723	0.136469426	0.194724286
128	0.059445652	0.05897055	0.187095188	0.083733573	0.497615438
13000	-0.005115623	0.016735954	-0.186734835	0.017500336	0.276336606
132	0.010600598	0.015228572	0.037685775	0.01855484	0.247176345
134	-0.492984181	-0.050547592	0.140762769	0.495568826	0.468670244

135	0.089634992	-0.384711577	-0.367349907	0.395015733	0.421753872
137	0.006378545	-0.004974825	-0.000234123	0.008089173	0.179178743
138	-0.080740815	-0.184928441	0.101386552	0.201786044	0.321306079
141	0.050072739	-0.059421958	0.608663741	0.077706167	0.29496812
142	-0.115851334	-0.023992959	0.401553073	0.118309736	0.312775982
143	0.082149098	-0.014631745	0.337749948	0.08344197	0.340266111
144	-0.038724673	0.040667883	-0.109288742	0.056155828	0.504135968
145	0.251161202	-0.121437858	0.253945602	0.278978678	0.465344665
147	0.005620961	0.06840327	0.239125821	0.068633829	0.274974449
150	-0.222194756	0.404456423	0.554967301	0.461471026	0.311841183
152	0.099102677	-0.109089176	0.097770116	0.147383137	0.212397338
154	0.073512203	0.0762633	0.112248842	0.105925139	0.474092011
155	-0.160359343	-0.267243747	-0.036486973	0.311663824	0.592471913
156	-0.181089599	-0.670728054	-0.593237983	0.694744244	0.170264774
157	0.241704873	-0.334885053	-0.754027543	0.413000296	0.270745004
158	0.005290656	-0.137978401	-0.098764141	0.138079797	0.488926476

Annex I: Characteristics of processed Vexcel aerial images

IMAGE_ NAME	ACQ_ HOURS	ACQ_DATE	SUN_ ELEVAT (°)	AVG_ HEIGHT (m)	AER_ HEIGHT (m)	AER_FLY_X (m)	AER_FLY_Y (m)	AER_ SCALE	FOCAL (mm)	AER_ OVER _LAP	AER_ SIDE_ LAP	PIXEL_X_Y SIZE (m)
1_10A_16278	11:58:24	15-04-15	49.10	4105	200	237138.203	149960.954	39861	100.500	60	30	0.250
1_10A_16279	11:58:33	15-04-15	49.10	4105	200	236077.573	149955.763	39861	100.500	60	30	0.250
1_10A_16280	11:58:42	15-04-15	49.10	4105	200	235025.579	149948.333	39861	100.500	60	30	0.250
1_10A_16281	11:58:52	15-04-15	49.10	4105	200	233973.190	149945.399	39861	100.500	60	30	0.250
1_10A_16282	11:59:01	15-04-15	49.10	4105	200	232918.342	149950.754	39861	100.500	60	30	0.250
1_10A_16283	11:59:10	15-04-15	49.10	4105	200	231867.307	149963.129	39861	100.500	60	30	0.250
1_10A_16284	11:59:19	15-04-15	49.10	4105	200	230816.267	149973.125	39861	100.500	60	30	0.250
1_10A_16285	11:59:28	15-04-15	49.10	4105	200	229762.990	149970.159	39861	100.500	60	30	0.250
1_10A_16286	11:59:38	15-04-15	49.10	4105	200	228707.903	149961.352	39861	100.500	60	30	0.250
1_10A_16287	11:59:47	15-04-15	49.10	4105	200	227651.611	149954.054	39861	100.500	60	30	0.250
1_10A_16288	11:59:56	15-04-15	49.10	4105	200	226599.723	149951.435	39861	100.500	60	30	0.250
1_10A_16289	12:00:05	15-04-15	49.10	4105	200	225547.469	149952.771	39861	100.500	60	30	0.250
1_11A_46330	14:21:44	12-04-15	36.50	4105	200	225433.040	147375.865	39861	100.500	60	30	0.250
1_11A_46331	14:21:51	12-04-15	36.50	4105	200	226485.175	147372.284	39861	100.500	60	30	0.250
1_11A_46332	14:21:59	12-04-15	36.50	4105	200	227540.080	147367.696	39861	100.500	60	30	0.250
1_11A_46333	14:22:06	12-04-15	36.50	4105	200	228593.682	147362.895	39861	100.500	60	30	0.250
1_11A_46334	14:22:13	12-04-15	36.40	4105	200	229647.921	147357.458	39861	100.500	60	30	0.250
1_11A_46335	14:22:21	12-04-15	36.40	4105	200	230700.855	147351.893	39861	100.500	60	30	0.250
1_11A_46336	14:22:28	12-04-15	36.40	4105	200	231754.295	147348.536	39861	100.500	60	30	0.250
1_11A_46337	14:22:35	12-04-15	36.40	4105	200	232808.721	147350.174	39861	100.500	60	30	0.250
1_11A_46338	14:22:43	12-04-15	36.30	4105	200	233874.863	147354.674	39861	100.500	60	30	0.250
1_11A_46339	14:22:50	12-04-15	36.30	4105	200	234942.667	147361.892	39861	100.500	60	30	0.250
1_11A_46340	14:22:58	12-04-15	36.30	4105	200	236011.991	147369.987	39861	100.500	60	30	0.250
1_11A_46341	14:23:05	12-04-15	36.30	4105	200	237080.522	147378.271	39861	100.500	60	30	0.250
1_12A_46196	13:58:10	12-04-15	39.30	4105	200	236796.136	144909.440	39861	100.500	60	30	0.250
1_12A_46197	13:58:20	12-04-15	39.30	4105	200	235752.106	144895.832	39861	100.500	60	30	0.250
1_12A_46198	13:58:29	12-04-15	39.30	4105	200	234713.243	144881.931	39861	100.500	60	30	0.250
1_12A_46199	13:58:39	12-04-15	39.30	4105	200	233674.509	144868.613	39861	100.500	60	30	0.250
1_12A_46200	13:58:48	12-04-15	39.30	4105	200	232629.476	144864.648	39861	100.500	60	30	0.250
1_12A_46201	13:58:58	12-04-15	39.30	4105	200	231580.022	144865.862	39861	100.500	60	30	0.250
1_12A_46202	13:59:07	12-04-15	39.30	4105	200	230532.236	144869.080	39861	100.500	60	30	0.250
1_12A_46203	13:59:17	12-04-15	39.20	4105	200	229475.474	144873.549	39861	100.500	60	30	0.250
1_12A_46204	13:59:27	12-04-15	39.20	4105	200	228411.180	144878.981	39861	100.500	60	30	0.250
1_12A_46205	13:59:36	12-04-15	39.20	4105	200	227349.580	144886.314	39861	100.500	60	30	0.250
1_12A_46206	13:59:46	12-04-15	39.20	4105	200	226290.949	144895.419	39861	100.500	60	30	0.250
1_12A_46207	13:59:55	12-04-15	39.20	4105	200	225240.690	144903.925	39861	100.500	60	30	0.250
1_13A_46086	13:38:43	12-04-15	41.60	4105	200	225152.434	142489.208	39861	100.500	60	30	0.250
1_13A_46087	13:38:50	12-04-15	41.50	4105	200	226193.586	142486.501	39861	100.500	60	30	0.250
1_13A_46088	13:38:58	12-04-15	41.50	4105	200	227236.087	142484.654	39861	100.500	60	30	0.250
1_13A_46089	13:39:05	12-04-15	41.50	4105	200	228281.317	142482.054	39861	100.500	60	30	0.250
1_13A_46090	13:39:13	12-04-15	41.50	4105	200	229333.086	142477.617	39861	100.500	60	30	0.250
1_13A_46091	13:39:20	12-04-15	41.50	4105	200	230365.558	142472.920	39861	100.500	60	30	0.250
1_13A_46092	13:39:27	12-04-15	41.50	4105	200	231399.603	142468.092	39861	100.500	60	30	0.250
1_13A_46093	13:39:35	12-04-15	41.40	4105	200	232431.678	142463.911	39861	100.500	60	30	0.250
1_13A_46094	13:39:42	12-04-15	41.40	4105	200	233462.493	142459.972	39861	100.500	60	30	0.250
1_13A_46095	13:39:50	12-04-15	41.40	4105	200	234496.071	142456.883	39861	100.500	60	30	0.250
1_13A_46096	13:39:57	12-04-15	41.40	4105	200	235531.818	142454.610	39861	100.500	60	30	0.250